

# **Numerical/Optical Simulation of Laser Beam Propagation Through Atmospheric Turbulence**

**Final Technical Report**

**by**

**Sergei S. Chesnokov  
Valerii P. Kandidov  
Victor I. Shmalhausen  
Vladimir V. Shuvalov**

*October 1994 — December 1995*

**United States Army**

**EUROPEAN RESEARCH OFFICE OF THE U.S. ARMY**

**London England**

**CONTRACT NUMBER N68171-94-C-9147**

**INTERNATIONAL LASER CENTER, MOSCOW STATE UNIVERSITY**

**Moscow Russia**

**19960122 018**

**Approved for Public Release; distribution unlimited**

## REPORT DOCUMENTATION PAGE

Form Approved  
OMB No. 0704-0188

Public reporting burden for this collection of information is estimated to average 1 hour per response, including the time for reviewing instructions, searching existing data sources, gathering and maintaining the data needed, and completing and reviewing the collection of information. Send comments regarding this burden estimate or any other aspect of the collection of information, including suggestions for reducing this burden, to Washington Headquarters Services, Directorate for Information Operations and Reports, 1215 Jefferson Davis Highway, Suite 1204, Arlington, VA 22202-4302, and to the Office of Management and Budget, Paperwork Reduction Project (0704-0188), Washington, DC 20503.

1. AGENCY USE ONLY (Leave blank)	2. REPORT DATE	3. REPORT TYPE AND DATES COVERED
	01 DEC 1995	FINAL, 01 OCT 1994 - 01 DEC 1995
4. TITLE AND SUBTITLE		5. FUNDING NUMBERS
Numerical/Optical Simulation of Laser Beam Propagation Through Atmospheric Turbulence		C N68171-94-C-9147 PR WK2Q6C-7472-CH01
6. AUTHOR(S)		7. PERFORMING ORGANIZATION NAME(S) AND ADDRESS(ES)
Sergei S. Chesnokov Valerii P. Kandidov Viktor I. Shmalgauzen Vladimir V. Shuvalov		International Laser Center Moscow State University Vorob'evy Gory 119899, Moscow, Russia
8. PERFORMING ORGANIZATION REPORT NUMBER		9. SPONSORING/MONITORING AGENCY NAME(S) AND ADDRESS(ES)
4-th		Naval Regional Contracting Center Detachment London, Block 2, WING11 DOE COMPLEX, EASTCOTE ROAD RUISLIP, MIDDX, HA4 8BS
10. SPONSORING/MONITORING AGENCY REPORT NUMBER		
11. SUPPLEMENTARY NOTES		
12a. DISTRIBUTION/AVAILABILITY STATEMENT		12b. DISTRIBUTION CODE
This report is approved for public release. Distribution unlimited		
13. ABSTRACT (Maximum 200 words)		
<p>In this project, computer simulation and optical modeling of laser beam propagation through the turbulent atmosphere, as well as development of techniques using photorefractive crystals to mitigate phase distortions in laser beams, have been done. In the framework of the first direction the mathematical methods and computational schemes based on split-step operators, phase screen model and the Monte Carlo method have been elaborated. Spatial statistics of light field in laser beam has been studied in relation to inner and outer scales for different models of atmospheric turbulence. Regimes of weak, moderate and strong fluctuations have been considered. In the framework of the second direction the possibility of simulation of double pass and anisoplanatic effects by means of few phase screens has been studied. An experimental set-up for optical modeling anisoplanatic effects by the use of dynamic phase modulator has been designed. A method of generation of random optical field with variable correlation function has been proposed and tested. In the framework of the third direction the problem of mitigation of distorted optical signals in photorefractive crystals has been studied. An optimal effective operating range of one-way system, based on nonlinear interaction of distorted signal with pumping formed by spatial filtering of the signal, has been found. Using the criterion of maximal mitigation of phase and amplitude distortions, the schemes of two- and four-beam interaction in InP:Fe have been optimized.</p>		
14. SUBJECT TERMS		15. NUMBER OF PAGES
Laser beam, turbulent atmosphere, computer simulation, optical simulation, phase screen model, Monte Carlo method, double pass effects, liquid crystal spatial phase modulator, dynamic holography, photorefractive crystal, mitigation of phase distortions.		75
16. PRICE CODE		
17. SECURITY CLASSIFICATION OF REPORT	18. SECURITY CLASSIFICATION OF THIS PAGE	19. SECURITY CLASSIFICATION OF ABSTRACT
UNCLASSIFIED	UNCLASSIFIED	UNCLASSIFIED
20. LIMITATION OF ABSTRACT		

## **List of participants of the project**

1. Principal Investigator, Associate Professor S.S.Chesnokov
2. Co-principal Investigator, Professor V.P. Kandidov
3. Co-principal Investigator, Senior Researcher V.V. Shuvalov
4. Co-principal Investigator, Professor V.I. Shmalhausen
5. Technical Manager, Associate Professor B.V. Zhdanov
6. Technical Secretary N.G. Podkopaeva
7. Associate Professor S.A. Shlyonov
8. Associate Professor V.A. Vysloukh
9. Senior Researcher A.V. Koriabin
10. Senior Researcher V.M. Petnikova
11. Assistant Researcher N.G. Iroshnikov
12. Assistant Researcher T.A. Matveeva
13. Assistant Researcher I.V. Davletshina
14. Assistant Researcher O.G. Kosareva
15. Assistant Researcher A.V. Larichev
16. PhD Student X.V. Prokofieva
17. PhD Student I.V. Krupina
18. PhD Student A.N. Simonov
19. Student M. Tamarov
20. Student A. Skulacheva
21. Student S. Skipetrov
22. Student V. Kutuzov
23. Student D. Mamontov
24. Student D. Mazurin
25. Student N. Yaitskova

## **Abstract**

In this project, computer simulation and optical modeling of laser beam propagation through the turbulent atmosphere, as well as development of techniques using photorefractive crystals to mitigate phase distortions in laser beams, have been done. In the framework of the first direction the mathematical methods and computational schemes based on split-step operators, phase screen model and the Monte Carlo method have been elaborated. Spatial statistics of light field in laser beam has been studied in relation to inner and outer scales for different models of atmospheric turbulence. Regimes of weak, moderate and strong fluctuations have been considered. In the framework of the second direction the possibility of simulation of double pass and anisoplanatic effects by means of few phase screens has been studied. An experimental set-up for optical modeling anisoplanatic effects by the use of dynamic phase modulator has been designed. A method of generation of random optical field with variable correlation function has been proposed and tested. In the framework of the third direction the problem of mitigation of distorted optical signals in photorefractive crystals has been studied. An optimal effective operating range of one-way system, based on nonlinear interaction of distorted signal with pumping formed by spatial filtering of the signal , has been found. Using the criterion of maximal mitigation of phase and amplitude distortions, the schemes of two- and four-beam interaction in InP:Fe have been optimized.

## **List of keywords**

Laser beam, turbulent atmosphere, computer simulation, optical simulation, phase screen model, Monte Carlo method, double pass effects, liquid crystal spatial phase modulator, dynamic holography, photorefractive crystal, spatial filtration, mitigation of phase distortions.

## Table of contents

<b>Part I. Numerical simulation of laser beam propagation through atmospheric turbulence</b>	6
1. Introduction	6
2. Justification of the Monte Carlo method based on the phase screen model	7
2.1. Parabolic equation	7
2.2. Model of phase screens	8
2.3. The origin of the phase screen model	9
2.4. Phase screen model and split-step method	9
2.5. Statistical trials in optics of the turbulent atmosphere	10
3. Computer simulation of the phase screens	10
3.1. Problem of scales in atmospheric turbulence	10
3.2. FFT-based phase screen generation	11
3.3. Subharmonics model	14
3.4. Modal representation	15
4. Computer simulation of laser beam propagation	19
4.1. Spectral method	19
4.2. Criteria of the split-step method applicability	20
4.3. Flexible grid	23
5. The effect of large-scale refractive index fluctuations on the propagation of the beam through the turbulent atmosphere	25
5.1. Optimization of the phase screen model	25
5.2. The role of the outer scale	28
5.3. Random migrations of beam centroid	30
6. Small-scale turbulence	30
6.1. Field realizations	32
6.2. Coherence of light field	32
6.3. Distribution of the mean irradiance	38
6.4. Irradiance variance	40
6.5. Monte Carlo method and the scintillations theory of the effective beam parameters	41
7. Literature cited	43
<b>Part II. Optical simulation of laser beam propagation through the turbulent atmosphere</b>	46
1. Introduction	46
2. Theoretical background	47
3. Two phase screen method	48
4. Optical simulation technique for anisoplanatic and double pass effects investigation	49
5. Random optical field generation	50
6. Experimental results on random phase screen generation	52
7. Conclusion	53
8. Literature cited	54

**Part III. Photorefractive crystal (PRC) based technology for distortion mitigation in laser beams** 56

1. Mitigation of phase distortions by means of one-way mitigation system with formation of pumping wave from the distorted signal	56
1.1. Introduction	56
1.2. Description of the model	58
1.3. Results of calculations	61
1.4. Conclusions	66
1.5. Literature cited	66
2. Dynamic distortion suppression by phase conjugation systems based on photorefractive nonlinearity	67
2.1. Introduction	67
2.2. The model	67
2.3. Theory	69
2.4. Numerical results	70
2.5. Conclusions	73
2.6. Publications	73
2.7. Literature cited	73
List of publications	74
List of participating scientific personnel	75

# Part I

## Numerical Simulation of Laser Beam Propagation Through Atmospheric Turbulence

### 1. Introduction

When the laser beam propagates through the atmosphere it undergoes distortions, caused by fluctuations in the refractive index in turbulence. Random blurring of the beam and the loss of the spatial coherence are some of the factors which limit the effectiveness of the location, probing and imaging systems in the atmosphere.

Lately the Monte Carlo method has been intensively developed in application to the theoretical investigation of the laser beam propagation through the turbulent atmosphere. This method has considerable advantages over the analytical methods, which commonly use one or another set of approximations<sup>1</sup>. Rytov theory is applicable in the regime of weak fluctuations, when the scintillation index in the plane wave satisfies the condition  $\beta_0^2 \ll 1$ . The equations for the field moments are valid without restrictions on the strength of fluctuations<sup>2</sup>. However, for the kurtosis (the fourth moment), which describes irradiance variance and covariance, only approximate solutions may be obtained. The generalized Huygens-Fresnel's approach allows to obtain the mean irradiance, but the solution for the kurtosis diverges with the increasing Rytov variance  $\beta_0^2$ . The phase approximation in Huygens-Kirchhoff's method gives asymptotically strict solutions for the fluctuations of the focused beam in the regions  $\beta_0^2 \ll 1$  and  $\beta_0^2 \gg 1$  and for the fluctuations of the collimated beam only in the near-field region<sup>3</sup>. The interesting results have been obtained from the theory of effective beam parameters, developed in Ref. 4. The Monte Carlo method is, in principle, free from any limitations. Its accuracy is defined only by computing resources.

Optics of the atmosphere usually assumes two approaches in the development of the Monte Carlo method. One of them is known as corpuscular approach and the other as wave approach<sup>5,6</sup> (Fig. 1.1a). In corpuscular approach the propagation of the light wave through the atmosphere is considered as a stochastic process of the photon scattering by the molecules of the air components<sup>7</sup>. From the ensemble of several thousands of calculated trajectories the angular distribution and polarization of the scattered radiation<sup>8</sup> as well as the visibility of the object in the atmosphere<sup>9</sup> and the quality of imaging through the disperse medium<sup>10</sup> may be obtained.

The wave approach is based on the model of phase screens which imitate fluctuations of the permittivity in the turbulent atmosphere. The propagation of the laser radiation is considered as a process of successive scattering of the light wave by the phase screens (Fig. 1.1b). The numerical solution to the problem of the wave scattering yields the realization of the light field in the receiver plane. Physically, this realization is equivalent to the distribution of the light field registered in the receiver plane. A series of such solutions obtained for different sets of phase screens forms an ensemble of realizations of the light field. Statistical characteristics of the laser beam in the atmosphere are calculated by averaging over the ensemble of the obtained realizations.

The Monte Carlo method allows on the basis of a unified approach to investigate various statistical quantities, associated with beam propagation in turbulence, as well as various models of atmospheric turbulence and conditions of propagation.

The Monte Carlo method based on the phase screen model is widely used for the treatment of the problems of the wave propagation in various media. The method is applied to the analysis of the fluctuations which are observed in many situations of scientific interest, such as electromagnetic waves through atmospheres, ionospheres, acoustic waves in the ocean, seismic waves in the earth<sup>11</sup>.

The present paper is devoted to computer simulations of the statistics of the laser beam in the turbulent atmosphere on the basis of the phase screen model. This paper has two main parts. The first part (sections 2-4) will describe methodological aspects of the Monte Carlo method based on the phase screen model. We will consider the justification of the Monte Carlo method and the phase screen model, the methods of generating the phase screens, which may adequately represent atmospheric turbulence, and methods to solve the problem of scattering of the radiation by a set of phase screens.

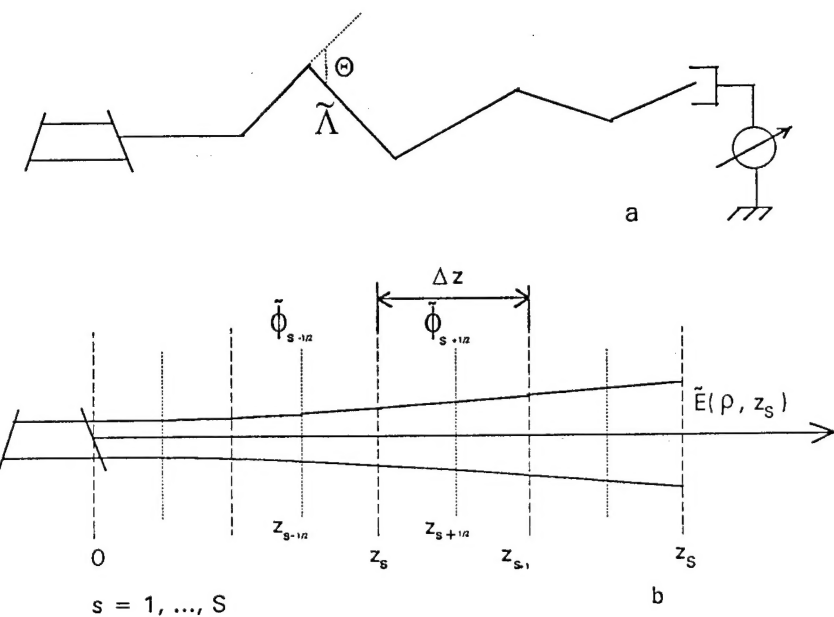


Fig. 1.1

The Monte Carlo method in a random media. a) The corpuscular approach. b) The wave approach on base of phase screen model.

The second part (sections 5-6) will discuss the results of the Monte Carlo simulations. We will consider the effect of the large-scale turbulence on random blur and wander of the laser beam and the effect of the small-scale turbulence on spatial statistics of the light field at the end of the atmospheric path. The effect of the model of atmospheric turbulence on statistical characteristics of the beam is estimated. The results obtained by Monte Carlo simulations and analytical methods are compared.

## 2. Justification of the Monte Carlo method based on the phase screen model

### 2.1. Parabolic equation

The wave approach in the Monte Carlo method is based on the parabolic equation for the complex amplitude of the light field  $E(\rho, z)$ , propagating in a randomly inhomogeneous medium:

$$2ik_0 \frac{\partial E}{\partial z} = \Delta_1 E + 2k_0^2 \bar{n}(\rho, z) E, \quad (2.1)$$

where  $k_0 = 2\pi/\lambda$  is a wave number,  $\bar{n}(\rho, z)$  is a three-dimensional field of the refractive index fluctuations in the medium.

Parabolic equation (2.1) is valid under the following assumptions<sup>12</sup>:

- spatial scales of fluctuations in the random medium  $L_e$  and in the light field  $r_k$  are much larger than the wavelength  $\lambda$  -

$$L_e, r_k \gg \lambda \quad (2.2)$$

- the Fresnel approximation may be used:

$$L_e^4, r_k^4 \gg \lambda^3 z \quad (2.3)$$

- the energy losses due to the backward scattering of the field by inhomogeneities of the medium are small:

$$\pi^2 k^2 z \int_{k\sqrt{z}}^{2k} \Phi_n(\kappa) \kappa d\kappa \ll 1 \quad (2.4)$$

When the light wave propagates through the atmosphere the conditions (2.2)-(2.4) are always satisfied.

The simultaneous fulfillment of the conditions (2.2)-(2.4) means that the scattered radiation propagates in the forward direction and the backward scattering may be neglected. This fact allows to introduce the propagation direction  $z$ , along which the light field amplitude  $E(\rho, z)$  variations are observed. The evolution of the radiation along the coordinate  $z$  obeys the principle of dynamic causality<sup>12</sup>. According to it, the propagation of the light beam is Markov process of successive passage of the slabs of randomly inhomogeneous atmosphere.

The representation of continuum as a set of slabs has been used in the local method of small perturbations<sup>13</sup>. From this method the equations for the field moments may be immediately obtained.

## 2.2. Model of phase screens

The further development of the stratified representation of continuum is a model of phase screens. In this model each slab of length  $\Delta z$  is effectively compressed to a phase screen located at the slab center. At a distance  $\Delta z/2$  to the right and to the left from the phase screen only diffraction in free space is considered (Fig. 1.1b). Randomly inhomogeneous continuum is replaced by a set of phase screens located along the propagation direction. The distance between the screens is  $\Delta z$ , the first and the last screen are located at a distance  $\Delta z/2$  from the transmitter and receiver planes respectively.

Thus, fluctuations in the refractive index of the atmosphere induce fluctuations in the phase of the light field  $\tilde{\varphi}_{s+1/2}(\rho)$ . These fluctuations are located on the infinitely thin phase screens in the planes  $z_{s+1/2}$ . Between the screens phase fluctuations transform to amplitude fluctuations owing to diffraction.

Such a set of a finite number of phase screen is a good model of randomly inhomogeneous continuum, if the length  $\Delta z$  between the screens is small in comparison with the diffraction length  $L_d$  and extinction length  $\alpha^{-1}$ .

$$\Delta z < \min\{L_d, \alpha^{-1}\}, \quad \Delta z = z_s - z_{s-1}, \quad (2.5)$$

where  $L_d = kr_k^2$  - is diffraction length corresponding to the characteristic scale of the light field inhomogeneity,  $\alpha$  is the extinction coefficient.

When the condition (2.5) is satisfied the phase fluctuation on the phase screen can be obtained from the geometrical optics approximation:

$$\tilde{\varphi}_{s+1/2}(\rho) = k \int_{z_s}^{z_{s+1}} \tilde{n}(\rho, \xi) d\xi. \quad (2.6)$$

If the length of a slab  $\Delta z$  exceeds the outer scale of turbulence  $L_0$

$$\Delta z \gg L_0, \quad (2.7)$$

then the model of  $\delta$ -correlated relative to  $z$  fluctuations of the refractive index is valid. For statistically isotropic field of atmospheric turbulence the spatial spectrum  $F_\varphi(k_1)$  of the random phase  $\varphi(\rho)$  on the screen may be expressed as follows:

$$F_\varphi(k_1) = 2\pi k_0^2 \Delta z \Phi_n(k_1, 0), \quad (2.8)$$

where  $\Phi_n(k_1, \kappa_z)$  is a three-dimensional spectrum of the refractive index fluctuations in the atmosphere.

The variance  $\sigma_\varphi^2$  of the phase fluctuations on the screen is given by:

$$\sigma_\varphi^2 = 2\pi k_0^2 \Delta z \int_0^\infty \Phi_n(k_1, 0) k dk \quad (2.9)$$

For Gaussian field  $\tilde{n}(\rho, z)$  the condition (2.7) means that phase fluctuations  $\tilde{\varphi}(\rho)$  on different screens are statistically independent:

$$\langle \tilde{\varphi}_{s+1/2}(\mathbf{r}) \tilde{\varphi}_{s'+1/2}^*(\mathbf{r}) \rangle = \sigma_\varphi^2 \cdot \delta_{ss'}. \quad (2.10)$$

When considering the wind flow, one commonly uses the hypothesis of the "frozen turbulence". In this case the field  $\tilde{\varphi}(\rho)$  satisfies the condition:

$$\tilde{\varphi}_{s+1/2}(\rho, t) = \tilde{\varphi}_{s+1/2}(\rho - \mathbf{V}_\perp t, 0), \quad (2.11)$$

where  $\mathbf{V}_\perp$  is the wind flow velocity in the plane of the screen.

### 2.3. The origin of the phase screen model

The simplest model containing one phase screen reflects the main properties of the wave in randomly inhomogeneous medium. This model allows to qualitatively estimate statistical properties of the wave in random medium. Presumably, the model of phase screen was first used in Ref. 14 for the analysis of the wave diffraction in a thick slab of randomly inhomogeneous medium. The theory of the wave diffraction behind a thin screen with random phase and amplitude fluctuations was thoroughly considered in Ref. 15. The physical situation, which is most adequately described by one phase screen, is scattering of the wave in a thin slab, when fluctuations of the light field are formed behind the slab. In particular, this situation may occur when the wave propagates through the ionosphere<sup>15</sup> and interplanetary plasma<sup>16</sup>.

The error of the representation of the continuum by one phase screen has been studied in Ref. 17 on the basis of numerical solution of the for the field kurtosis. When the length of the medium exceeds the outer scale  $L_0$ , one phase screens significantly overestimates irradiance fluctuations in the absence of saturation. The error of the model essentially decreases if the screen is located at the center of the path.

The first statistical trials with the waves scattered by the phase screen have been done in Ref. 18. The authors<sup>18</sup> discuss methodological questions of spectral analysis of stochastic waves diffraction and illustrate the methods by the example of propagation through a thin layer of anisotropic ionosphere. The distribution function of the irradiance fluctuations in the plane wave behind a thin turbulent layer was studied in Ref. 19 on the basis of the model with one phase screen. Ten thousand realizations showed that Rice-Nakagami and log-normal distributions may not be applied to the description of irradiance fluctuations.

The model based on a set of phase screens is substantially more reliable for the reproduction of randomly inhomogeneous continuum. The application of this model is equivalent to the representation of the kurtosis of the field as a convolution for the continuum<sup>20</sup>. In the plane wave coherence function integration in the exponent is replaced by summation when the phase screen method is applied<sup>21</sup>.

The application of the phase screen model to analytical study of the wave propagation in randomly inhomogeneous media is thoroughly discussed in Refs. 6, 11.

Statistical study of the wave propagation in randomly inhomogeneous media on the basis of the phase screen model implies the application of the split-step method to solve stochastic parabolic equation (2.1).

### 2.4. Phase screen model and split-step method

In fact, the phase screen model for randomly inhomogeneous medium is physical interpretation of split-step method, which is well known in computational mathematics<sup>22</sup>. In this method the differential equation with some operator, which can be written as a linear sum of several pieces, at each step  $\Delta z$  is replaced by a sequence of equations corresponding to the pieces in the sum. This approach allows to use the most effective differencing schemes for each equation from the sequence. It has been shown<sup>23</sup> that the split-step method allows to reduce computing time by as much as 30 percents in comparison with the time needed for the direct solution of the stochastic equation (2.1) for randomly inhomogeneous medium. When handling diffraction problems Fast Fourier Transform algorithm is found to especially increase effectiveness of the split-step method in the conditions of strong fluctuations.

The idea to use the split-step method for treatment of the wave propagation in randomly inhomogeneous and nonlinear media was first suggested in Ref. 24. One of the first practical applications of this step method was associated with investigation of the effect of the internal waves on distortions of acoustic signal in underwater sound channel<sup>25</sup>. In optics of the turbulent atmosphere the split-step method has become widespread after Ref. 26 had been published. In Ref. 26 separate realizations of a powerful laser beam traveling through the atmosphere were obtained.

The current state concept of the split-step method and ways for constructing the splitted operators for the problems of the optical wave propagation in randomly inhomogeneous medium are reviewed in Ref. 27.

For the parabolic equation (2.1) the split-step method applied to a slab  $\Delta z$  of the medium yields the following set of equations:

$$2ik_0 \frac{\partial \tilde{E}_d}{\partial z} = \Delta_\perp E_d, \quad z \in [z_s, z_{s+1/2}], \quad \text{for } \tilde{E}_d(\rho, z_s) = \tilde{E}(\rho, z_s); \quad (2.12)$$

$$2ik_0 \frac{\partial \tilde{E}_\epsilon}{\partial z} = 2k_0^2 \tilde{n} \tilde{E}_\epsilon, z \in [z_s, z_{s+1}] \text{ for } \tilde{E}_\epsilon(\rho, z_s) = \tilde{E}_d(\rho, z_{s+1/2}); \quad (2.13)$$

$$2ik_0 \frac{\partial \tilde{E}_d}{\partial z} = \Delta_\perp E_d, z \in [z_{s+1/2}, z_{s+1}], \text{ for } \tilde{E}_d(\rho, z_{s+1/2}) = \tilde{E}_\epsilon(\rho, z_{s+1}). \quad (2.14)$$

The solution of the last equation is the final solution of the equation (2.1) in the plane  $z_{s+1}$ :  $\tilde{E}_d(\rho, z_{s+1}) = \tilde{E}(\rho, z_{s+1})$ .

Equations (2.12) and (2.14) describe the diffraction of the wave in homogeneous field at a distance  $\Delta z/2$  to the left and to the right of the screen, located in the plane  $z_{s+1/2}$ . Equation (2.13) describes the scattering of the wave by inhomogeneities in geometric optics approximation. Its solution is

$$\tilde{E}_\epsilon(\rho, z_{s+1}) = \tilde{E}_\epsilon(\rho, z_s) e^{i\tilde{\varphi}_{s+1/2}(\rho)}, \quad (2.15)$$

where  $\tilde{\varphi}_{s+1/2}(\rho)$  is the phase perturbation on the screen (2.6).

In the next slab  $[z_{s+1}, z_{s+2}]$  we sequentially solve equations describing diffraction and scattering of the wave by a phase screen. This procedure repeats over and over again from transmitter plane  $z=0$  to receiver plane  $z=z_s$ .

It is common practice to combine equations describing diffraction in two adjacent slabs. As a result diffraction of the wave is considered on the interval  $[z_{s-1/2} + 0, z_{s+1/2} - 0]$ , i.e. between two neighboring screens.

### *2.5. Statistical trials in optics of the turbulent atmosphere*

First papers dealing with the Monte Carlo method based on the phase screen approach are related to investigations of statistical characteristics of the powerful laser beams in the turbulent atmosphere. In Ref. 28 a time-dependent calculation of spatial statistics of irradiance fluctuations of the beam propagating through the atmosphere under the conditions of thermal self-action has been done. Irradiance fluctuations of the laser beam in the presence of wind are considered in Ref. 29. The effect of the wind velocity fluctuations on random motion and blurring of the beam propagating in the presence of nonlinear refraction is discussed in Refs. 30,31.

Recently much attention has been paid to the linear problems of statistical optics of the turbulent atmosphere. Here the propagation is described by the equation (2.1). A series of Refs. 32-34 have been devoted to the investigation of the plane and spherical light waves statistics. In Ref. 32 strong fluctuations of the plane wave irradiance are considered, the Ref. 33 investigates the convergence of asymptotic solutions for irradiance moments in the regimes of strong  $\beta_0^2 \geq 10$  and complete  $\beta_0^2 \geq 10$  saturation of fluctuations. In Ref. 34 simple empirical formulas have been obtained for the dependence of irradiance variance on the inner scale in the regime of strong focusing. The Ref. 35 is devoted to investigation of the distribution function of irradiance fluctuations in the plane and spherical waves.

## 3. Computer simulations of the phase screens

### *3.1. Problem of scales in atmospheric turbulence*

According to the modern concepts the microstructure of atmospheric turbulence is determined by the cascade process of fragmentation of eddies that arise in the wind flow<sup>36</sup>. The size of the large-scale eddies  $L_0 \ll r \ll L_0$  is comparable to the characteristic scale of the entire wind flow. The size of the small-scale eddies  $l_0$  corresponds to the size of perturbations at which the dissipation of energy through viscous effects becomes important. The inertial subrange of atmospheric turbulence is bounded by the outer  $L_0$  and inner  $l_0$  scales

$$l_0 \ll r \ll L_0 \quad (3.1)$$

Structure functions of the random temperature field and consequently the refractive index field obey within the inertial subrange the two-third law<sup>2</sup>:

$$D_a(r) = C_a^2 r^{2/3}, \quad l_0 \ll r \ll L_0 \quad (3.2)$$

where  $C_a^2$  is the structure constant of the refractive index fluctuations in the atmosphere. This structure function corresponds to the three-dimensional Kolmogorov spectrum  $\Phi_a^K(\kappa)$  that has a power dependence on the wave number  $\kappa^2$ :

$$\Phi_a^K(\kappa) = 0.033 C_a^2 \kappa^{-11/3}, \quad \kappa_0 \ll \kappa \ll \kappa_I \quad (3.3)$$

where  $\kappa_I = 2\pi/l_0$ ,  $\kappa_0 = 2\pi/L_0$  are the boundaries of the spatial spectrum corresponding to the inertial subrange.

The Kolmogorov spectrum satisfactorily describes the fluctuations of the refractive index in the atmosphere within the inertial subrange. However, the behavior of the fluctuations at the boundaries and outside of the inertial subrange requires some additional assumptions. The following models take into account the effect of the boundaries in an explicit form:

the Tatarskii spectrum considers the effect of the inner scale

$$\Phi_a^T(\kappa) = 0.033 C_a^2 \kappa^{-11/3} e^{-\kappa^2/\kappa_m^2}, \quad \kappa_m = 5.92/l_0 \quad (3.4)$$

the von Karman spectrum considers the effect of the outer scale

$$\Phi_a^{VK}(\kappa) = 0.033 C_a^2 (\kappa^2 + \kappa_0^2)^{-11/6}, \quad (3.5)$$

the modified von Karman

$$\Phi_a^{MK}(\kappa) = 0.033 C_a^2 (\kappa^2 + \kappa_0^2)^{-11/6} e^{-\kappa^2/\kappa_m^2}, \quad \kappa_m = 5.92/l_0 \quad (3.6)$$

and the Andrews spectra

$$\Phi_a^A(\kappa) = 0.033 C_a^2 \left[ 1 + 1.802 \left( \frac{\kappa}{\kappa_s} \right) - 0.254 \left( \frac{\kappa}{\kappa_s} \right)^{7/6} \right] \frac{e^{-\kappa^2/\kappa_s^2}}{(\kappa^2 + \kappa_0^2)^{11/6}}, \quad \kappa_s = 3.3/l_0 \quad (3.7)$$

consider the effect of both inner and outer scales

Typically, the scale sizes of turbulent eddies vary from an outer scale of tens of meters down to an inner scale of just a few millimeters. In other words, the range of spatial perturbations of the refractive index in the atmosphere is extremely wide: the ratio between the inner and the outer scales may reach several orders of magnitude. In numerical implementations,  $\kappa_I$  may be often ignored, because the ratio of  $\Phi_a(\kappa_0, z)/\Phi_a(\kappa_I, z)$  or the dynamic range of the spectrum to be simulated is several orders of magnitude as well. Hence, the effect of the roll-off due to the presence of  $\kappa_I$  in the model will most likely not be noticed.

In the phase screen model we use the 2D power spectrum of a thin slab of turbulence in a plane orthogonal to the direction of propagation (the  $z$  axis). This spectrum is given by (3.8)

$$F(\kappa_{\perp}) = 2\pi k_0^2 \Delta z \Phi_a(\kappa_{\perp}, 0) \quad (3.8)$$

where  $\Phi_a(\kappa_{\perp}, 0)$  is 2D power spectrum of the refractive index fluctuations, which corresponds to one of the models of atmospheric turbulence.

### 3.2. FFT-based phase screen generation

The traditional method of generating random fields with the known autocorrelation function (the phase screens under discussion also belong to this case) is filtering a white noise process with square root of the spectrum, followed by an inverse Fourier transform. This spectral method is highly efficient, because it allows to take advantage of the fast Fourier transform (FFT) algorithm.

In this method the complex field  $\phi(n, m)$  is represented on the screen as a sum of Fourier harmonics with random complex coefficients (discrete white noise):

$$\phi(n, m) = \frac{1}{\sqrt{N_x N_y}} \sum_{p=-N_x/2+1}^{N_x/2} \sum_{q=-N_y/2+1}^{N_y/2} a_{pq} (\xi_{pq} + i\eta_{pq}) W_{N_x}^{pn} W_{N_y}^{qm},$$

$$a_{pq} = \sqrt{F_\varphi(p, q) \Delta \kappa_x \Delta \kappa_y}, \quad W_{N_x} = \exp\left\{i \frac{2\pi}{N_x}\right\}, \quad W_{N_y} = \exp\left\{i \frac{2\pi}{N_y}\right\}, \quad (3.9)$$

where  $\xi_{pq}, \eta_{pq}$  are statistically independent random numbers which are either Gaussian with parameters  $(0, 1)$  or uniformly distributed on the interval  $[-\sqrt{6}/2, \sqrt{6}/2]$ . In the last case the generated phase screens have Gaussian statistics owing to the central limit theorem<sup>37</sup>. Through  $F_\varphi(p, q) = F_\varphi(\kappa_p, \kappa_q)$  we denote the values of the two-dimensional spectrum of the phase, where spatial frequencies  $\kappa_p$  and  $\kappa_q$  are defined by

$$\begin{aligned} \kappa_p &= \Delta \kappa_x p & p &= -N_x/2, \dots, N_x/2 - 1, \\ \kappa_q &= \Delta \kappa_y q & q &= -N_y/2, \dots, N_y/2 - 1, \end{aligned} \quad (3.10)$$

Frequency intervals between harmonics  $\Delta \kappa_x$  and  $\Delta \kappa_y$  are given by

$$\Delta \kappa_x = 2\pi/A_x, \quad \Delta \kappa_y = 2\pi/A_y, \quad (3.11)$$

where  $A_x = N_x \Delta x$  and  $A_y = N_y \Delta y$  are the sizes of the simulation aperture. Real and imaginary parts of the generated field  $\varphi(n, m)$  form two statistically independent realizations of the phase screen

$$\begin{aligned} \{\varphi(n, m) &= \operatorname{Re} \varphi(n, m), \quad n = 1, \dots, N_x, \quad m = 1, \dots, N_y\}, \\ \{\varphi'(n, m) &= \operatorname{Im} \varphi(n, m), \quad n = 1, \dots, N_x, \quad m = 1, \dots, N_y\} \end{aligned} \quad (3.13)$$

Algorithm (3.9) assumes that  $p$  and  $q$  may be equal to zero. In this case the weighting coefficient  $a_{pq}$  is equal to the value of zero harmonic  $F_\varphi(0, 0)$  of the spectrum. For the Kolmogorov (3.3) and Tatarskii (3.4) spectra of atmospheric turbulence  $F_\varphi \rightarrow \infty$  as  $\kappa \rightarrow 0$ . Taking into account that the average phase delay has no effect on the image formation process or a beam propagation, the origin of the filter function can be set to zero,  $a_{00} = 0$ .

The two-dimensional field of the phase fluctuations and its covariance and structure functions are represented by their values at the discrete spatial domain points  $n, m$ . The spectrum of the field is represented by its values at the discrete spectral domain points  $\kappa_p, \kappa_q$ . Therefore, the phase covariance function  $B_\varphi(n, m)$  and its spectrum  $F(p, q)$  are related by the discrete Fourier transform

$$B_\varphi(n, m) = \sum_{p=-N_x/2+1}^{N_x/2-1} \sum_{q=-N_y/2+1}^{N_y/2-1} F(p, q) \Delta \kappa_x \Delta \kappa_y W_{N_x}^{-np} W_{N_y}^{-mq} \quad (3.14)$$

Eq. (3.14) defines the simulated (which can be simulated on the numerical grid) phase covariance function for the chosen spectrum of atmospheric turbulence  $F_\varphi(\kappa_x, \kappa_y)$ . The simulated structure function is given by

$$D_\varphi(n, m) = 2(B_\varphi(0, 0) - B_\varphi(n, m)) \quad (3.15)$$

A deviation of the simulated statistical characteristics from the desired ones forms a systematic error of the phase screens. Typically, phase screens are evaluated by how well they reproduce the desired phase structure function for the given turbulence model. For the Kolmogorov turbulence the phase structure function has the form (3.2). When discussing methods of generating the phase screens, in parallel with the Kolmogorov spectrum (3.3) we will consider the von Karman spectrum (3.5). For the case of a finite outer scale the phase structure function is given by

$$D_n^{\text{VK}}(r) = 0.308 C_n^2 L_0^{2/3} \left[ 1 - \frac{2^{2/3}}{\Gamma(1/3)} (r \kappa_0)^{1/3} Y_{1/3}(r \kappa_0) \right] \quad (3.16)$$

where  $Y_{1/3}(r \kappa_0)$  is the Neumann function of the order of  $1/3$  of the imaginary argument.

Generation of random screens according to the algorithm (3.9) can be easily performed using the FFT method. However, this fast and effective approach has its own limitations. The minimum and maximum spatial frequencies of the screens generated by the FFT are  $\kappa_{\min} = \Delta\kappa = 2\pi / A$  and  $\kappa_{\max} = N\Delta\kappa / 2 = \pi / \Delta x$ .

Correspondingly, the minimum representable scale size is  $r_0 = 2\Delta x = 2\pi / \kappa_{\max}$ . Thus, if one wants to reproduce on the grid the minimum inhomogeneity of the order of 10mm and if the number of grid points for one of the transverse coordinates is 128, than the maximum reproducible scale on the grid is 0.64 m. In most cases this is not enough for adequate reproduction of the large scale fluctuations ( $\sim L_0$ ) of the refractive index since typically  $L_0$  is much larger than 0.6m.

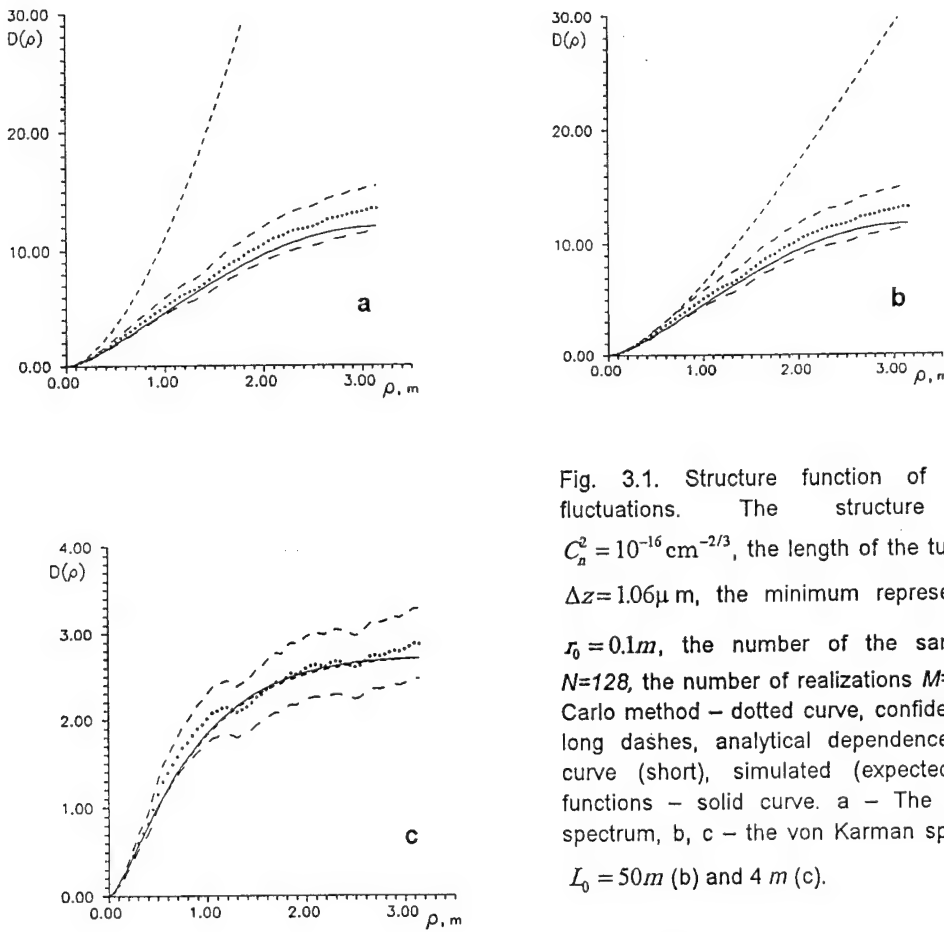


Fig. 3.1. Structure function of the phase fluctuations. The structure constant  $C_a^2 = 10^{-16} \text{ cm}^{-2/3}$ , the length of the turbulent slab  $\Delta z = 1.06 \mu\text{m}$ , the minimum representable size  $r_0 = 0.1 \text{ m}$ , the number of the sample points  $N=128$ , the number of realizations  $M=100$ . Monte Carlo method – dotted curve, confidence limits – long dashes, analytical dependence – dashed curve (short), simulated (expected) structure functions – solid curve. a – The Kolmogorov spectrum, b, c – the von Karman spectrum with  $L_0 = 50 \text{ m}$  (b) and  $4 \text{ m}$  (c).

Fig. 3.1 shows the structure functions of phase fluctuations on the screen obtained by the FFT-based method. The averaging has been done

over 100 screens. It is clearly seen that analytical dependences lie essentially upper than the curves obtained through Monte Carlo simulations as well as than the values of structure function expected on the grid. This is valid for both the Kolmogorov (Fig. 3.1a) and the von Karman (with large outer scale) (Fig. 3.1b) spectra. A satisfactory agreement between the analytical and simulated structure functions is obtained only when the step of the grid becomes comparable with the outer scale of turbulence (Fig. 3.1c). The reason for the discrepancies shown in Figs. 3.1 a, and b is that the tilt and other manifestations of the large-scale turbulence are not correct on this screen. In other words, the grid does not adequately reproduce the low-frequency characteristics of atmospheric turbulence.

### 3.3. Subharmonics method

The discussed limitations essentially deteriorate the performance of the FFT-based methods of generating the phase screens. In a series of papers<sup>38-40</sup> some attempts have been done to modify the original method so that it could take into account the effect of large-scale phase fluctuations within the limited aperture.

Following<sup>40</sup> let us consider the possibility to add low-frequency information using subharmonics. The method is based on the following idea. The power spectral density  $F_\varphi(\kappa_x, \kappa_y)$  of the phase fluctuations in the vicinity of zero is sampled with the smaller sampling interval than at the rest (high-frequency) part of the spectrum. Subsequent application of this procedure leads to the algorithm of increasing (in the vicinity of zero) sampling density or decreasing sampling interval of spatial frequencies. In this case the generation of the phase screen consists of several steps.

The first step assumes the generation of the phase screen  $\varphi_h(n, m)$  using conventional FFT-based method. However, before making inverse Fourier transformation (3.9) harmonics  $F_\varphi(p, q)$  are modified so that the points at indices  $(\pm 1, 0)$  and  $(0, \pm 1)$  are scaled by a factor of 1/2 and the points at indices  $(\pm 1, \pm 1)$  are scaled by a factor of 3/4. The obtained field  $\varphi_h(n, m)$  represents the high-frequency part of the phase fluctuations on the screen.

In the second step the low-frequency part of the spectrum is formed according to algorithm:

$$\begin{aligned} \varphi_l(n, m) = & \frac{1}{\sqrt{N_x N_y}} \sum_{j=1}^{N_j} \sum_{p'=-3}^2 \sum_{q'=-3}^2 a_{p'q'} (\xi_{p'q'} + i\eta_{p'q'}) \exp \left\{ 2\pi i 3^{-j} \left( \frac{(p'+0.5)m}{N_x} + \frac{(q'+0.5)n}{N_y} \right) \right\}, \\ a_{p'q'} = & 3^{-j} \sqrt{F_\varphi(\kappa'_x, \kappa'_y)} \Delta \kappa'_x \Delta \kappa'_y \end{aligned} \quad (3.17)$$

where  $\kappa'_x = 3^{-j}(p'+0.5)\Delta \kappa_x$  and  $\kappa'_y = 3^{-j}(q'+0.5)\Delta \kappa_y$ . The values of harmonics  $F_\varphi(\kappa'_x, \kappa'_y)$  with indices  $(-1, -1), (0, -1), (-1, 0)$  and  $(0, 0)$  are set to zero for all  $j$  except for  $j = N_j$ . The number  $N_j$  defines the number of iterations of increasing sampling density.

For each iteration sampling interval in the spatial frequency domain decreases by a factor of 3. The larger the number of iterations the closer to zero frequency are harmonics in the sum (3.17).

The resulting phase screen  $\varphi(n, m)$  may be obtained as a sum of its low- and high-frequency components,  $\varphi(n, m) = \varphi_h(n, m) + \varphi_l(n, m)$ .

Fig. 3.2 demonstrates the results of statistical processing of the phase screens obtained by subharmonics method. The number of points on the screen is the same as in the FFT-based method. One can see that the increased sampling density has resulted in the structure functions which are very closed to those predicted by the theory. An excellent agreement is obtained for the Karman spectrum with the outer scale  $L_0 = 50m$ .

In the case of the Kolmogorov spectrum the results of Monte Carlo simulations are essentially closer to the theoretically predicted as compared to those obtained by the conventional FFT method (Fig. 3.1a). The agreement may be further improved by increasing the number of iterations  $N_j$ . However, we have to keep in mind that with increasing number of iterations the round-off error also increases since  $F_\varphi(\kappa_x, \kappa_y) \rightarrow \infty$  when  $\kappa \rightarrow 0$ .

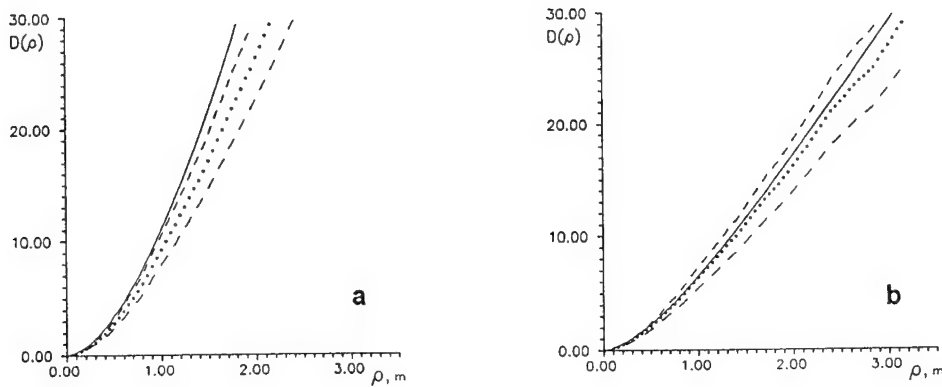


Fig. 3.2. Structure function of the phase fluctuations on the screens generated by subharmonic method.  $N_j=4$ . Parameters are the same as in Fig. 3.1. Solid curve – analytical dependence, a – the Kolmogorov spectrum, b – the von Karman spectrum with  $L_0 = 50 \text{ m}$ .

A limitation of this method is its low efficiency. Since the FFT algorithm is not used when the low-frequency part of the spectrum (3.17) is constructed, the computing time may increase by an order of magnitude in comparison with the FFT-based method, even if the number of realization is not too large.

### 3.4. Modal representation

Along with the spectral method, there exist alternative techniques for generating phase screens. One of them is modal representation. In contrast to the spectral method, in which sines and cosines form orthonormal basis for the decomposition of phase fluctuations, the modal method employs another set of orthonormal functions. For phase fluctuations in the turbulent atmosphere the most appropriate basis is formed by Zernike polynomials. The analytical definition of these polynomials is not unique since there is a choice with respect to the numbering sequence and the selection of an appropriate amplitude factor. We will use the definition convenient from the point of view of a statistical analysis<sup>41</sup>:

$$\left. \begin{aligned} Z_{even \ j} &= \sqrt{n+1} R_n^m(r) \sqrt{2} \cos(m\theta) \\ Z_{odd \ j} &= \sqrt{n+1} R_n^m(r) \sqrt{2} \sin(m\theta) \end{aligned} \right\} \quad m \neq 0, \quad (3.18)$$

$$Z_j = \sqrt{n+1} R_n^0(r), \quad m = 0$$

where

$$R_n^m(r) = \sum_{s=0}^{(n-m)/2} \frac{(-1)^s (n-s)!}{s! [(n+m)/2-s]! [(n-m)/2-s]!} r^{n-2s} \quad (3.19)$$

The values of  $n$  and  $m$  are always integer and satisfy  $m \leq n$ ,  $n - |m| = \text{even}$ . The index  $j$  is a mode ordering number and is a function of  $n$  and  $m$ .

The main advantage of Zernike polynomials (3.18) is their ability to represent phase fluctuations in terms of classical aberrations observed in the turbulent atmosphere. The first Zernike polynomial  $Z_1$  reproduces the average random phase growth on the aperture  $R$ , the second and the third ( $Z_2$  and  $Z_3$ ) describe random tilt, the fourth ( $Z_4$ ) - random defocus. The Zernike polynomial expansion of random phase fluctuations on the screen over a circle of radius  $R$  is given by:

$$\varphi(R\rho, \theta) = \sum_j a_j Z_j(\rho, \theta) \quad (3.20)$$

with  $\rho = r/R$  and the coefficients  $a_j$  being given by

$$a_j = \int d\rho^2 \rho W(\rho) \varphi(R\rho, \theta) Z_j(\rho, \theta), \quad (3.21)$$

where

$$W(\rho) = \begin{cases} 1/\pi, & \rho \leq 1 \\ 0, & \rho > 1 \end{cases} \quad (3.22)$$

Statistical properties of coefficients  $a_j$  depend on the characteristics of the wavefront  $\varphi(R\rho, \theta)$  to be expanded. In the case under discussion  $a_j$  are Gaussian random numbers with zero mean and given variance. The covariance matrix of these coefficients is defined by:

$$C_{jj'} = \langle a_j^* a_{j'} \rangle = \int d\rho \int d\rho' W(\rho) W(\rho') Z_j(\rho, \theta) \langle \varphi(R\rho, \theta) \varphi(R\rho', \theta') \rangle Z_{j'}(\rho', \theta'). \quad (3.23)$$

In frequency domain we have:

$$C_{jj'} = \langle a_j^* a_{j'} \rangle = \int dk \int dk' Q_j^*(k, \phi) \Phi_s(k/R) \delta(k - k') Q_{j'}(k', \phi'), \quad (3.24)$$

where  $Q_j(k, \phi)$  is the Fourier transform of  $Z_j(\rho, \theta)$ . The function  $Q_j(k, \phi)$  can be written from Eq.(3.18) as<sup>41</sup>:

$$\begin{aligned} Q_{even\ j}(k, \phi) &= \left[ (-1)^{(n-m)/2} i^m \sqrt{2} \cos(m\phi) \right] \\ Q_{odd\ j}(k, \phi) &= \left[ \sqrt{n+1} \frac{J_{n+1}(2\pi k)}{\pi k} (-1)^{(n-m)/2} i^m \sqrt{2} \sin(m\phi) \right], \\ Q_j(k, \phi) &= \left[ (-1)^{n/2}, \quad (m=0) \right] \end{aligned} \quad (3.25)$$

where  $J_l(x)$  is the  $l$ th order Bessel function of the first kind.

The expressions for the covariance matrix  $C$  may be obtained analytically only for the Kolmogorov model of atmospheric turbulence (3.3)<sup>41</sup>. For other models numerical integration of the expression (3.24) should be performed.

Although the Zernike polynomials form an orthonormal basis, it follows from the Eq.(3.23) that in the general case coefficients  $a_j$  are not statistically independent. The latter makes the generation of phase screens using Zernike expansion significantly more complicated. The requirement of statistical independency imposed on coefficients  $a_j$  in combination with the requirement on polynomials to be orthonormal, leads to the system of Karhunen-Loeve equations:

$$\begin{cases} \int d\rho \int d\rho' \tilde{Z}_j(\rho, \theta) \tilde{Z}_{j'}(\rho', \theta') = \delta_{jj'} \\ \int d\rho \int d\rho' \tilde{Z}_j(\rho, \theta) \langle \varphi(R\rho, \theta) \varphi(R\rho', \theta') \rangle \tilde{Z}_{j'}(\rho', \theta') = \delta_{jj'} \end{cases}. \quad (3.26)$$

Thus, the Zernike polynomials are not orthonormal, while the Karhunen-Loeve functions  $\tilde{Z}_j$  are not convenient since they cannot be expressed analytically.

In the present paper we suggest the following method of generating random fields with given spatial spectrum. The method is based on the Zernike polynomial expansion of the Karhunen-Loeve functions<sup>42</sup>. Let

$A = \begin{pmatrix} a_2 \\ a_3 \\ \dots \\ a_j \end{pmatrix}$  be the desired vector the components of which are the random coefficients for the Zernike

polynomials. The covariance matrix  $C = E[A \cdot A^T]$  may be obtained by numerical integration of the Eq.(3.24)

the Karhunen-Loeve functions, one should diagonalize the matrix  $C$ . It is known, that the symmetric quadratic matrix may be diagonalized by similarity transformation  $S = U \cdot C \cdot U^T$ , where  $U$  is a unitary matrix. Here diagonal elements of the matrix  $S$  are eigenvalues of the matrix  $C$ , while the columns of the matrix  $U$  are eigenvectors of the initial matrix. However, if there exists identical eigenvalues of the matrix  $C$ , not any matrix  $U$  may be used for the diagonalization of the matrix  $C$ . In our case the modes with the same radial degrees have identical eigenvalues. At the same time it can be easily verified that  $\langle a_j^* a_j \rangle \neq 0$  if the corresponding polynomials have identical angular dependence. This fact allows to group the coefficients, which are correlated, in clusters and apply the diagonalization algorithm within clusters. The problem of eigenvectors disappears automatically since the polynomials with identical angular dependence have different radial degrees.

After the diagonalization of matrix  $C$  we easily obtain the vector of random Karhunen-Loeve coefficients  $B$ , components of which are Gaussian random variables with zero mean and variance, given by the diagonal matrix  $S$ . The components of the vector  $A$  can be computed from the relation  $A = U^T \cdot B$ . These components  $a_j$  multiplied by  $(2R/r_0)^{5/6}$ , where  $r_0 = 1.68(C_a^2 K^2 \Delta z)^{-3/5}$  is the Fried radius, give rise to the weights for evaluating the Zernike polynomials with correct variance and covariance.

Statistical properties of the screens, obtained from the modal method (3.20), have been verified by analysis of structure functions of phase fluctuations on these screens. Parameters of turbulence and grid are as follows:

$C_a^2 = 10^{-15} \text{ cm}^{-2/3}$ ,  $\lambda = 0.53 \mu\text{m}$ ,  $\Delta z = 50 \text{ m}$ ,  $N_x = N_y = 128$ , the number of the Zernike polynomials  $J$  varied from 2 to 104. The averaging has been performed over  $M=300$  screens.

In order to make sure that the phase screens are statistically homogeneous and isotropic, we computed the structure function in several cross-sections of the screen. Fig. 3.3 shows three structure functions, two of which have been computed along the  $x$ - and  $y$ - axes, while the third - along the chord  $y=1/3 R_0$ . The comparison of these dependences allows to conclude that statistical homogeneity and isotropy of the obtained phase screens are quite good.

The behavior of the structure function for different numbers of Zernike polynomials used for the expansion is shown in Fig. 3.4. It demonstrates that within the confidence limits the structure functions coincide with exact solution. Note, that the first two Zernike polynomials make a main contribution to the phase fluctuations. The contribution of higher order polynomials, responsible for the small-scale fluctuations, becomes significant at the distances which are small as compared to the aperture size. Fig. 3.5 demonstrates that the structure function approaches exact solution as the number of the Zernike polynomials increases. Thus, the implementation of the modal method with sufficiently large number of the Zernike polynomials ( $\geq 100$ ) is expected to allow consideration of the effects of large-scale as well as small-scale turbulence on statistical characteristics of the laser beam, propagating through the atmosphere.

Since the structure function of phase fluctuations for the Kolmogorov spectrum has a power dependence on distance of the type  $D = ar^b$ , where  $a=0.10$  and  $b=1.67$  (for the parameters under consideration), it is convenient to use the logarithmic scale, with the help of which parameters  $a$  and  $b$  may be obtained from the least square method. Fig. 3.6 shows the structure functions for different numbers of the Zernike polynomials at the logarithmic scale. It is seen that at large distances (of the order of grid size) numerical solution is in good agreement with analytical for any number of the Zernike polynomials, while at small distances the satisfactory agreement may be obtained only by increasing the number of polynomials. This fact is also confirmed by estimating the parameters  $a$  and  $b$  for different number of polynomials. For two Zernike polynomials  $b=2.0$  and  $a=0.04 \pm 1$ , while for one hundred and four Zernike polynomials  $b=1.78 \pm 0.02$  and  $a=0.04 \pm 0.01$ . However, it should be noticed that even large number of polynomials does not allow to obtain exact power dependence for the structure function.

Similar results may be obtained for the von Karman model of atmospheric turbulence (3.5), the structure function for which is defined by Eq.(3.16). Let the outer scale of turbulence be  $L_0=2 \text{ m}$ , the grid size  $A_x = A_y = A = 5.44 \text{ cm}$ ,  $C_a^2 = 10^{-15} \text{ cm}^{-2/3}$ ,  $\lambda = 0.53 \mu\text{m}$ ,  $\Delta z = 1.2 \text{ km}$ ,  $N_x = N_y = 128$ . The structure functions obtained from Monte Carlo simulations ( $M=300$  phase screens) for these parameters are shown in Fig. 3.7. For comparison the Fig. 3.7 shows the structure function of phase fluctuations on the screen generated using the FFT-based method. It is clearly demonstrated that the Zernike polynomial expansion with the large number of polynomials gives better reproduction of the von Karman phase fluctuations than the FFT-based method.

It may be more emphatically illustrated at the logarithmic scale (Fig.3.8), that numerical solutions are in good agreement with analytical solutions for different number of polynomials if the distance  $r$  is of the order

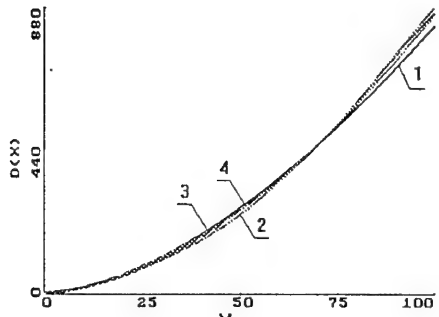


Fig. 3.3

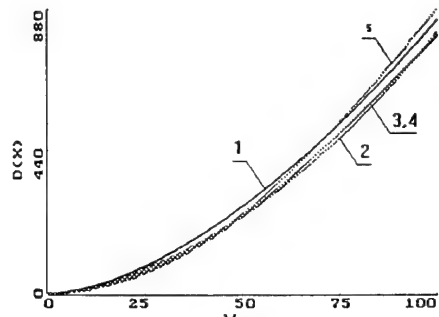


Fig. 3.4

Fig. 3.3. Sections of the structure function of phase fluctuations obtained for  $J = 104$  Zernike polynomials and  $M = 300$  phase screens. Curves: 1- analytical expression for Kolmogorov model, 2 - statistical processing: 2 - along the x-axis, 3 - along the y-axis, 4 - along the chord  $y = R_0 / 3$ .  $C_n^2 = 5 \cdot 10^{-16} \text{ cm}^{-2/3}$ ,  $\lambda = 1.06 \mu\text{m}$ ,  $\Delta z = 7.4 \text{ km}$ .

Fig. 3.4. Examples of the structure functions for different  $J$ . Curves: 1- analytical expression for Kolmogorov model, 2-5 - statistical processing ( $M = 300$ ): 2 -  $J = 5$ , 3 -  $J = 14$ , 4 -  $J = 44$ , 5 -  $J = 104$ . Atmospheric conditions are the same as in Fig. 3.3.

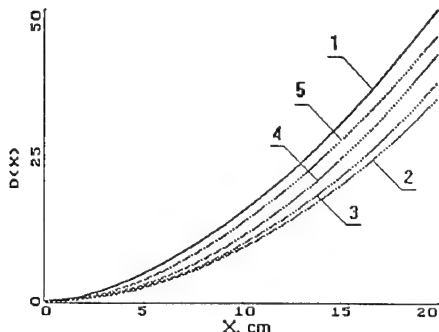


Fig. 3.5

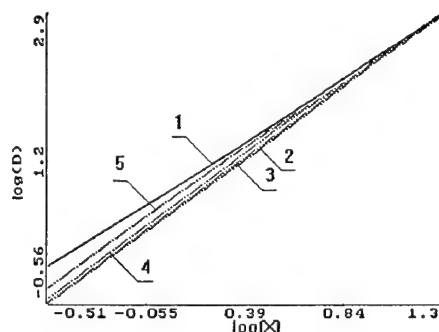


Fig. 3.6

Fig. 3.5. The structure functions at distances  $r \ll A$  for different  $J$ . Curves designation and atmospheric conditions are the same as in Fig. 3.4.

Fig. 3.6. The structure functions at the logarithmic scales for different  $J$ . Curves designation and atmospheric conditions are the same as in Fig. 3.4.

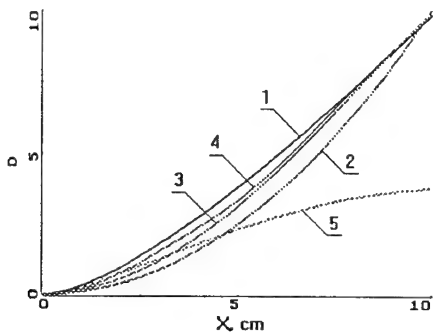


Fig. 3.7

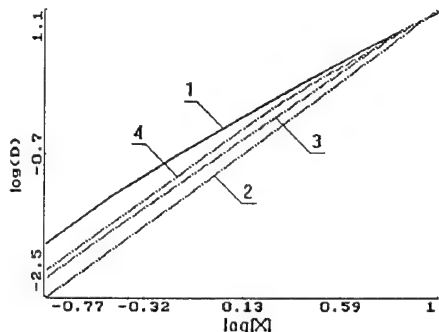


Fig. 3.8

Fig. 3.7. Examples of the structure functions for von Karman model of turbulence. Curves: 1- analytical expression for von Karman model, 2-5 - statistical processing ( $M = 300$ ): 2 -  $J = 2$ , 3 -  $J = 14$ , 4 -  $J = 44$ , 5 - FFT based method.  $A = 5.44 \text{ cm}$ ,  $L_0 = 2 \text{ m}$ ,  $C_n^2 = 10^{-15} \text{ cm}^{-2/3}$ ,  $\lambda = 0.53 \mu\text{m}$ ,  $\Delta z = 1.2 \text{ km}$ .

Fig. 3.8. The structure functions for von Karman model at the logarithmic scales. Curves designation and atmospheric conditions are the same as in Fig. 3.7.

of aperture size  $A$ . However, for small distances discrepancies may be observed which indicate that small-scale fluctuations are not reproduced quite adequately.

In spite of all difficulties, the general conclusion can be made that the phase screens obtained from modal method are applicable for the study of laser beam propagation through the turbulent atmosphere. At the same time one should remember that the effect of the small-scale fluctuations on the beam propagation will not be adequately reproduced.

#### 4. Computer simulations of laser beam propagation

In this section we will discuss methodical aspects of numerical integration of the equation (2.1) describing the propagation of coherent light beam through randomly-inhomogeneous medium. First, we will concentrate on spectral method for solving diffraction equation (2.12), (2.14) in the space between two phase screens. Then we will discuss criteria of applicability of the split-step method. Finally, the method is considered for constructing a flexible grid, which allows to follow random wandering of the beam under the conditions of strong turbulence.

##### 4.1. Spectral method

Spectral method based on the fast Fourier transform algorithm is currently one of the most widespread approaches to the problems of quasi optics. This comparatively simple and effective method has been intensively discussed in the literature<sup>26,43,44</sup>. Nonetheless, there exists a set of methodical questions, which so far have been left aside. The objective of this subsection is to clarify some of them.

Let us seek for the solution to the problem (2.12), (2.14) on the square aperture of the size  $A_0$ . We expand a complex amplitude of the light field  $E(x, y, z)$  in Fourier series over the square  $-A_0/2 \leq x \leq A_0/2$ ,  $-A_0/2 \leq y \leq A_0/2$ :

$$E_d(x, y, z) = \sum_{p=-N/2+1}^{N/2} \sum_{q=-N/2+1}^{N/2} \hat{E}_{pq}(z) \exp\left[\frac{2\pi i}{A_0}(px + qy)\right] \quad (4.1)$$

When writing expansion (4.1) we assume that the function  $E(x, y, z)$  has been replaced by a periodic function with a period  $A_0$ . Suppose that Fourier image of the function  $E$  is either limited or rapidly decreases so that the sum of the first  $N$  harmonics reproduces  $E(x, y, z)$  with necessary accuracy.

Substituting (4.1) into (2.12) or (2.14) we have:

$$\sum_p \sum_q \left[ 2ik \frac{\partial \hat{E}_{pq}}{\partial z} + \left( \frac{2\pi}{A_0} \right)^2 (p^2 + q^2) \hat{E}_{pq} \right] \exp\left[\frac{2\pi i}{A_0}(px + qy)\right] = 0 \quad (4.2)$$

From this it follows that separate harmonics  $\hat{E}_{pq}$  must satisfy the equations:

$$\frac{\partial \hat{E}_{pq}}{\partial z} = -\frac{i}{2k} \left( \frac{2\pi}{A_0} \right)^2 (p^2 + q^2) \hat{E}_{pq}, \quad (4.3)$$

$$-N/2+1 \leq p \leq N/2, -N/2+1 \leq q \leq N/2.$$

The solution to the system (4.3) has the form:

$$\hat{E}_{pq}(z_{s+1/2}) = \hat{E}_{pq}(z_{s-1/2}) \exp\left[\frac{i}{2k} \left( \frac{2\pi}{A_0} \right)^2 (p^2 + q^2) \Delta z\right] \quad (4.4)$$

$$-N/2+1 \leq p \leq N/2, -N/2+1 \leq q \leq N/2.$$

For the first and the last slabs (i.e. for  $s=0$  and  $s=S$ ), the step  $\Delta z$  should be replaced by the step  $\Delta z/2$ .

We now introduce a two-dimensional grid  $x_m = m\Delta x$ ,  $y_m = n\Delta x$ , where  $\Delta x = A_0/N$ ,  $0 \leq m \leq N-1$ ,  $0 \leq n \leq N-1$ . Then the values of Fourier harmonics  $\hat{E}_{pq}(z_{s-1/2})$  may be computed from the values of the complex amplitude  $E_d(x_m, y_m, z_{s-1/2})$ . Numerically this can be done using the FFT:

$$\hat{E}_{pq}(z_{s-1/2}) = \frac{1}{N^2} \sum_{m=0}^{N-1} \sum_{n=0}^{N-1} E_d(x_m, y_n, z_{s-1/2}) \exp\left[-\frac{2\pi i}{N}(pm + qn)\right] \quad (4.5)$$

Thus, knowing the field amplitude at  $z = z_{s-1/2}$ , we may find initial values of Fourier harmonics. The next step is to compute the values of harmonics at  $z = z_{s+1/2}$  from equation (4.4). The final step is to find the complex amplitude at a distance  $z = z_{s+1/2}$  using the inverse Fourier transform:

$$E_d(x_m, y_n, z_{s+1/2}) = \sum_{p=-N/2+1}^{N/2} \sum_{q=-N/2+1}^{N/2} \hat{E}_{pq}(z_{s+1/2}) \exp\left[\frac{2\pi i}{N}(pm + qn)\right] \quad (4.6)$$

In practice one should remember that the most standard subroutines, computing the FFT, use the harmonic ordering from 0 to  $N-1$ . Since harmonics of the complex function are periodic, i.e.

$$\hat{E}_{N-p,q} = \hat{E}_{-p,q}, \quad \hat{E}_{p,N-q} = \hat{E}_{p,-q}, \quad (4.7)$$

we may easily rewrite equations (4.4) so that they are applicable to the calculations with the new harmonic ordering from 0 to  $N-1$ :

$$\begin{aligned} \hat{E}_{p,q}(z_{s+1/2}) &= \hat{E}_{p,q}(z_{s-1/2}) \exp\left[\frac{i}{2k}\left(\frac{2\pi}{A_0}\right)^2 (p^2 + q^2) \Delta z\right] \text{ for } 0 \leq p \leq N/2, 0 \leq q \leq N/2; \\ \hat{E}_{p,q}(z_{s+1/2}) &= \hat{E}_{p,q}(z_{s-1/2}) \exp\left[\frac{i}{2k}\left(\frac{2\pi}{A_0}\right)^2 ((N-p)^2 + q^2) \Delta z\right] \text{ for } N/2 < p \leq N-1, 0 \leq q \leq N/2; \\ \hat{E}_{p,q}(z_{s+1/2}) &= \hat{E}_{p,q}(z_{s-1/2}) \exp\left[\frac{i}{2k}\left(\frac{2\pi}{A_0}\right)^2 (p^2 + (N-q)^2) \Delta z\right] \text{ for } 0 \leq p \leq N/2, N/2 < q \leq N-1; \\ \hat{E}_{p,q}(z_{s+1/2}) &= \hat{E}_{p,q}(z_{s-1/2}) \exp\left[\frac{i}{2k}\left(\frac{2\pi}{A_0}\right)^2 ((N-p)^2 + (N-q)^2) \Delta z\right] \text{ for } N/2 \leq p \leq N-1, N/2 \leq q \leq N-1. \end{aligned} \quad (4.8)$$

The advantages of the presented algorithm are high speed and the lack of such typical for finite-difference schemes side effects as grid dispersion and diffusion. Numerical solution to the diffraction equation is exact for

practical purposes if the function  $E$  is infinitely small at the boundaries of the square aperture  $|x| \leq A_0/2$ ,

$|y| \leq A_0/2$  and its spectrum  $\hat{E}_{pq}$  is infinitely small for  $|p| = N/2$ ,  $|q| = N/2$ . When the first condition is violated, interference between initial beam and its periodic continuation occurs. This obviously leads to the distortion of the beam profile. The violation of the second condition causes spatial frequency aliasing, which in turn leads to the errors in computations of the derivatives  $\partial E / \partial x^2$  and  $\partial E / \partial y^2$  in spectral domain. Thus, in order to control the accuracy during the calculations, one should regularly estimate the values of the function

$|E|^2$  at the edges of the grid as well as the values of its spectrum  $|\hat{E}_{pq}|^2$  at Nyquist frequency.

#### 4.2. Criteria of the split-step method applicability

Numerical analysis of the light field propagation in the atmosphere is based on the discretization of independent variables  $x, y, z$  and representation of the amplitude and phase of the field by their values at the discrete set of points. Over the past decade the question, whether this discrete model adequately describes the propagation of a light field in randomly-inhomogeneous medium or not, has been discussed in a lot of papers, a review of which has been done by Knepp<sup>43</sup>. He formulates the following problems, which have to be taken into account when choosing the number of grid points and step size: - accuracy of phase reproduction on the screen; - accuracy of the solution to the wave propagation equation; - minimization of boundary effects.

Let us discuss these questions in more details, adding our own experience to the ideas, developed in Ref. 43.

#### 4.2.1. Phase reproduction

The choice of the phase screen size and grid step for the adequate reproduction of phase fluctuations ranging between the inner and the outer scales of turbulence, has been thoroughly discussed in section 3. Here we only note one important condition: phase difference between the neighboring grid points must not exceed the value of  $\pi$ , i.e.

$$\max_{m,n} [(\varphi_{m+1,n} - \varphi_{m,n}), (\varphi_{m,n+1} - \varphi_{m,n})] < \pi \quad (4.9)$$

For the grid step  $\Delta x$  this condition may be rewritten in the form:

$$\Delta x \max_{x,y} \left| \frac{\partial \varphi}{\partial x} \right| < \pi, \quad \Delta x \max_{x,y} \left| \frac{\partial \varphi}{\partial y} \right| < \pi \quad (4.10)$$

When generating the phase screen using the spectral method, random field  $\varphi(x, y)$  is represented as a superposition of Fourier harmonics with random amplitudes, the root-mean-square values of which are:

$$a_{pq} = \frac{1}{N} \sqrt{F_\varphi(\kappa_{pq})} \frac{2\pi}{A_0},$$

where  $F_\varphi(\kappa)$  is the spectrum of phase fluctuations on the screen,  $\kappa_{pq} = \sqrt{\kappa_p^2 + \kappa_q^2}$ . Consequently, for the harmonic with indices  $pq$

$$\max_x \left| \frac{\partial \varphi_{pq}}{\partial x} \right| = a_{pq} \kappa_{pq} = \kappa_{pq} \sqrt{F_\varphi(\kappa_{pq})} \frac{2\pi}{A_0 N} \quad (4.11)$$

and the condition (4.10) takes the form:

$$\Delta x < \frac{A_0 N}{2} \left[ \max_{pq} (\kappa_{pq} \sqrt{F_\varphi(\kappa_{pq})}) \right]^{-1}. \quad (4.12)$$

For the definiteness, we will use the modified von Karman model to make some estimates. For this model the maximum of the expression  $\kappa \sqrt{F_\varphi(\kappa)}$  occurs at  $\kappa_0 = 2\pi/L_0$ , where  $L_0$  is the outer scale of turbulence. Taking into account Eqs.(2.8) and (3.6) we finally obtain:

$$\Delta x < 3.1 \frac{A_0}{L_0^{5/12} \sqrt{k_0 C_n \sqrt{\Delta z}}} \quad (4.13)$$

From this it is clear that the estimate for the grid step  $\Delta x$  depends not only on the grid size  $A_0$  and propagation parameters  $k_0$ ,  $C_n$ ,  $L_0$  but also on the step  $\Delta z$  in the propagation direction. This is associated with the fact that the variance of phase fluctuations on the screen is defined by the length of the modelled turbulent slab. Therefore, additional ways of estimating  $\Delta z$  should be found.

#### 4.2.2. Light wave propagation

Since in the space between the screens light wave experiences natural diffraction, the discretization of  $z$ -variable most likely will not introduce essential error into the simulations, if  $\Delta z$  does not exceed the diffraction length for the smallest inhomogeneity, reproduced on the screen. Since the size of this inhomogeneity is of the order of the grid step, a reliable estimate for  $\Delta z$  has the form:

$$\Delta z < k_0 \Delta x^2. \quad (4.14)$$

Note, that this limitation is significantly stronger than that formulated in Ref. 43:

$$\Delta z < \frac{k_0}{\pi} A_0 \Delta x \quad (4.15)$$

Substituting estimate for  $\Delta z$  from (4.14) into (4.13), we have

$$\Delta x < 2.1 A_0^{2/3} L_0^{5/18} k_0^{-1/2} C_n^{-1/3}. \quad (4.16)$$

For typical parameters of simulations ( $A_0=1$  m,  $L_0=0.5$  m,  $k_0=5.93 \cdot 10^6$  m $^{-1}$ ) we obtain that  $\Delta x$  must not exceed several millimeteres in the case of strong turbulence ( $C_a^2 = 10^{-13}$  cm $^{-2/3}$ ) and several centimeters in the case of weak turbulence ( $C_a^2 = 10^{-17}$  cm $^{-2/3}$ ). The number of grid points N must be from several hundreds to several tens.

Another estimate for  $\Delta x$  may be obtained when simulating the propagation of the focused beams, the wave front of which at  $z=0$  is given by:

$$\varphi(x, y) = k_0 \frac{x^2 + y^2}{2R_f}, \quad (4.17)$$

where  $R_f$  is a focal length of a lens. Taking into account the condition (4.9), we have:

$$\Delta x < \frac{2\pi}{k_0} \frac{R_f}{A_0} = \lambda \frac{R_f}{A_0}. \quad (4.18)$$

This condition may be optimized if we replace  $A_0$  by the effective size of the region of localization of the beam on the transmitter. For Gaussian beam this size is of the order of  $10a_0$ .

#### 4.2.3. Boundary effects

Numerical integration of the equation (2.1), which describes the propagation in free space, is performed on the grid of a finite size  $A_0$ . To make sure that numerical solution is valid, one should control the beam energy conservation. This becomes crucial when the beam travels large distances comparable with a diffraction length  $z_d = ka_0^2$ . The most reliable estimate of the numerical solution validity is the analysis of the beam spatial spectrum while the beam propagates through the phase screens. However, priori estimates of the  $\Delta z$  step are also quite useful.

Since the angle  $\vartheta$  of the wave scattering and phase  $\varphi$  are related by the equation

$$\vartheta = \sqrt{\vartheta_x^2 + \vartheta_y^2}, \quad \vartheta_x = \frac{1}{k_0} \frac{\partial \varphi}{\partial x}, \quad \vartheta_y = \frac{1}{k_0} \frac{\partial \varphi}{\partial y}, \quad (4.19)$$

the energy of the wave, which travels a distance  $\Delta z$  in the direction of propagation, travels in the perpendicular direction a distance  $\vartheta \Delta z$ . In order to neglect the boundary effects, one should choose the grid size  $A_0$  not less than  $2\vartheta_{\max}\Delta z$ . Using the estimate (4.11) for  $\vartheta_{\max}$  and assuming the modified von Karman model of turbulence we have:

$$\Delta z \leq 1.33 A_0^2 L_0^{5/9} (C_a \Delta x)^{-2/3}. \quad (4.20)$$

It should be noted, that the above estimate is valid only for the model of turbulence with limited outer scale. When generating the phase screens using the spectral method, the actual outer scale reproducible on the grid does not exceed  $A_0$ . Beam wander and blur are not significant. In this case boundary effects are negligibly small even when  $\Delta z$  is comparatively large. This fact is supported by the Eq.(4.20), when substituting into it typical parameters of simulations. The modal approach allows to use the models with unlimited outer scale (e.g. the Kolmogorov and Tatarskii models). In this case estimate (4.20) is not valid and analytical dependences for the root-mean-square shift of the beam and effective radius should be used to obtain the grid size  $A_0$  and step  $\Delta z$  (see section 5).

#### 4.2.4. Practical estimates of the split-step method convergence

In this subsection we perform the numerical analysis of the split-step method convergence. For simplicity, we consider a one-dimensional beam with complex amplitude  $E = E(x, z)$ , the propagation equation for which has the form:

$$2ik_0 \frac{\partial E}{\partial z} = \frac{\partial^2 E}{\partial x^2} + 2k_0^2 \tilde{n}(x, z)E. \quad (4.21)$$

The spectrum of phase fluctuations on a one-dimensional phase screen may be obtained by integrating (3.6) over  $\kappa_y$  and has the form:

$$F_\phi(\kappa) = 0.111\pi k_0^2 \Delta z C_a^2 (\kappa^2 + \kappa_0^2)^{-4/3} \exp(-\kappa^2 / \kappa_m^2) \quad (4.22)$$

where  $\kappa_0$  and  $\kappa_m$  have been defined previously. For the simulations we choose the following parameters:

$a_0 = 5\text{cm}$ ,  $\lambda = 1.06\mu\text{m}$ ,  $A_0 = 409.6\text{cm}$ ,  $L_0 = 102.4\text{cm}$ ,  $I_0 = 5\text{mm}$ ,  $N = 2048$ ,  $\Delta x = 2\text{m}$ ,  $C_a^2 = 10^{-15}\text{cm}^{-2/3}$ . Beam diffraction length is  $z_d = 14.82\text{ km}$ , diffraction length for the smallest scale of amplitude fluctuations is  $\kappa_0 \Delta x^2 = 23.7\text{ m}$ .

From Monte Carlo simulations we obtain the following statistical quantities describing the beam propagation:

the root-mean-square displacement of the beam centroid

$$x_c = \langle \tilde{x}_c^2 \rangle^{1/2}, \quad \tilde{x}_c = \int x I(x, z) dx / \int I(x, z) dx, \quad (4.23)$$

long exposure effective beam radius

$$a_{\text{eff}} = \left\{ \int x^2 < I(x, z) > dx / \int I(x, z) dx \right\}^{1/2}; \quad (4.24)$$

coherence function

$$\gamma(x) = \left| \langle E(-x/2) E^*(x/2) \rangle \right| / [ < I(-x/2) > < I(x/2) > ]^{1/2}; \quad (4.25)$$

and the radius of coherence  $\rho_E$  defined at  $\sigma^1$  level of  $\gamma(x)$ ;

the irradiance covariance fluctuations

$$b_I(x) = \langle (I(-x/2) - < I(-x/2) >) (I(x/2) - < I(x/2) >) \rangle / [\sigma_I^2(-x/2) \sigma_I^2(x/2)]^{1/2}, \quad (4.26)$$

where  $\sigma_I^2 = < I^2 > - < I >^2$  - is the irradiance variance;

radius of irradiance covariance  $\rho_I$  defined at  $\sigma^1$  level of  $b_I(x)$ ;

the log-amplitude variance of at the beam center

$$\sigma_x^2(0) = < \log^2(E(0)/E_0(0)) > - < \log(E(0)/E_0(0)) >^2, \quad (4.27)$$

where  $E_0 = E_0(x, z)$  is the field of the unperturbed beam propagating in vacuum;

the scintillation index (normalized irradiance variance) at the beam center

$$\beta_I^2 = < I^2(0) > / < I(0) >^2 - 1. \quad (4.28)$$

All statistical quantities have been defined by averaging over  $M=100$  realizations.

Figures 4.1-4.3 show the dependences of the defined quantities on the number of phase screens  $S$  in the strong fluctuation regime: the length of the path  $z=5\text{ km}$  ( $=0.3374 z_d$ ), the Rytov variance at the end of the path  $\beta_0^2=12.77$ . From the figures it is clear that the energy characteristics  $x_c$  and  $a_{\text{eff}}$  have a weak dependence on the number of screens and converge rapidly with increasing  $S$ . Note a rapid growth of the light field fluctuations at  $S=32$ , when the distance between the screens is comparable with the diffraction length for the inner scale of turbulence. A reliable convergence of the results reveals for  $S \geq 256$ , i.e. in the case, when  $\Delta z$  becomes less than diffraction length, defined from the grid step ( $\Delta z < k_0 \Delta x^2$ ). The simulation results, given in the weak fluctuation regime ( $z=625\text{ m}$  ( $=0.042 z_d$ ),  $\beta_0^2=0.28$ ), confirm this conclusion (see Figs. 4.4-4.6). For this case the condition  $\Delta z = k_0^2$  yields  $S=4$ , while the condition  $\Delta z = k \Delta x^2$  yields  $S=32$ . Thus the most reliable estimate for the distance between the screens is inequality (4.14).

#### 4.3 Flexible grid

In the strong fluctuation regime, when the Kolmogorov spectral density is chosen, random wander of the beam in separate realizations may several times exceed its initial radius. So in the simulations we have to use buffer zones in order to minimize boundary effects on the grid. This results in the increasing grid step and decreasing accuracy of computations, if the array size remains unchanged.

In this subsection we suggest a simple trick, that allows to retain the high resolution of the grid in the strong fluctuation regime without the increasing the number of grid points. The trick is based on the introduction of flexible grid, which moves with the wandering beam. Below we will discuss two ways of handling the problem.

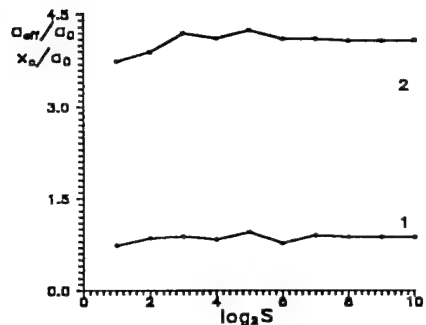


Fig. 4.1

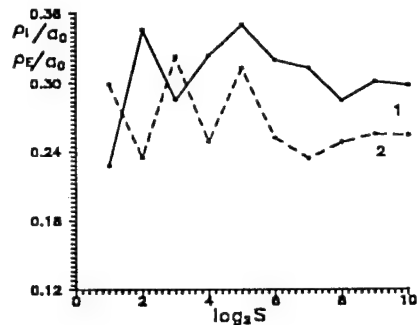


Fig. 4.2

Fig. 4.1. Convergence of  $\rho_c$  (curve 1) and  $a_{\text{eff}}$  (curve 2) as a number of phase screens  $S$  increases.  
 $z=5\text{km}, \beta_0^2=12.77$

Fig. 4.2. Convergence of  $\rho_E$  (curve 1) and  $\rho_I$  (curve 2) as a number of phase screens  $S$  increases.  
 $z=5\text{km}, \beta_0^2=12.77$

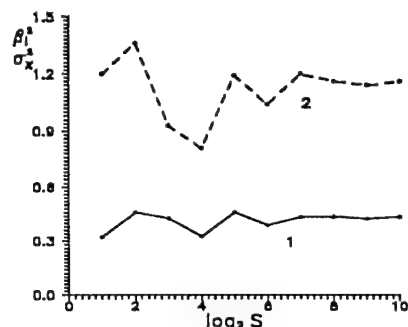


Fig. 4.3

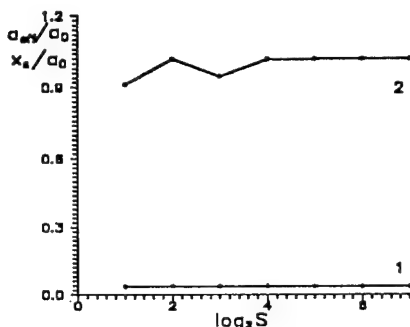


Fig. 4.4

Fig. 4.3. Convergence of  $\sigma_x^2$  (curve 1) and  $\beta_I^2$  (curve 2) as a number of phase screens  $S$  increases.  
 $z=5\text{km}, \beta_0^2=12.77$

Fig. 4.4. Convergence of  $\rho_c$  (curve 1) and  $a_{\text{eff}}$  (curve 2) as a number of phase screens  $S$  increases.  
 $z=625\text{m}, \beta_0^2=0.28$

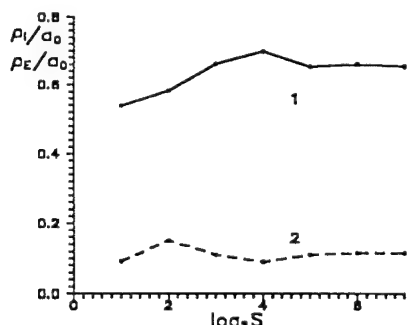


Fig. 4.5

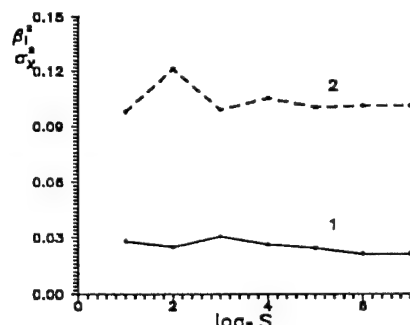


Fig. 4.6

Fig. 4.5. Convergence of  $\rho_E$  (curve 1) and  $\rho_I$  (curve 2) as a number of phase screens  $S$  increases.  
 $z=625\text{m}, \beta_0^2=0.28$

Fig. 4.6. Convergence of  $\sigma_x^2$  (curve 1) and  $\beta_I^2$  (curve 2) as a number of phase screens  $S$  increases.  
 $z=625\text{m}, \beta_0^2=0.28$

The first way is to predict the movement of the beam on the basis of its wave front analysis. Let after the passage of the  $S$ th phase screen, the wavefront of the beam be  $U_s(x, y)$ . Applying the least square method it is easy to find the tilt angles  $(\vartheta_x)_s$  and  $(\vartheta_y)_s$  along the axis  $x$  and  $y$  respectively:

$$(\vartheta_x)_s = \frac{1}{k_0} \sum_{m,n=1}^N x_m U_{m,n} / N \sum_{m=1}^N x_m^2, \quad (\vartheta_y)_s = \frac{1}{k_0} \sum_{m,n=1}^N y_m U_{m,n} / N \sum_{m=1}^N y_m^2 \quad (4.29)$$

If the beam propagated at angles  $(\vartheta_x)_s$  and  $(\vartheta_y)_s$  to the initial optical axis, its center in the  $(S+1)$ th screen would displace by a distance

$$(\tilde{x}_c)_{s+1} = (\vartheta_x)_s \Delta z, \quad (\tilde{y}_c)_{s+1} = (\vartheta_y)_s \Delta z \quad (4.30)$$

from its position in the  $S$ th screen. If we transform the wave front  $U_s(x, y)$  by removing the tilts

$$\bar{U}_s(x, y) = U_s(x, y) - k_0 (\vartheta_x)_s x - k_0 (\vartheta_y)_s y, \quad (4.31)$$

the beam will propagate along its initial optical axis. Repeating this procedure at each step and remembering the calculated values of the displacements  $(\tilde{x}_c)_s$ ,  $(\tilde{y}_c)_s$ , we obtain practically straight-line propagation of the beam. The algebraic sum of the values  $(\tilde{x}_c)_s$  and  $(\tilde{y}_c)_s$  will give us the displacement of the beam center at the end of the path. The grid size may be significantly decreased by reducing the buffer zones.

The second way is to decrease the effect of accumulation of the displacement, when the beam propagates in the medium. At each phase screen we calculate the coordinates of the beam centroid  $(\tilde{x}_c)_s$  and  $(\tilde{y}_c)_s$ . Then the beam center is shifted to the origin of the coordinates by cyclic reassigning of elements of complex array  $(E_{mn})_s$ . As in the first case, the shift of the center at the end of the propagation path can be obtained from the sum of the displacements  $(\tilde{x}_c)_s$ ,  $(\tilde{y}_c)_s$ .

In our practice the application of both methods in the strong fluctuation regime showed high efficiency.

## 5. The effect of large-scale refractive index fluctuations on the propagation of the beam through the turbulent atmosphere

As it was mentioned before, atmospheric turbulence has a broad spatial spectrum of the refractive index fluctuations, which cannot be completely reproduced on a grid of reasonable size. At the same time this spectrum rapidly drops with increasing spatial frequency. Therefore the low-order aberrations dominate in the wave front of the light wave. This has been clearly demonstrated in Ref. 45, where experimentally measured wave fronts of the laser beam, propagating in the planetary boundary layer are presented.

Here we employ the idea of separate simulations of the large- and small-scale fluctuations of the refractive index. This approach enables us to analyze the contribution of the different parts of atmospheric spectra on statistics of the light beam. It is naturally to assume, that random wander and blur of the beam as a whole, which are revealed in the irradiance profile during the long-exposure registration, are to a great extent caused by a low-frequency part of the spectrum.

This section describes numerical simulations of these effects using the modal representation of the refractive index fluctuations. The parameters of numerical algorithm are optimized on the basis of comparison of Monte Carlo simulations results with the theoretical predictions. Various atmospheric spectra and fluctuation regimes are considered and the influence of the outer scales on the energy characteristics of the light beam is discussed.

### 5.1 Optimization of the phase screen model

In the modal representation of atmospheric inhomogeneities the diameter of the circle  $D$ , over which Zernike polynomial expansion of a random phase is performed, is a free parameter. At the same time diameter

D defines the variances of random Zernike coefficients, and consequently the value of D significantly effects on the phase fluctuations variance  $\sigma_\phi^2$  on the screen. It is naturally to expect that in the limit, when the number of the Zernike modes tends to infinity, the dependence of  $\sigma_\phi^2$  on D will be decreasing. Most likely, the ideal phase screen, which is reproduced by a sum of infinite number of the Zernike modes, has to adequately reproduce the wave front at any D. However, in simulations the number of the Zernike modes is always limited and in the most cases not too large. Therefore, it is of practical interest to estimate the diameter of the circle and the number of the Zernike polynomials, for which such effects like random blur and wander of the beam, are reproduced satisfactorily.

As a base for the estimates, let us use theoretical predictions, developed in<sup>46</sup> for the effective beam parameters in the atmosphere<sup>47</sup>. In particular, for the Kolmogorov spectral density, theory<sup>46</sup> gives the following formula for the effective beam radius  $a_{\text{eff}}$ , which defines the dimensions of the area painted by beam wander

$$a_{\text{eff}} = a_d \{1 + 1.624(\beta_0^2)^{6/5} z / (k_0 a_d^2)\}^{1/2}, \quad (5.1)$$

where

$$a_d(z) = a_0 \left\{ \left( \frac{z}{k_0 a_0} \right)^2 + \left( 1 - \frac{z}{R_f} \right)^2 \right\}^{1/2} \quad (5.2)$$

is the radius of diffraction-limited Gaussian beam in vacuum,  $a_0$  is the initial beam radius,

$$\beta_0^2 = 1.23 C_a^2 k_0^{7/6} z^{1/6} \quad (5.3)$$

is the Rytov variance. In simulations we obtained the following statistical quantities:  
root-mean-square displacement of the beam centroid

$$\rho_c = \langle \tilde{\rho}_c \rangle, \quad \tilde{\rho}_c = \sqrt{\tilde{x}_c^2 + \tilde{y}_c^2}, \quad x_c = \iint x I dx dy / \iint I dx dy, \quad y_c = \iint y I dx dy / \iint I dx dy \quad (5.4)$$

effective beam radius

$$a_{\text{eff}} = \left\{ \iint (x^2 + y^2) \langle I \rangle dx dy / \iint I dx dy \right\}^{1/2}. \quad (5.5)$$

We performed the averaging over M=100 realizations for the beam with the following parameters:  $a_0=5$  cm,  $\lambda=1.06 \mu\text{m}$  (diffraction length  $z_d=14.82$  km). The grid size was  $A_0=100$  cm with 128 points in both x- and y-directions. The number of phase screens was varied from S=10 to S=20, the length of the path was  $z=7.41$  km ( $=0.5 z_d$ ). We used the Kolmogorov model of turbulence.

### 5.1.1. The collimated beam

When simulating the phase screens, we start for simplicity from 5 Zernike polynomials, describing the aberrations of the first and the second order (the piston mode is excluded from the consideration). Fig. 5.1 shows the dependences of  $a_{\text{eff}}$  on z, obtained for different ratios  $D/a_0$  in the case of moderate fluctuation regime ( $C_a^2 = 5 \cdot 10^{-17} \text{ cm}^{-2/3}$ ,  $\beta_0^2=1.31$ ). The best agreement between the simulation results and theoretical prediction (5.1) is observed for  $D/a_0=2.5$ . With increasing D the effective radius decreases due to the decrease in the variances of the Zernike modes, proportional to  $D^{6/5}$ . Fig. 5.2 shows the same dependences obtained for  $D/a_0=2.5$  in the cases of weak ( $\beta_0^2=0.26$ ), moderate ( $\beta_0^2=1.31$ ) and strong ( $\beta_0^2=13.1$ ) fluctuation regimes.

It is of interest to try to improve the agreement between the simulation results and theoretical predictions by increasing the number of the Zernike polynomials J. We take J=14 for the modes up to the 4th order and J=44 for the modes up to the 6th order. The calculated dependences  $a_{\text{eff}}(z)$ , obtained for the different number of the Zernike modes are shown in Fig. 5.3 ( $\beta_0^2=1.31$ ,  $D/a_0=4$ ) and in Fig. 5.4 ( $\beta_0^2=13.1$ ,  $D/a_0=8$ ). From these figures it is clear that increasing the number of the Zernike modes gives the more pronounced effect in the case of moderate fluctuations and less pronounced in the case of strong fluctuations. Note, that the optimum size of the diameter D increases with increasing number of the Zernike polynomials from  $D/a_0=2.5$  for J=5 to  $D/a_0=8$  for J=44.

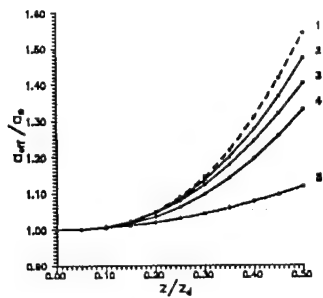


Fig.5.1.

Fig.5.1. Dependencies of  $a_{eff}$  on  $Z$  for collimated beam. Curves: 1 - theory, 2-4 - Monte Carlo method at different values of  $D/a_0$ : 2 -  $D/a_0=2.5$ ; 3 -  $D/a_0=4$ ; 4 -  $D/a_0=10$ ; 5 - vacuum. Turbulence is reproduced by  $J=5$  Zernike modes. Propagation conditions are:  $a_0 = 5\text{cm}$ ,  $\lambda = 1.06\mu\text{m}$ ,  $C_n^2 = 5 \cdot 10^{-17} \text{cm}^{-2/3}$ ,  $\beta_0^2 = 1.31$ .

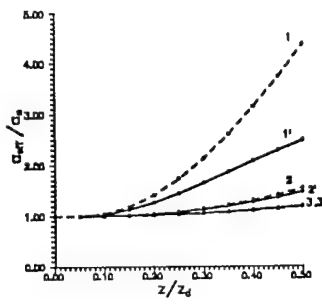


Fig.5.2.

Fig.5.2. Dependencies of  $a_{eff}$  on  $Z$  for collimated beam. Curves: 1,2,3 - theory, 1',2',3' - Monte Carlo method ( $C_n^2 = 5 \cdot 10^{-16}, 5 \cdot 10^{-17}, 10^{-17} \text{cm}^{-2/3}$ , respectively). Phase screen parameters:  $J=5$ ,  $D/a_0=2.5$ . Beam parameters:  $a_0 = 5\text{cm}$ ,  $\lambda = 1.06\mu\text{m}$ .

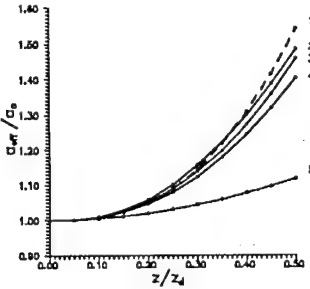


Fig.5.3.

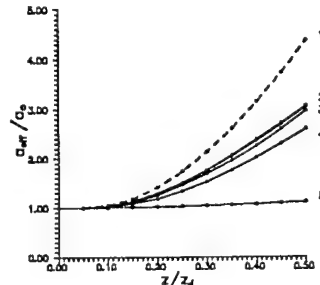


Fig.5.4.

Fig.5.3. Dependencies of  $a_{eff}$  on  $Z$  for collimated beam. Curves: 1 - theory, 2-4 - Monte Carlo method at different number of Zernike modes: 2 -  $J=44$ ; 3 -  $J=14$ ; 4 -  $J=5$ ; 5 - vacuum. Phase screen parameter  $D/a_0=4$ . Propagation conditions are:  $a_0 = 5\text{cm}$ ,  $\lambda = 1.06\mu\text{m}$ ,  $C_n^2 = 5 \cdot 10^{-17} \text{cm}^{-2/3}$ ,  $\beta_0^2 = 1.31$ .

Fig.5.4. Dependencies of  $a_{eff}$  on  $Z$  for collimated beam. Curves designation is the same as in Fig. 5.3. Phase screen parameter  $D/a_0=8$ . Propagation conditions are:  $a_0 = 5\text{cm}$ ,  $\lambda = 1.06\mu\text{m}$ ,  $C_n^2 = 5 \cdot 10^{-16} \text{cm}^{-2/3}$ ,  $\beta_0^2 = 1.31$ .

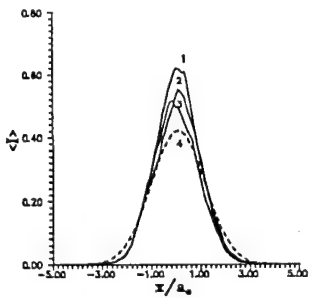


Fig.5.5.

Fig.5.5. Mean irradiance profiles obtained by Monte-Carlo method: 1 -  $J=5$ ; 2 -  $J=14$ ; 3 -  $J=44$  ( $D/a_0=4$ ). Curve 4 - Gaussian profile with theoretically predicted  $a_{eff}$ .

Fig.5.6. Logarithmic representation of mean irradiance profiles shown in Fig.5.5.

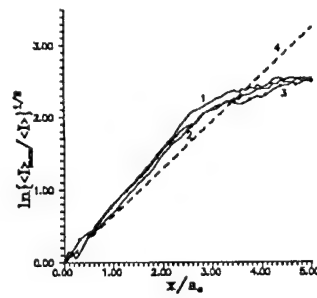


Fig.5.6.

Drastic discrepancies between numerically obtained and theoretically predicted results in the regime of strong fluctuations (Fig. 5.4) may not be explained by the limited number of the polynomials: the increase in  $J$  from 14 to 44 causes only 2% increase in  $a_{\text{eff}}$ . From our point of view, the theory overestimates the values of  $a_{\text{eff}}$  for the conditions under discussion. Indeed, the results in Ref.46 are obtained under the assumption that the long-exposure mean irradiance profile is Gaussian. Analysis of the mean irradiance profiles obtained in simulations for different  $J$  (Fig. 5.5) demonstrates that in the strong fluctuation regime this assumption might be not valid. This may be clearly demonstrated by the analysis of the Fig.5.6, where the functions  $\ln(\langle I \rangle_{\max} / \langle I(x) \rangle)$  are shown for the mean irradiance profiles from Fig. 5.5. Here  $\langle I \rangle_{\max}$  is the maximum value of the intensity for the given profile. A straight line on the plot corresponds to Gaussian profile with the effective radius obtained from Eq.(5.1). The difference between the slopes of the simulated and theoretically predicted lines is clearly seen. This difference is the most pronounced at the edge of the beam.

Bearing in mind the considerations presented above, it is likely to expect that with increasing fluctuation strength the difference between the simulated and theoretically predicted (5.1) radius of the effective beam will be increasing.

### 5.1.2. Focused beam

When analyzing the propagation of the focused beam, we use the simplified phase screen model, which contains only the first and the second-order Zernike modes ( $J=5$ ). The optimized ratio  $D/a_0$  for this case is equal to 2.5. Let us consider the beam, described in subsubsection 5.1.1, focused at a distance  $R_f=7.41$  km ( $=0.5 z_d$ ). Simulated and theoretical dependences of  $a_{\text{eff}}$  on  $z$  are shown in Fig. 5.7 for those values of  $C_a^2$ , which correspond to  $\beta_0^2=0.26, 1.31, 13.1$ . It is seen that for the focused beam as well as for the collimated beam, numerical and theoretical results quite satisfactorily agree in the weak and moderate fluctuation regimes, while in the strong fluctuation regime the formula (5.1) overestimates  $a_{\text{eff}}$ . At the same time the location of the effective beam waist in turbulence  $z_{be}$ , obtained from the Monte Carlo simulations is in good agreement with that predicted by Eq.(5.1) in wide range of  $C_a^2$  (Fig.5.8). As predicted in Ref.46, turbulent beam waist migrates towards the transmitter as the turbulent strength increases.

### 5.2. The role of the outer scale

The estimate of the influence of the outer scale of turbulence on energy characteristics of the beam was performed for the von Karman spectral density. (3.6). The conditions of the beam propagation are those described in subsection 5.1.

Fig. 5.9 shows the simulated dependences  $a_{\text{eff}}(z)$  obtained for the collimated beam in the moderate fluctuation regime ( $C_a^2 = 5 \cdot 10^{-17} \text{ cm}^{-2/3}$ ) for different values of the outer scale  $L_0$ . For comparison, we again plotted the curves for the Kolmogorov turbulence presented in Fig. 5.1: simulated dependence for  $L_0 = \infty$  and theoretical prediction (5.1). It is clear that with decreasing outer scale the effective beam radius decreases. This decrease is more pronounced for small  $L_0$ . Basically, this behavior of  $a_{\text{eff}}$  can be explained by the decrease in the variance of random migrations of the beam and to a less degree by the decrease in random blur, since the value of the outer scale most significantly affects the tilt variance of the wave front<sup>48,49</sup>.

Results for the focused beam are presented in Figs.5.10, 5.11, where  $R_f=0.5 z_d$ . Fig. 5.10 shows the dependence  $a_{\text{eff}}(z)$  in the weak ( $\beta_0^2=0.26$ ) and moderate ( $\beta_0^2=1.31$ ) fluctuation regimes for both the Kolmogorov and the von Karman (with  $L_0 = 100 a_0 = 5 \text{ m}$ ) models of turbulence. For comparison the curves obtained from Eq.(5.1) are also presented. Fig. 5.11 illustrates the dependence of the location of the effective beam waist  $z_{be}$  on the outer scale. Results were obtained from Monte Carlo simulations in the regimes of weak, moderate and strong fluctuations. With decreasing outer scale, the effective beam waist shifts from the transmitter in all regimes according to the Kolmogorov model.

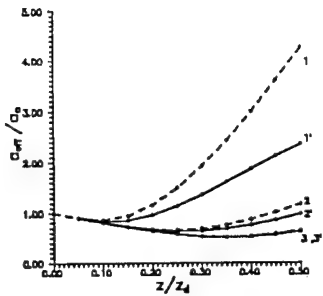


Fig.5.7.

Fig.5.7. Dependencies of  $a_{eff}$  on  $Z$  for convergent beam. Curves: 1,2,3 - theory, 1',2',3' - Monte Carlo method ( $\beta_0^2 = 13.1, 1.31, 0.26$ , respectively). Phase screen parameters:  $J=5$ ,  $D/a_0=2.5$ . Beam parameters:  $a_0 = 5\text{cm}$ ,  $\lambda = 1.06\mu\text{m}$ ,  $R_f = 7.41\text{km} (= 0.5z_d)$ .

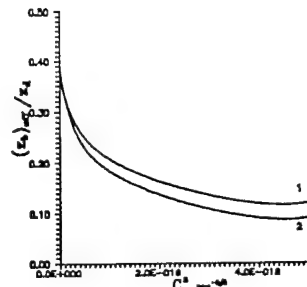


Fig.5.8.

Fig.5.8. Coordinate of effective beam waist in Kolmogorov turbulence as a function of  $C_n^2$ . Curves: 1 - theory, 2 - Monte Carlo method. Phase screen parameters:  $J=5$ ,  $D/a_0=2.5$ . Beam parameters:  $a_0 = 5\text{cm}$ ,  $\lambda = 1.06\mu\text{m}$ ,  $R_f = 7.41\text{km} (= 0.5z_d)$ .

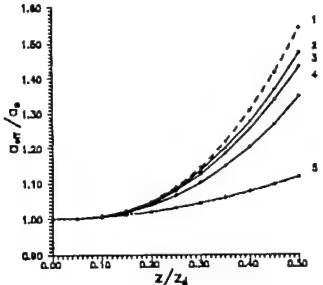


Fig.5.9.

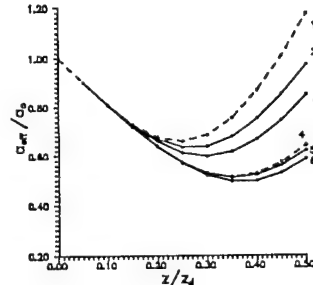


Fig.5.10.

Fig.5.9. Dependencies of  $a_{eff}$  on  $Z$  for collimated beam. Curves: 1,2- theory and Monte Carlo method for  $L_0 = \infty$ , 3,4 - Monte Carlo method for  $L_0 = 5\text{m}$  and  $2\text{m}$  respectively, 5 - vacuum. Propagation conditions are:  $a_0 = 5\text{cm}$ ,  $\lambda = 1.06\mu\text{m}$ ,  $C_n^2 = 5 \cdot 10^{-17} \text{ cm}^{-2/3}$ ,  $\beta_0^2 = 1.31$ .

Fig.5.10. Dependencies of  $a_{eff}$  on  $Z$  for collimated beam. Curves: 1,2- theory and Monte Carlo method for  $L_0 = \infty$ ,  $C_n^2 = 5 \cdot 10^{-17} \text{ cm}^{-2/3}$ , 3 - Monte Carlo method for  $L_0 = 5\text{m}$ ,  $C_n^2 = 5 \cdot 10^{-17} \text{ cm}^{-2/3}$ , 4,5 - theory and Monte Carlo method for  $L_0 = \infty$ ,  $C_n^2 = 10^{-17} \text{ cm}^{-2/3}$ , 6 - Monte Carlo method for  $L_0 = 5\text{m}$ ,  $C_n^2 = 10^{-17} \text{ cm}^{-2/3}$ , 7 - vacuum. Propagation conditions are:  $a_0 = 5\text{cm}$ ,  $\lambda = 1.06\mu\text{m}$ ,  $R_f = 7.41\text{km} (= 0.5z_d)$ .

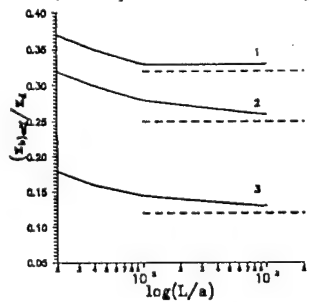


Fig.5.11.

Fig.5.11. Coordinate of effective beam waist in von Karman turbulence as a function of  $L_0$ . Curves: 1 -  $C_n^2 = 10^{-17} \text{ cm}^{-2/3}$ ,  $\beta_0^2 = 0.26$ , 2 -  $C_n^2 = 5 \cdot 10^{-17} \text{ cm}^{-2/3}$ ,  $\beta_0^2 = 1.31$ , 3 -  $C_n^2 = 5 \cdot 10^{-16} \text{ cm}^{-2/3}$ ,  $\beta_0^2 = 13.1$ . Dashed lines - values of  $(z_{eff})_{\infty}$  at  $L_0 = \infty$ . Beam parameters:  $a_0 = 5\text{cm}$ ,  $\lambda = 1.06\mu\text{m}$ ,  $R_f = 7.41\text{km} (= 0.5z_d)$

### 5.3. Random migrations of beam centroid

Monte Carlo method allows to separately investigate various statistical quantities describing the beam propagation. In particular, this method may be used to confirm the results, predicted in Ref.50 for the variance of random migrations of the beam in the turbulent atmosphere. Under the assumption of the disturbed field of Gaussian collimated beam authors of Ref.50 derived the formula for the variance of the beam centroid displacement:

$$\rho_c^2 = \frac{4\pi^2 z^3}{3} \int_0^\infty \kappa^3 \Phi_a(\kappa) e^{-\kappa^2 a_0^2/2} d\kappa, \quad (5.6)$$

where  $\Phi_a$  is the spectrum of the refractive index fluctuations. For the Kolmogorov model of turbulence the integral in (5.6) may be computed analytically. Thus we have

$$\rho_c^2 = \frac{0.132\pi^2 \Gamma(1/6)}{3 \cdot 2^{5/6}} C_n^2 z^3 a_0^{-1/3}. \quad (5.7)$$

For other than Kolmogorov spectral densities, integral in Eq.(5.6) may be easily computed numerically.

The Table 5.1 presents the results of numerical analysis of migration of collimated beam centroid random. The data are compared with those obtained from Eqs.(5.6), (5.7). Good agreement between the theoretical predictions and results of Monte Carlo simulations is demonstrated in the wide range of values of the outer scale and turbulence strength.

**Table 5.1.** RMS beam displacement  $\rho_c / a_0$  as a function of outer scale of turbulence for collimated beam ( $a_0 = 5 \text{ cm}$ ,  $\lambda = 1.06 \mu\text{m}$ ,  $z = 7.41 \text{ km} (= 0.5 z_d)$ ).

$C_n^2 \text{ cm}^{2/3}$	$\beta_0^2$	$L_0 / a_0 = \infty$		$L_0 / a_0 = 100$		$L_0 / a_0 = 40$	
		Theory	Monte Carlo	Theory	Monte Carlo	Theory	Monte Carlo
$1 \cdot 10^{-17}$	0.26	0.358	0.356	0.299	0.314	0.240	0.244
$5 \cdot 10^{-17}$	1.31	0.800	0.806	0.710	0.708	0.53	0.55
$5 \cdot 10^{-16}$	13.1	2.58	2.55	2.11	2.18	1.77	1.75

## 6. Small-scale turbulence

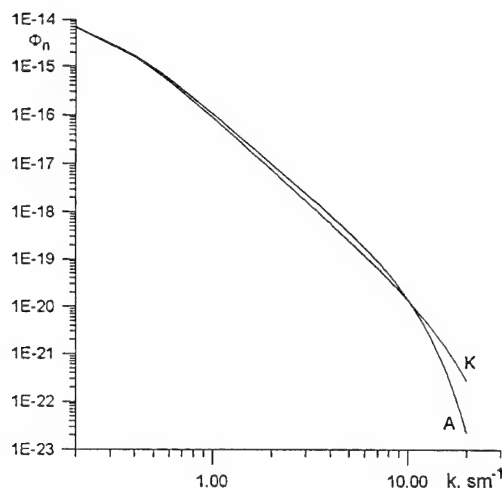


Fig. 6.1

Fig. 6.1. Spectra of the refractive index fluctuations in the atmosphere. A - the Andrews spectrum, K - the modified von Karman spectrum.

In this section we analyze the effect of small-scale fluctuations of the refractive index on statistical characteristics of the laser beam propagating in the turbulent atmosphere. We consider the changes in the following characteristics with the distance: the coherence of light field, the profile of the mean irradiance, irradiance variance and covariance in case of the collimated and focused beams at different parameters of turbulence. The results of Monte Carlo simulations are compared with predictions of the scintillation theory<sup>46</sup> and phase approximation in Huygens-Kirchhoff's method<sup>3</sup>.

The obtained statistical characteristics are the results of processing of the ensemble of light field distributions in the registration plane. In calculations for each realization we follow a random blurring of the beam and put its axis at the origin of the coordinates.

To perform the analysis of the effect of different models of atmospheric turbulence on statistical characteristics of the beam we considered the modified von Karman  $\Phi_a^{MK}(k)$  (3.6) and the Andrews  $\Phi_a^A(k)$  (3.7) spectra. For both models the phase screens were generated using the same arrays of random

numbers in order to exclude random deviations associated with a finite number of realizations  $M$ .

The presented simulations are made for initially Gaussian beams and laser wavelength of  $0.5 \mu\text{m}$ .

#### Computer simulations parameters

- In the case of the collimated beam :

initial beam radius	$a_0=2 \text{ cm}$
length of the path	$z=2 \text{ km}$
inner scale of turbulence	$l_0=4 \text{ mm}$
outer scale of turbulence	$L_0=25 \text{ cm}$
structure constant	$C_n^2 = 3 \cdot 10^{-15} \text{ cm}^{-2/3}$
the irradiance variance	
calculated from the Rytov theory for $z=2 \text{ km}$	$\beta_0^2=17.1$
structure function of phase fluctuation for spherical wave	
on the transmitting aperture for $z=2 \text{ km}$	$D_s(2a)=104.6$

Grid parameters:

number of screens	$S=20$
distance between the screen	$\Delta z=100 \text{ m}$
the variance of phase fluctuations on the screen	$\sigma_\phi^2=3.83 (\Phi_n^{MK}(k))$
grid spacing	$\sigma_\phi^2=4.14 (\Phi_n^A(k))$
number of grid points	$h=1.0 \text{ mm}$
size of the grid	$N_x \times N_y=512 \times 512$
number of realisations	$A_x = A_y=51.2 \text{ cm}$
	$M=80$

For the chosen grid spacing the smallest scale, that can be represented on the grid, is  $r_0=2 \text{ mm}$ . This provides an adequate reproduction of high-frequency structure of fluctuations in the modified von Karman  $\Phi_n^{MK}(k)$  and Andrews  $\Phi_n^A(k)$  spectra, which are shown in Fig. 6.1 at the logarithmic scale.

- In the case of the focused beam :

initial beam radius	$a_0=2 \text{ cm}$
focal length of the lens	$z_f=500 \text{ m}$
length of the path	$z=1 \text{ km}$
inner scale of turbulence	$l_0=4 \text{ mm}$
outer scale of turbulence	$L_0=13 \text{ cm}$
structure constant	$C_n^2 = 5 \cdot 10^{-15} \text{ cm}^{-2/3};$
the irradiance variance	
calculated from the Rytov theory for $z=1 \text{ km}$	$\beta_0^2=8.03$
structure function of phase fluctuation for spherical wave	
on the transmitting aperture for $z=1 \text{ km}$	$D_s(2a)=87.2$

Grid parameters:

number of screens	$S=20$
distance between the screen	$\Delta z=50 \text{ m}$
the variance of phase fluctuations on the screen	$\sigma_\phi^2=1.02 (\Phi_n^{MK}(k))$
	$\sigma_\phi^2=1.15 (\Phi_n^A(k))$

grid spacing  
number of grid points  
size of the grid  
number of realisations

$b=0.25$  mm  
 $N_x \times N_y = 512 \times 512$   
 $A_x = A_y = 12.8$  cm  
 $M=120$

In the case of the focused beam the grid spacing of 0.25 mm allows to reproduce the beam profile in the focal plane of the lens. In vacuum the radius of the focal spot is 0.2 mm.

When the grid spacing  $\Delta z$  along the propagation direction is constant, the number of screens  $S$  decreases as the receiver plane approaches towards the transmitting aperture. However, for  $S \geq 3 \div 5$ , the phase screen model, according to the section 4 of the present paper, is valid.

### 6.1. Field realizations

The typical distribution of the random irradiance in the beam cross-section at different distances from the transmitting aperture is shown in Figs. 6.2, 6.3. The distortions in the beam profile such as, for example, local random focusing, caused by small-scale fluctuations of the refractive index, are clearly demonstrated.

For the collimated beam the effect of the "bump" in the Andrews spectrum (3.7) is observed. At the end of the propagation path the beam breaks up into small-scale speckles (Fig. 6.2b). In the case of the modified von Karman spectrum (3.6) the irradiance distribution is smoother and the characteristic scale of inhomogeneities is larger than in the case of the Andrews spectrum.

In the case of the focused beams the difference between the irradiance distributions obtained for different atmospheric spectra is not so distinct (Fig. 6.3) since strong focusing ( $R_f / L_d = 0.1$ ) to a great extent suppresses phase fluctuations.

### 6.2. Coherence of light field

Spatial coherence of the light field is characterized by the function  $\gamma(\rho)$ . At the beam center this function is given by:

$$\gamma(\rho) = \frac{\langle E(-\rho/2)E^*(\rho/2) \rangle}{(\langle I(-\rho/2) \rangle \langle I(\rho/2) \rangle)^{1/2}}, \quad (6.1)$$

where  $\langle \rangle$  denote averaging over an ensemble of  $M$  realizations.

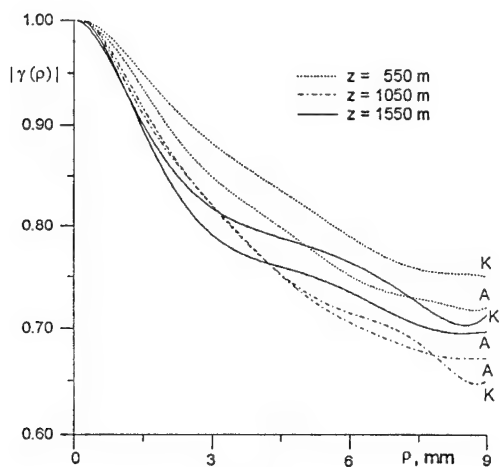


Fig. 6.4a

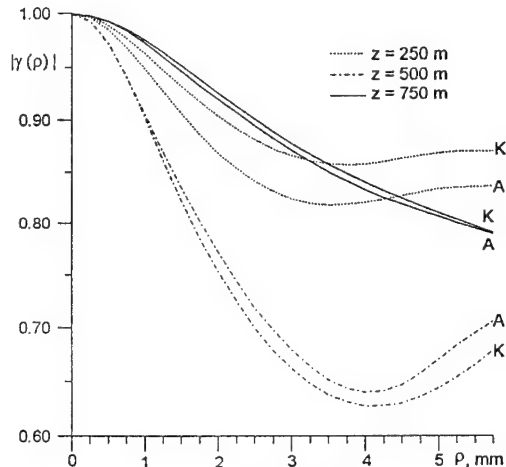


Fig. 6.4b

Fig. 6.4. The coherence function  $|\gamma(\rho)|$  of the beam at different distances for the transmitter.

- a) collimated beam
- b) focused beam

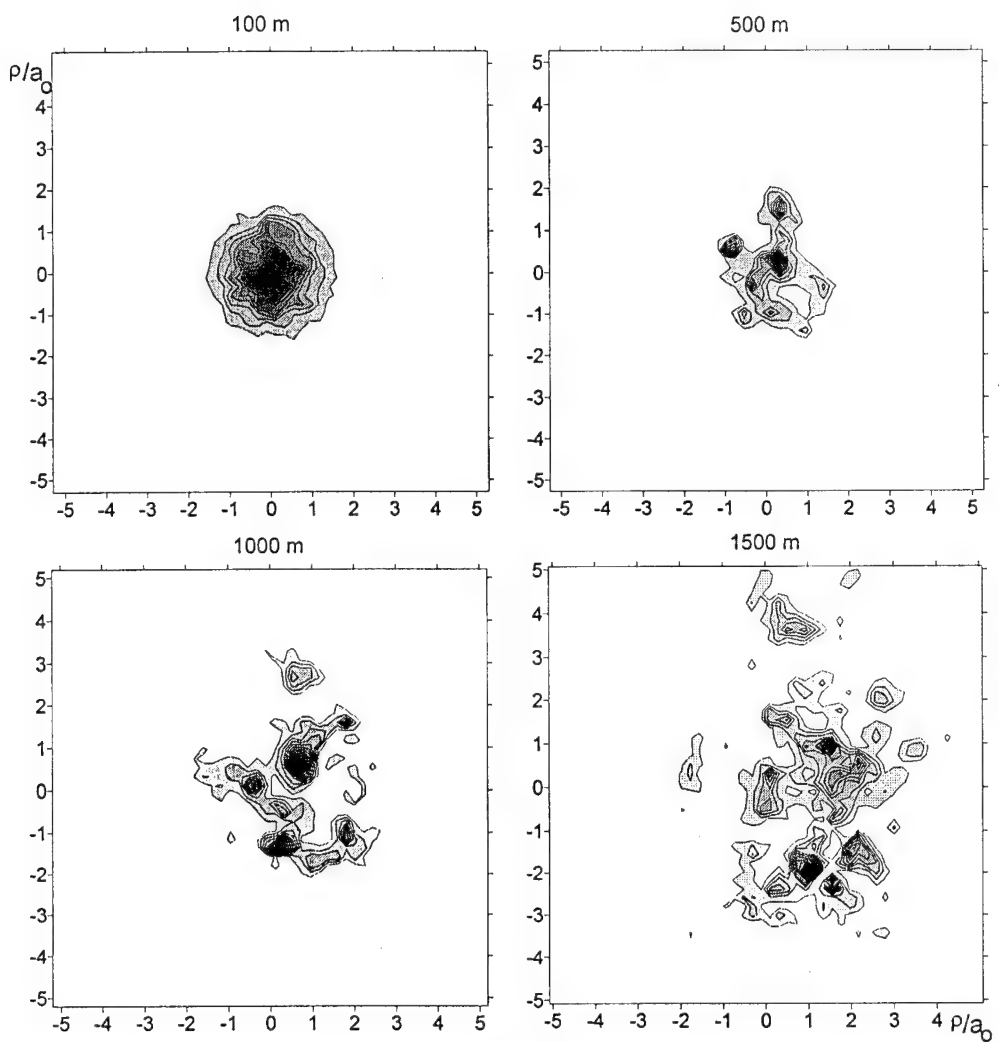


Fig. 6.2a

Fig. 6.2a The propagation of one realization of the collimated beam through the modified von Karman turbulence. Irradiance distributions are registered in different  $z$ -planes along the propagation direction. Irradiance is normalized to a maximum value  $I_m$  in the planes:

$z, m$	100	500	1000	1500
$I_m/I_0$	1.3	3.3	1.6	1.0

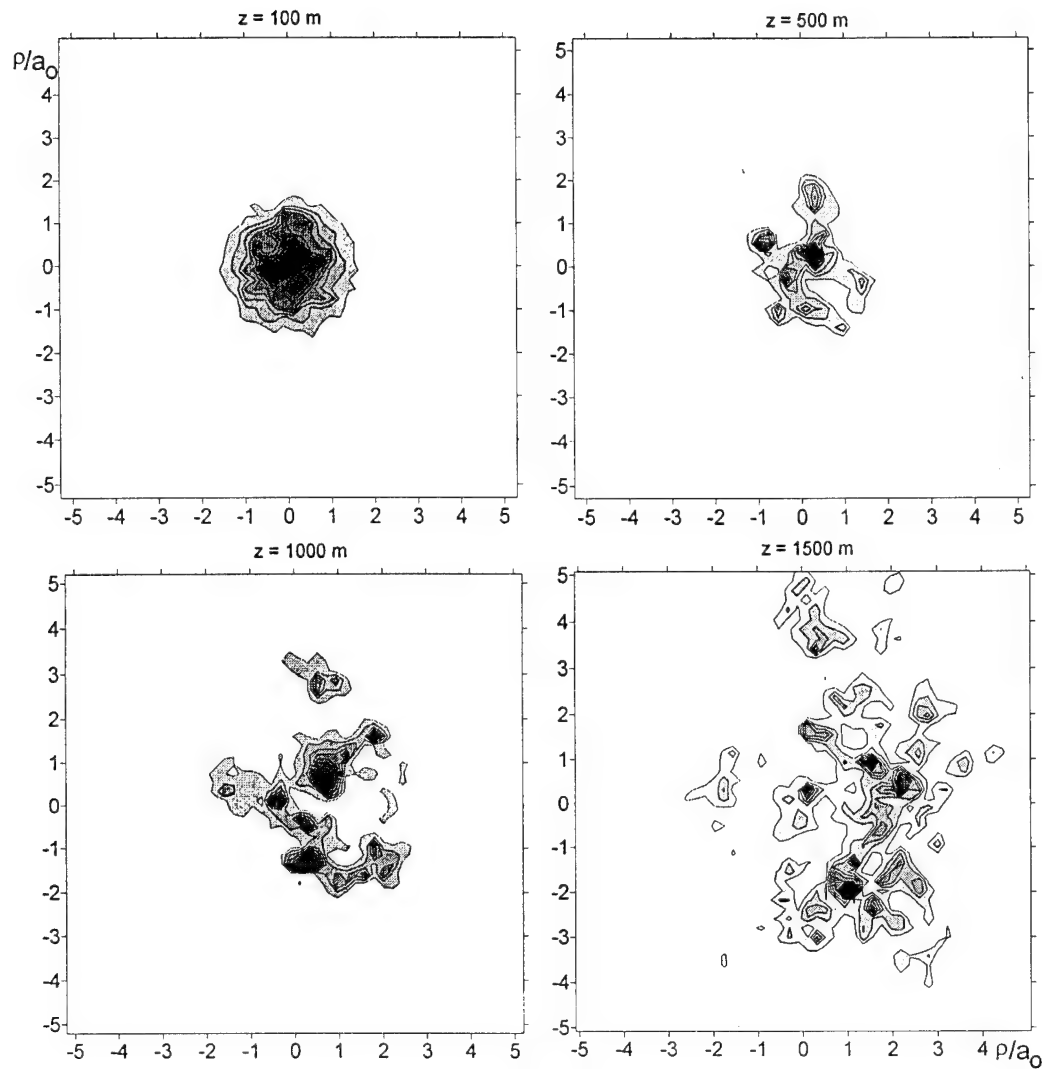


Fig. 6.2b

Fig. 6.2b The propagation of one realization of the collimated beam through the Andrews turbulence. Irradiance distributions are registered in different  $z$ -planes along the propagation direction. Irradiance is normalized to a maximum value  $I_m$  in the planes:

$z, \text{ m}$	100	500	1000	1500
$I_m/I_0$	1.3	3.6	1.2	0.7

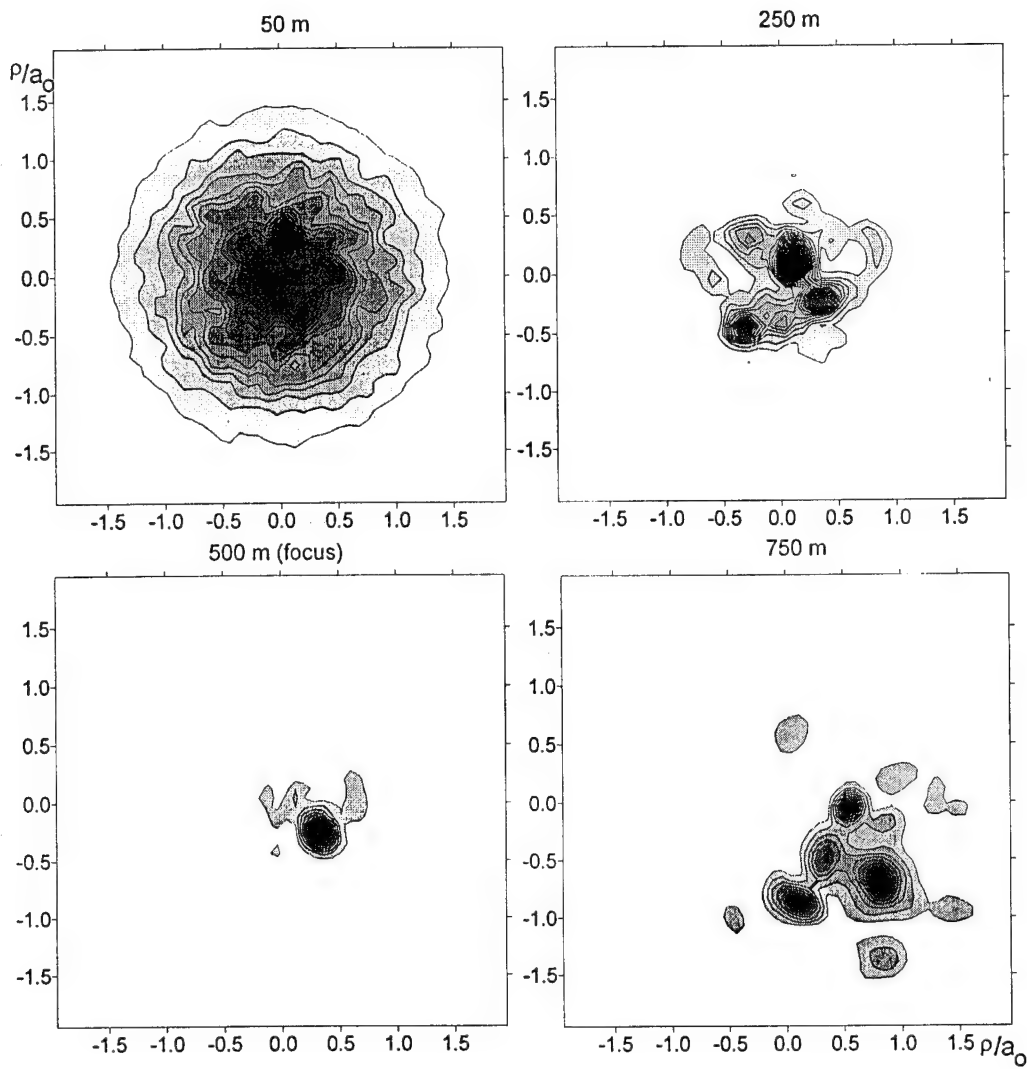


Fig. 6.3a

Fig. 6.3a The propagation of one realization of the focused beam through the modified von Karman turbulence. Irradiance distributions are registered in different  $z$ -planes along the propagation direction. Irradiance is normalized to a maximum value  $I_m$  in the planes:

$z, \text{m}$	50	250	500	750
$I_m/I_0$	1.9	10.6	23.5	5.14

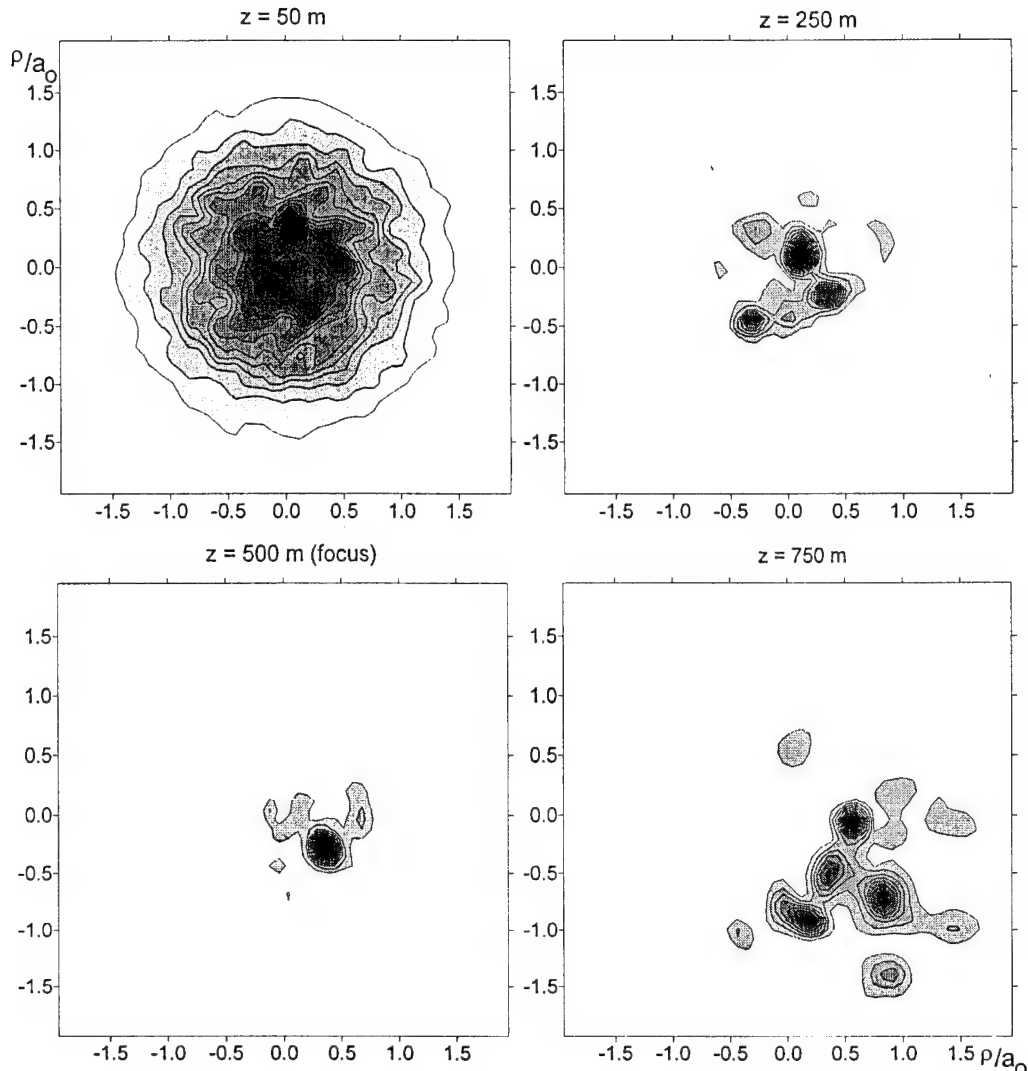


Fig. 6.3b

Fig. 6.3b The propagation of one realization of the focused beam through the Andrews turbulence. Irradiance distributions are registered in different  $z$ -planes along the propagation direction. Irradiance is normalized to a maximum value  $I_m$  in the planes:

$z, \text{m}$	50	250	500	750
$I_m/I_0$	2.0	12.9	22.0	5.6

Fig. 6.4 shows the module of the function  $\gamma(\rho)$  in the cases of collimated and focused beam. The curves are obtained from polynomial interpolation of experimental data:

$$\gamma(\rho) = 1 + \sum_{i=1}^N a_i \rho^{2i} \quad (6.2)$$

In the case of the collimated beam the function  $|\gamma(\rho)|$  at small distances  $\rho \leq 3$  mm becomes narrower as the light propagates along the  $z$ -axis (Fig. 6.4a). At the beginning of the path ( $z=550$  m) the function  $|\gamma(\rho)|$  is significantly narrower for the Andrews spectrum than for the modified von Karman spectrum. The reason for this is the larger contribution of small-scale fluctuations to the spectrum  $\Phi_n^A(k)$  (3.7).

For  $z=1050$  m the functions  $|\gamma(\rho)|$  virtually coincide for both models of atmospheric turbulence. At the end of the propagation path ( $z=1550$  m) the difference between the functions  $|\gamma(\rho)|$  for the models under discussion is revealed only at distances  $\rho > 2$  mm. For  $\rho > 4$  mm and  $z=1550$  m the rate of the decrease in coherence slows down due to natural divergence of the beam.

In the focused beam the changes in  $|\gamma(\rho)|$  with  $z$  are more distinct (Fig. 6.4b). Up to the focal plane  $R_f=500$  the width of the function  $|\gamma(\rho)|$  decreases due to the focusing and atmospheric turbulence. The broadening of the coherency function after the focal plane is caused by a divergence of the beam as a whole. The effect of "bump" in the Andrews spectrum is revealed at distances  $z < R_f$ . In this case the width of the coherency function is less than in the case of the von Karman spectrum. When  $z > R_f$  the discrepancies between coherency functions obtained for two models of turbulence are not large.

In the simulations  $|\gamma(\rho)|$  changes from 1 down to 0.6-0.7. To estimate the radius of coherence  $\rho_E$  at small distances  $\rho$ , we will use a parabolic approximation of  $|\gamma(\rho)|$  in the vicinity of  $\rho=0$ :

$$|\overline{\gamma(\rho)}| = 1 + a_1 \rho^2. \quad (6.3)$$

Defining the radius of coherence at  $e^{-1}$  level of the function  $|\gamma(\rho)|$

$$|\overline{\gamma(\rho_E)}| = e^{-1}, \quad (6.4)$$

we obtain the following expression for  $\rho_E$ :

$$\rho_E = \left( \frac{e^{-1} - 1}{a_1} \right)^{\frac{1}{2}}. \quad (6.5)$$

The change of the radius of coherence  $\rho_E$  with  $z$  for the collimated and focused beams is shown in Fig. 6.5.

In the collimated beam the radius  $\rho_E$  rapidly falls at a distance  $z < z^* = 800$  m. Its further changes with the distance are insignificant (Fig. 6.5a). At a distance  $z = z^*$  the radius of the first Fresnel zone  $r_F = \sqrt{\lambda z^*}$  is 2.0 cm. This value coincides with the initial beam radius  $a_0$ . Thus, at a distance  $z^*$  the decrease in correlation of the light field, caused by joint effects of the turbulence and diffraction, stops.

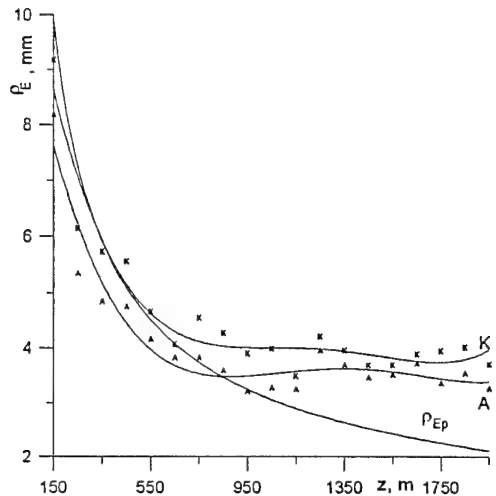


Fig. 6.5a

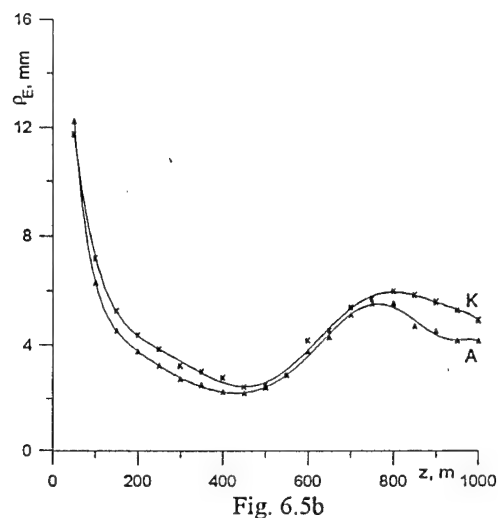


Fig. 6.5b

Fig. 6.5. Radius of coherence  $\rho_E$  as a function of  $z$ . Symbol "K" denotes  $\rho_E$  for the modified von Karman turbulence and "A" for the Andrews turbulence.

- a) collimated beam;
- b) focused beam

At the very beginning of the propagation path  $z \approx 150$  m the radius  $\rho_E$  for the collimated beam may be estimated from the plane wave approximation. Fig. 6.5a shows analytical dependence of the radius of coherence on  $z$  for the case of the plane wave and the Kolmogorov spectrum of atmospheric turbulence<sup>3</sup>:

$$\rho_{EP} = \frac{1}{(1.45 C_n^2 K^2 z)^{3/5}} \quad (6.6)$$

For  $z < 800$  m ( $z \leq 0.15 L_d$ ) the radius of coherence  $\rho_E$  of the beam is close to that of the plane wave  $\rho_{EP}$ . For  $z > 800$  m the natural divergence of the beam compensates for the decrease in correlation in the turbulent atmosphere, and the radius  $\rho_E$  remains practically unchanged. As a result, for  $z > 800$  m radius of coherence  $\rho_E$  of the beam is larger than the radius of coherence  $\rho_{EP}$  of the plane wave. The lower boundary of the region  $z'$ , where  $\rho_E > \rho_{EP}$ , may be estimated from the condition<sup>3</sup>:

$$\frac{L_d}{z} \ll 1.22 \beta_0^{12/5} \quad (6.7)$$

For the parameters under discussion  $z' \approx 700$  m, that is close to the result of numerical simulations. However,

this value of  $z'$  more likely satisfies the weak inequality  $\frac{L_d}{z} < 1.22 \beta_0^{12/5}$  rather than the strong inequality (6.7).

### 6.3 Distribution of the mean irradiance

Mean irradiance profiles were obtained for  $x=0$ . For the collimated beam the irradiance  $\langle I(\rho) \rangle$  at different distances  $z$  is shown in Fig. 6.6. Although the number of realizations is quite large ( $M=80$ ), irradiance profile reveals several peaks, associated with the error of Monte Carlo simulations.

The effect of the small-scale turbulence on the distribution of irradiance in the beam is characterized by a mean short-exposure radius  $a$ . In simulations  $a^2$  is computed from Eq.(5.1).

The radius  $a$  is an integral parameter, that smoothes the irradiance over the beam section. For the collimated beam the value  $a^2$  steadily grows with  $z$  (Fig. 6.7a). Diffractive broadening of the radius  $a$  is not large: it forms approximately 7% for  $z=1.9$  km. Due to the turbulence the beam broadens by a factor of 3-4 while it propagates along the same length. The Andrews model provides the larger broadening than the

modified von Karman model. Fig. 6.7a shows analytical estimate (5.1) of  $a_{eff}^2$  obtained from the theory of

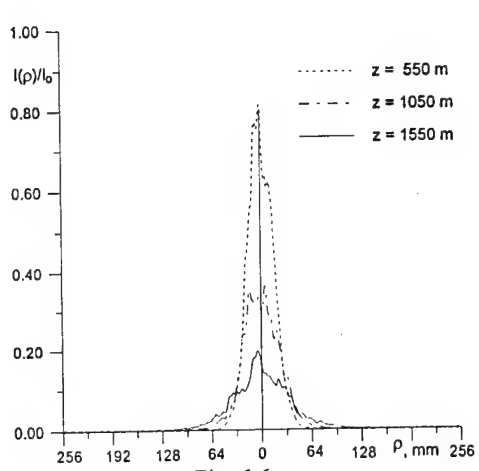


Fig. 6.6a

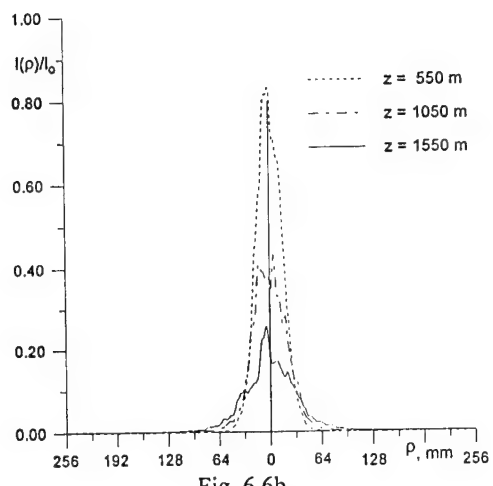


Fig. 6.6b

Fig. 6.6. Mean irradiance  $\langle I(\rho) \rangle$  of the collimated beam in the plane  $x=0$ . a) in the modified von Karman turbulence; b) in the Andrews turbulence.

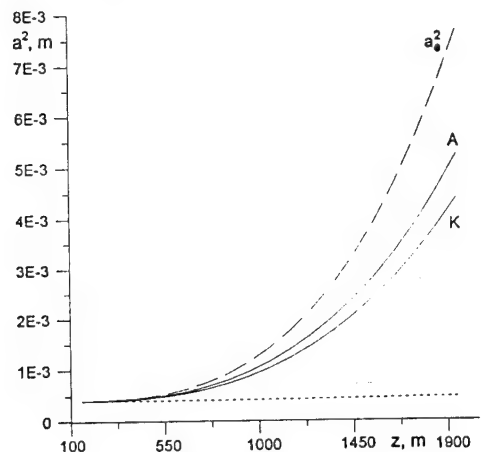


Fig. 6.7a

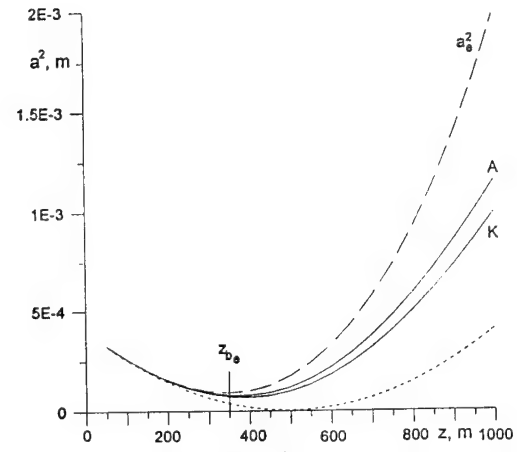


Fig. 6.7b

Fig. 6.7. Square of the mean radius  $a^2$  as a function of  $z$ . Dashed line - without turbulence, long dashed line - theoretical predictions<sup>46</sup>; a) collimated beam; b) focused beam

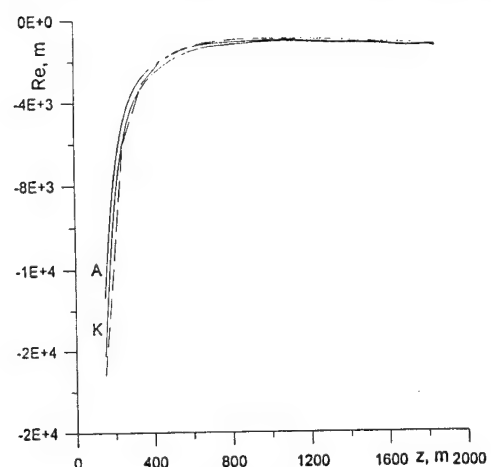


Fig. 6.8a

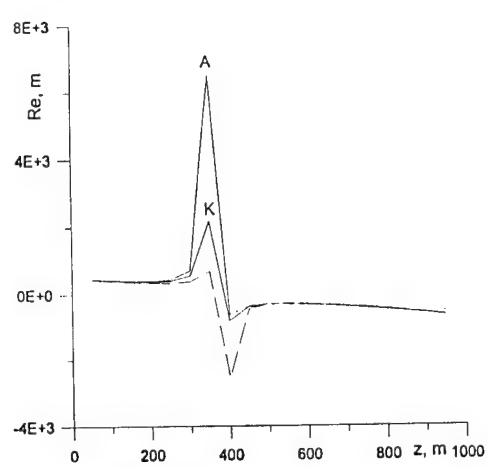


Fig. 6.8b

Fig. 6.8. Effective radius of curvative  $R_e$  as a function of  $z$  in the modified von Karman turbulence and the Andrews turbulence, long dashed line - theoretical predictions<sup>46</sup>; a) collimated beam; b) focused beam.

strong fluctuations in Ref. 46. The analytical estimate of  $a_{\text{eff}}^2$ , that includes both random motion blurring of the beam, exceeds the result of simulations in the conditions of small-scale turbulence.

The obtained from Monte Carlo simulations dependence of  $a$  on distance  $z$  enable us to find the mean radius of curvature  $R_e$  introduced in Ref. 46. Indeed,

$$R_e(z) = -\frac{a(z)}{da(z)/dz}. \quad (6.8)$$

For the collimated beam the change of  $R_e$  with distance is shown in Fig. 6.8a. When  $z > 500$  m the dependencies for the Andrews and von Karman spectrum coincide with theoretical prediction<sup>46</sup>. A discrepancy between theoretical and simulated values of  $R_e$  for  $z < 500$  m arises since our numerical algorithm does not take into consideration random blurring of the beam, though it is precisely this effect, that is responsible for the change in  $R_e$  at the beginning of the propagation path. The discrepancy between the values of  $R_e$  at the beginning of propagation explain the decrease in mean radius  $a$ , as compared with theoretical predictions, at the end of the path (Fig. 6.7a).

For the focused beam simulated values of  $R_e$  coincide with theoretical values<sup>46</sup> for  $z \approx 200$  m  $z > 500$  m (Fig. 6.8b). Some discrepancies in the vicinity of the beam waist are most likely associated with the error in numerical algorithm and require further analysis.

The coordinate of the effective beam waist may be computed from the equation  $\frac{\partial R(z_{be})}{\partial z} = 0$ . For both models of turbulence the beam waist shifts towards the transmitter. The simulated shifts are less than theoretically predicted. The reason for this is underestimating the role of large-scale fluctuations in numerical algorithm.

In the case of the focused beam the peaks of the mean irradiance  $\langle I(\rho) \rangle$  are not high, since for  $R_f / L_u = 0.1$  the behavior of the beam is governed by the focusing. Note, that in the focal plane peak value of the mean irradiance is significantly larger for the modified von Karman model, than for the Andrews model.

The dependence of  $a^2$  on distance for the focused beam is plotted in Fig. 6.7b. As in the case of the collimated beam, theoretical estimate of  $a$  in the case of the focused beam exceeds the values obtained from Monte Carlo simulations.

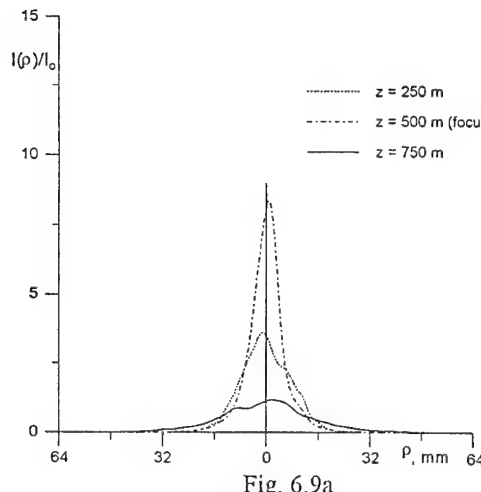


Fig. 6.9a

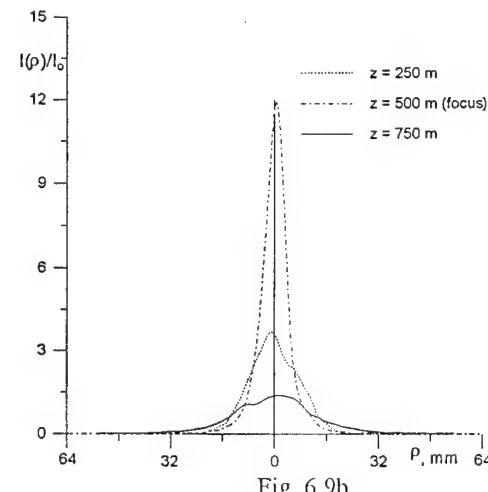


Fig. 6.9b

Fig. 6.9. Mean irradiance  $\langle I(\rho) \rangle$  of the focused beam in the plane  $x=0$ . a) in the Andrews turbulence; b) in the modified von Karman turbulence.

#### 6.4. Irradiance variance

The normalized irradiance variance is computed from the equation:

$$\beta_I^2(\rho, z) = \frac{\langle I^2(\rho, z) \rangle - \langle I(\rho, z) \rangle^2}{\langle I(\rho, z) \rangle^2}. \quad (6.9)$$

For simplicity of notation, we will suppress the  $z$  dependence unless helpful for clarity. In simulations we consider irradiance variance at the beam center  $\rho=0$  and at the diffractive beam edge  $\rho=a_d$ . For the collimated beam the normalized irradiance variance  $\beta_I^2$  grows at the beginning of the propagation path and saturates when  $z > 1000$  m (Fig. 6.10a). The normalized irradiance variance  $\beta_I^2$  is always larger at the diffractive beam edge  $\rho=a_d$  than at the beam center. This is in complete agreement with experimental data and theoretical estimates<sup>3</sup>. Note, that for both the Andrews and the von Karman models of turbulence the dependencies  $\beta_I^2(z)$  are nearly identical.

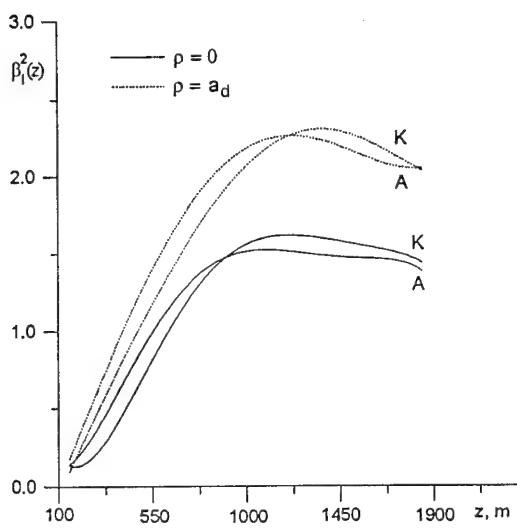


Fig. 6.10a

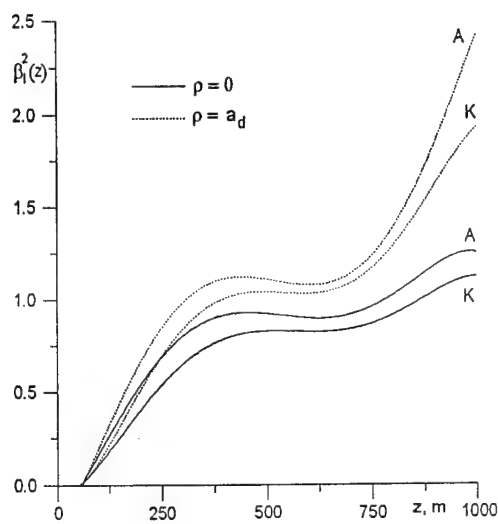


Fig. 6.10b

Fig. 6.10. Irradiance variance for (a) collimated and (b) focused beams.

In the case of the focused beam the normalized irradiance variance  $\beta_I^2$  grows only at the very beginning of the propagation path ( $z < R_f$ ) (Fig. 6.10b). In the vicinity of the effective beam waist in the turbulent atmosphere ( $z=z_{be}$ ) at the beam center and at the diffractive beam edge some decrease in  $\beta_I^2$  is observed.

Past the beam waist, the irradiance variance at the beam center  $\beta_0^2(0)$  slowly increases with the distance, while the variance at the diffractive beam edge  $\beta_I^2(a_d)$  climbs sharply.

Thus, we come to a conclusion that field of irradiance fluctuations in the section of the focused beam is close to statistically homogeneous in the region of weak fluctuations ( $\beta_0^2 < 1$ ) and in the small region beyond the effective beam waist  $z_{be}$ . Immediately in the beam waist  $z \approx z_{be}$  and far beyond it  $z > z_{be}$ , i.e. in the region of strong fluctuations ( $\beta_0^2 \gg 1$ ), the field of irradiance fluctuations in the beam section is statistically inhomogeneous. The latter contradicts the results obtained from the phase approximation in Huygens-Kirchhoff's method<sup>3</sup> and the scintillation theory based on the effective beam parameters<sup>46</sup>, further referred as the "effective" theory.

#### 6.5. Monte Carlo method and the scintillation theory of the effective beam parameters

To compare the results of Monte Carlo simulations with results of the scintillation theory of the effective beam parameters, let us consider the behavior of the log-irradiance variance  $\sigma_{lnI}^2(\rho, z)$  given by:

$$\sigma_{\ln I}^2(\rho, z) = \left\langle \left( \ln \frac{I(\rho, z)}{I_0} \right)^2 \right\rangle - \left\langle \left( \ln \frac{I(\rho, z)}{I_0} \right) \right\rangle^2. \quad (6.10)$$

The log-irradiance variance  $\sigma_{\ln I}^2$  has been calculated at the beam center  $\rho=0$  and at the diffractive beam edge  $\rho=a_d$ .

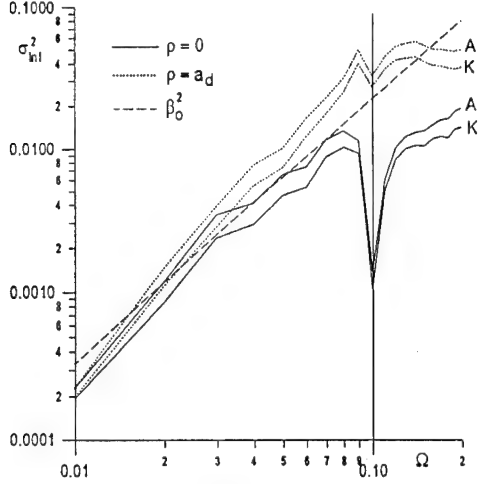


Fig. 6.11

Fig. 6.11. The dependence of the log-irradiance variance  $\sigma_{\ln I}^2(a_d)$  on  $\Omega = z/ka_0^2$  at the diffractive edge and at the center of the focused beam, propagating in weak turbulence  $C_a^2 = 5 \cdot 10^{-17} \text{ cm}^{-2/3}$ .

In simulations the end of the propagation path  $z=1 \text{ km}$  corresponds to  $\Omega=0.2$ . Therefore, from simulations we cannot obtain the stabilization of the variance  $\sigma_{\ln I}^2$  to the log-irradiance variance of a spherical wave. Nevertheless, the results of stochastic simulations are in complete agreement with the results of the weak fluctuation theory and the "effective" theory. Numerical simulations show that for all  $\Omega$  the log-irradiance variance  $\sigma_{\ln I}^2(0)$  in the Andrews model exceeds the log-irradiance variance  $\sigma_{\ln I}^2(0)$  in the von Karman model.

In strong turbulence  $C_a^2 = 5 \cdot 10^{-15} \text{ cm}^{-2/3}$  the behavior of the log-irradiance variance changes dramatically (Fig. 6.12). In the simulations the range of variations in the Rytov variance  $\beta_0^2$  coincide with that considered in Ref. 46. When  $\Omega < \Omega_f$  the variance  $\sigma_{\ln I}^2(0)$  climbs more rapidly than the Rytov variance  $\beta_0^2$  and exceeds  $\beta_0^2$  in the range  $0.3 < \Omega < 0.7$ . Then the growth of  $\sigma_{\ln I}^2$  slows down and  $\sigma_{\ln I}^2$  lies below  $\beta_0^2$ . The value of  $\Omega$ , for which  $\sigma_{\ln I}^2 = \beta_0^2$  is close to the parameter  $\Omega_{fe}$  corresponding to the effective beam waist:

$$\Omega_{fe} = z_{be} / ka_0^2$$

Recall that  $\Omega_{fe} < \Omega_f$  due to the shift of the effective beam waist. Simulation results are close to the predictions of the "effective" theory for  $\Omega < \Omega_{fe}, \Omega_f$ . However, in contrast to these predictions, we did not observe the minimum in the vicinity of  $\Omega_f$ . The further analysis is needed to understand this discrepancy.

For the collimated beam, propagating in weak turbulence, the dependencies of the log-irradiance and Rytov variances on  $z$  lie quite closely (Fig. 6.13). In strong turbulence ( $\beta_0^2 > 1$ )  $\sigma_{\ln I}^2$  stabilizes to a value 1.8. Before the saturation  $\sigma_{\ln I}^2(a_d)$  at the diffractive beam edge is noticeably larger than  $\sigma_{\ln I}^2(0)$ , while in the region of stabilization the difference is not so pronounced.

Following Miller et. al.<sup>46</sup>, let us first analyze the case of the weak turbulence when  $C_a^2 = 5 \cdot 10^{-17} \text{ cm}^{-2/3}$ . Fig. 6.11 shows the log-irradiance variance  $\sigma_{\ln I}^2$  at the beam center  $\rho=0$  and at the diffractive beam edge  $\rho=a_d$  of the focused beam as a function of parameter  $\Omega = z/ka_0^2$ , for parameter  $\Omega_f = R_f / ka_0^2 = 0.1$ . The variance  $\sigma_{\ln I}^2(0)$  begins by closely following the Rytov variance  $\beta_0^2$  in the region  $\Omega < \Omega_f$ , plunging slightly to a minimum in the near vicinity of  $\Omega = \Omega_f$ . Past  $\Omega = \Omega_f$ , the log-irradiance variance  $\sigma_{\ln I}^2$  climbs sharply to a local maximum, then grows, all the way remaining less than the Rytov variance  $\beta_0^2$ . At the diffractive beam edge, the  $\sigma_{\ln I}^2(a_d)$  climbs more rapidly when  $\Omega < \Omega_f$ . When  $\Omega$  is near  $\Omega_f$ , the variance  $\sigma_{\ln I}^2(a_d)$  climbs sharply to a local maximum and then drops at  $\Omega = \Omega_f$ .

In simulations the end of the propagation path  $z=1 \text{ km}$  corresponds to  $\Omega=0.2$ . Therefore, from simulations we cannot obtain the stabilization of the variance  $\sigma_{\ln I}^2$  to the log-irradiance variance of a spherical wave. Nevertheless, the results of stochastic simulations are in complete agreement with the results of the weak fluctuation theory and the "effective" theory. Numerical simulations show that for all  $\Omega$  the log-irradiance variance  $\sigma_{\ln I}^2(0)$  in the Andrews model exceeds the log-irradiance variance  $\sigma_{\ln I}^2(0)$  in the von Karman model.

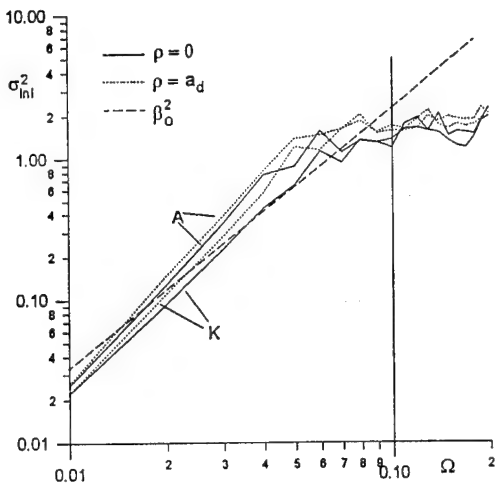


Fig. 6.12

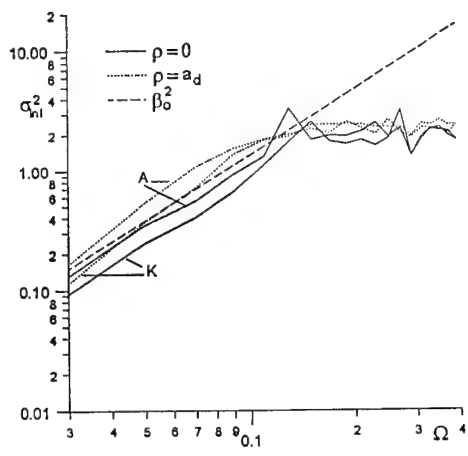


Fig. 6.13

Fig.6.12. The dependence of the log-irradiance variance  $\sigma_{\ln I}^2$  on  $\Omega = z/ka_0^2$  at the diffractive edge and at the center of the focused beam, propagating in strong turbulence  $C_a^2 = 5 \cdot 10^{-15} \text{ cm}^{-2/3}$ .

Fig.6.13. The dependence of the log-irradiance variance  $\sigma_{\ln I}^2$  on  $\Omega = z/ka_0^2$  at the diffractive edge and at the center of the collimated beam, propagating in strong turbulence  $C_a^2 = 3 \cdot 10^{-15} \text{ cm}^{-2/3}$ .

The performed simulations allow to make the following conclusions:

1. In weak turbulence ( $\beta_0^2 \ll 1$ ) the irradiance fluctuations are close to statistically homogeneous. The log-irradiance variance  $\sigma_{\ln I}^2(a_d)$  at the diffractive beam edge exceeds the variance  $\sigma_{\ln I}^2(0)$  at the beam center by 10-20%.
2. In the vicinity of the effective beam waist the irradiance fluctuations in the beam section become statistically inhomogeneous. In weak turbulence the log-irradiance variance  $\sigma_{\ln I}^2(a_d)$  at the diffractive beam edge exceeds the variance  $\sigma_{\ln I}^2(0)$  at the beam center by several orders of magnitude. In strong turbulence ( $\beta_0^2 \gg 1$ ) the difference between  $\sigma_{\ln I}^2(0)$  and  $\sigma_{\ln I}^2(a_d)$  is not large.
3. Beyond the beam waist the irradiance fluctuations are again close to statistically homogeneous.

These conclusions to some extent coincide with the predictions of phase approximation in Huygens-Kirchhoff's method<sup>3</sup> and the "effective" theory<sup>46</sup>.

For the collimated beam the results of Monte Carlo simulations are in complete agreement with theoretical predictions.

## 7. Literature cited

1. A. Ishimaru, *Wave Propagation and Scattering in Random Media*, V.2, (Academic Press, New York, San Francisco, London, 1978).
2. V. I. Tatarskii, *The Effects of the Turbulent Atmosphere on the Wave Propagation*, (National Technical Inform. Service, US Department of Commerce, Springfield, VA, 1971).
3. V.V. Zuev, V.A. Banakh, V.V. Pokasov, *Optics of the Turbulent Atmosphere*, (Gidrometeoizdat, Leningrad, 1988).
4. L.C. Andrews, W.B. Miller, J.C. Ricklin, "Spatial coherence of a Gaussian beam in weak and strong optical turbulence", *JOSA A*, V.11, p.1653 (1994).
5. V.P. Kandidov, "Investigation of statistics of optical radiation in nonlinear medium by the Monte Carlo method", *Bull. Acad. Sci., USSR, Phys. Ser. (USA)*, V.47, p.120-126, (1983).
6. B.J. Uscinski, "Multi-phase-screen analysis", in *Wave Propagation in Random Media*, SPIE, PM-09, p.346 (1992).

7. G.I. Marchuk, *Method Monte Carlo in Optics of the Atmosphere*, (Nauka, Novosibirsk, 1976).
8. V.B. Eflov, Yu.A. Il'inskii, "Method Monte Carlo in problems of transfer of polarized light beams", *Vestnik MSU. Fizika, Astronomia* (in Russian), V.25, p.115 (1984).
9. J.M. Devis, Th.B. Mecee, St.K. Cox, "Application of Monte Carlo method to problems in visibility using a local estimate", *Appl. Opt.*, V.24, p.3193 (1985).
10. M.T. Valley, "Numerical method for modelling nonspherical aerosol modulation transfer functions", *Proc. SPIE*, V.1688, p.73 (1992).
11. Yu.A. Kravtsov, "Propagation of electromagnetic waves through a turbulent atmosphere", *Rep. Prog. Phys.*, p.39 (Printed in UK, 1992).
12. S.M. Rytov, Yu.A. Kravtsov, V.I. Tatarskii, *Introduction to Statistical Radiophysics. Part 2. Random Fields*, (Nauka, Moskva, 1978).
13. A.M. Prokhorov, F.V. Bunkin F.V., K.S. Gochevashvili, V.I. Shishov, "Laser irradiance propagation in randomly nonhomogeneous media", *Sov. Phys. - Usp.*, V.17, p.826 (1975).
14. E.N. Bramley, "The diffraction of waves by an irregular refracting medium", *Proc. Roy. Soc. A.*, V.225, N1163, p.515 (1954).
15. J.A. Ratcliffe, "Some aspects of diffraction theory and their applications to the ionosphere", *Reports on Progress in Physics*, V.XIX, p.188 (1956).
16. E.E. Salpeter, "Interplanetary scintillations. I. Theory", *The Astrophysical Journal*, V.147, p.433 (1967).
17. H.G. Booker, J.A. Ferguson, H.O. Vats, "Comparison between the extended-medium and the phase-screen scintillation theories", *J. of Atm. and Terr. Phys.*, V.47, p.381 (1985).
18. R. Buckley, "Diffraction by a random phase-changing screen: a numerical experiment", *J. of Atm. and Terr. Phys.*, V.37, p.1431 (1975).
19. G.C. Valley, W.P. Brown, "Intensity statistics for propagation through a turbulent layer", *Appl. Opt.*, V.21, p.3002 (1982).
20. B.J. Uscinski, "Analytical solution of the fourth-moment equation and interpretation as a set of phase screens", *JOSA A*, V.2, p.2077 (1985).
21. V.P. Kandidov, V.I. Ledenev, Using the method of statistical tests to the investigation of a wave beam propagation in a randomly inhomogeneous medium", *Izvestiya vuzov. Radiofizika* (in Russian), V.24, p.438 (1981).
22. S.K. Godunov, V.S. Ryaben'kii, *Finite Difference Schemes*, (Nauka, Moskva, 1977).
23. C. Macaskill, T.E. Ewart, "Computer simulation of two-dimensional random wave propagation", *IMA. J. of Appl. Math.*, V.33, p.1 (1984).
24. R.H. Hardin, F.D. Tappert, "Application of the split step Fourier method to the numerical solution of nonlinear and variable coefficient wave equations", *SIAM Review*, V.15, p.423 (1973).
25. St.M. Flatte, F.D. Tappert, "Calculation of the effect of internal waves on oceanic sound transmission", *J. of Acoust. Soc. Am.*, V.58, p.1151 (1975).
26. J.A. Fleck, J.R. Morris, M.D. Feit, "Time-dependent propagation of high-energy laser beams through the atmosphere. I.", *Appl. Phys.*, V.10, p.129 (1976).
27. J. Martin, "Simulation of wave propagation in random media: Theory and applications", in *Wave Propagation in Random Media (Scintillation)*, SPIE, PM-09, p.463 (1992).
28. V.P. Kandidov, V.I. Ledenev, "An investigation of optical pulse thermal blooming in a turbulent medium by the Monte Carlo method", *Sov. J. Quantum Electronics (USA)*, V.11, p.873 (1984).
29. V.P. Kandidov, S.A. Shlyonov, "Spatial statistics of light beam under wind refraction in turbulent atmosphere", *Sov. J. Quantum Electronics (USA)*, V.12, p.1490 (1985).
30. K.D. Egorov, V.P. Kandidov, S.S. Chesnokov, "Numerical analysis of the propagation of high-intensity laser radiation in the atmosphere", *Sov. Phys. J. (USA)*, V.26, p.161-173 (1983).
31. V.P. Kandidov, "Statistics of strong light beams in the turbulent atmosphere", *Bull. Acad. Sci. USSR. Phys. Ser.*, V.49, No 3, p.24-31 (1985).
32. J.M. Martin, St.M. Flatte, "Intensity images and statistics from numerical simulation of wave propagation in 3-D random media", *Appl. Opt.*, V.27, p.2111 (1988).
33. R. Dashen, G.Y. Wang, St.M. Flatte, C. Bracher, "Moments of intensity and log intensity: new asymptotic results for waves in power-law media", *JOSA A*, V.10, p.1233 (1993).
34. St.M. Flatte, G.Y. Wang, "Irradiance variance of optical waves through atmospheric turbulence by numerical solution and comparison with experiment", *JOSA A*, V.10, p.2363 (1993).
35. St.M. Flatte, C. Bracher, G.Y. Wang, "Probability-density functions of irradiance for waves in atmospheric turbulence calculated by numerical simulation", *JOSA A*, V.11, p.2080 (1994).
36. A.S. Monin, A.M. Yaglom, *Statistical Fluid Mechanics*, V.2, (MIT Press, Cambridge, MA, 1975).

37. L.I. Mirkin, M.A. Rabinovich, L.P. Yaroslavskii, "Method of computer generation of correlated Gaussian pseudorandom numbers", Zh. Vychisl. Mat. & Mat. Fiz. (in Russian), V.18, p.1353 (1982).

38. B.J. Herman, L.A. Strugala, "Method for inclusion of low-frequency contributions in numerical representation of atmospheric turbulence", Proc. SPIE, V.1221, p.183 (1990).

39. R.G. Lane, A. Glindemann, J.C. Dainty, "Simulation of a Kolmogorov phase screen", in Waves in Random Media, V.2, No.3, p.209 (1992).

40. E.M. Johansson, D.T. Gavel, "Simulation of stellar speckle imaging", Proc. SPIE, V.2200, p.372 (1994).

41. R.J. Noll, "Zernike polynomials and atmospheric turbulence", JOSA, V.66, p.208 (1976).

42. N. Roddier, "Atmospheric wavefront simulation using Zernike polynomials", Optical Engineering, V.29, p.1174 (1990).

43. D.L.Knepp, "Multiple phase-screen calculation of the temporal behaviour of stochastic waves", Proc. IEEE, V.71, p.722 (1983).

44. S.S. Chesnokov, "Fast Fourier transformation in problems of thermal self-action", Moscow Univ. Phys. Bull. (USA), V.35, p.27 (1980).

45. E. Abitol, N. Ben-Yosef, "Experimental method for the spatio-temporal investigation of atmospheric-turbulence-disturbed wave fronts", JOSA A, V.11, p.2093-2099 (1994).

46. J.C. Ricklin, W.B. Miller, L.C. Andrews, "Effective beam parameters and the turbulent beam waist for initially convergent Gaussian beams", to appear Applied Optics.

47. L.C. Andrews, W.B. Miller, J.C. Ricklin, "Geometrical representation of Gaussian beams propagating through complex paraxial systems", Appl. Opt., V.32, p.5918 (1993).

48. D.M. Winker, "Effect of a finite outer scale on the Zernike decomposition of atmospheric optical turbulence", JOSA A, V.8, p.1568-1573 (1991).

49. S.S. Chesnokov, I.V. Davletshina, A.V. Koryabin, V.I. Shmalhausen, "Laboratory simulation of large-scale wavefront distortions in turbulent atmosphere", in Technical Digest of 8th Laser Optics Conf., V.1, p.22-23, St. Petersburg, Russia (1995).

50. A.S. Gurvich, A.I. Kon, V.L. Mironov, S.S. Khmelevtsov, *Laser Rariation in the Turbulent Atmosphere*, (Nauka, Moskva, 1976).

## Part II

### Optical Simulation of Laser Beam Propagation through the turbulent Atmosphere

#### 1. Introduction

A laser beam in atmosphere is distorted due to refractive index inhomogeneities. Statistics of phase distortions of plane or spherical wave propagating through turbulent medium is well investigated<sup>1</sup>. In practice we often have to deal with a more complicate situation - imaging of an extended object illuminated by a laser beam in an optical ranging system. In such cases computer or optical simulation of laser beam propagation through distorting medium is helpful<sup>2</sup>.

Let us consider a laser beam that is back scattered so that angle  $\theta$  (Fig.1) is small enough. The total phase deviation induced by atmosphere may be represented as a sum of forward and back path terms, so

$$\Delta\varphi = \Delta\varphi_1 + \Delta\varphi_2, \text{ and}$$

$$\langle \Delta\varphi^2 \rangle = \langle \Delta\varphi_1^2 \rangle + \langle \Delta\varphi_2^2 \rangle + 2 \langle \Delta\varphi_1 \Delta\varphi_2 \rangle = 2\sigma^2(1 + K_1(\theta)) \quad (1)$$

$$\text{here } \sigma^2 = \langle \Delta\varphi_1^2 \rangle = \langle \Delta\varphi_2^2 \rangle,$$

$$K_1(\theta) = \langle \Delta\varphi_1 \Delta\varphi_2 \rangle / \sigma^2$$

We can see from (1) that for small values of the angle  $\theta$ , when phase distortions along the beam path 1 - R and 2 - R are almost the same,  $K_1(\theta) \approx 1$  and  $\langle \Delta\varphi^2 \rangle$  is twice greater than that for large angles, when  $K_1(\theta) \ll 1$ . This phenomenon is known as amplification of phase fluctuations in the back scattered beam and is one of so-called double-pass effects. The theory of these effects<sup>3</sup>, well developed for such ideal scattering objects as a point reflector or a plane mirror, becomes more and more sophisticated for complex objects and needs computer simulations or optical modelling.

Some related phenomena appear in imaging of an extended object<sup>4</sup>. Let us consider two rays coming from different points of an object to a single point of receiving aperture: 1-M and 2-M in Fig.2. Turbulence induced phase difference between these two rays, important for the analysis of so-called anisoplanatic effects, is  $\Delta\varphi = \Delta\varphi_1 - \Delta\varphi_2$  and its mean square value may be written as

$$\langle \Delta\varphi^2 \rangle = \langle \Delta\varphi_1^2 \rangle + \langle \Delta\varphi_2^2 \rangle - 2 \langle \Delta\varphi_1 \Delta\varphi_2 \rangle = 2\sigma^2(1 - K_2(\theta)) \quad (2)$$

Correlation function  $K_1(\theta)$  in (1) and  $K_2(\theta)$  in the last formula are the same for a statistically homogeneous layer, but differ if turbulence parameters depend on the coordinate  $z$  along the optical path. These simple examples show close ties between double pass and anisoplanatic phase effects. In general cases, such as imaging of an extended object by a finite aperture optical system or scattering by a non point object, phase effects are more complicated and may be described by means of correlation or, in more general case, mutual structure function<sup>5</sup> (see Fig.3):

$$D_\varphi(\bar{r}_1, \bar{r}_2) = \langle (\Delta\varphi_1 - \Delta\varphi_2)^2 \rangle \quad (3)$$

Both  $K_1(\theta)$  and  $K_2(\theta)$ , provided they exist, may be expressed through  $D_\varphi(\bar{r}_1, \bar{r}_2)$ .

Now one can conclude that for simulation of double pass or anisoplanatic effects we should make a model, that enable us to obtain the mutual structure function  $D_\varphi(\bar{r}_1, \bar{r}_2)$  with desired accuracy. Note that such a

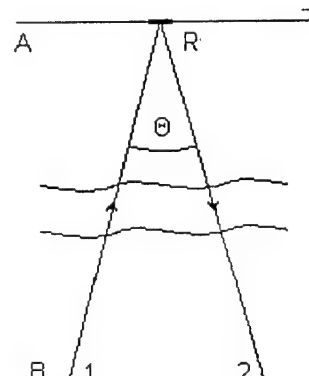


Fig.1

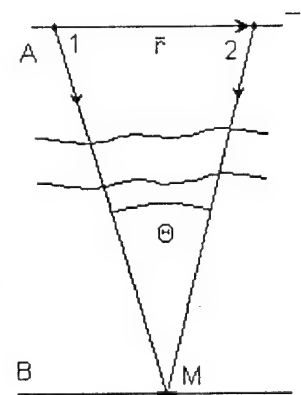


Fig.2

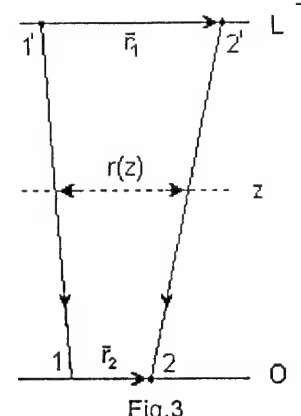


Fig.3

model does not implement amplitude effects, but only phase ones. In many cases this approach is sufficient for adaptive optics systems design and analyses of their efficiency. In other case a more complicated model with a number of phase screens should be used.

## 2. Theoretical background

It is known<sup>6</sup> that in a homogeneous turbulent layer with Kolmogorov power spectrum mean square phase difference between two parallel rays is

$$\langle \Delta\phi^2 \rangle = 2.92 C_n^2 k^2 L r^{5/3} \quad (4)$$

where  $C_n^2$  is the refractive index structure constant,  $k$  - the wave number,  $L$  - the path length and  $r$  - the rays separation distance.

If the rays are not exactly parallel, and the angle  $\theta$  between them is small enough one can apply expression (4) to each thin layer (see Fig.3) and summarise their contributions along the path:

$$\langle \phi^2 \rangle = 2.92 k^2 \int_0^L C_n^2(z) [r(z)]^{5/3} dz. \quad (5)$$

In the case considered above  $r(z) = \left| \vec{r}_1 \cdot z / L + \vec{r}_2 \cdot \frac{L-z}{z} \right|$  (5a)

If  $C_n^2$  does not depend on  $z$  the integral in (5) can be calculated both analytically (by a rather sophisticated expression) or by a computer. For non-Kolmogorov spectra the analysis is more complicated and a different technique is used<sup>4,7</sup>. The integral representation (5) of the mutual structure function  $D$  can be easily applied to compare it with different models of turbulent layer. For computer and optical simulation of imaging system performance a number of phase screen models has been used<sup>8-10</sup>. These models were designed to simulate single pass optical wave propagation and their possibility for double pass and anisoplanatic effects simulation was not examined yet. That can be done calculating the errors in representation of mutual structure function by a chosen model. Another way is to construct a model of turbulent layer in such a way, that it should reproduce properly correlation between two rays, propagating at a small enough distance.

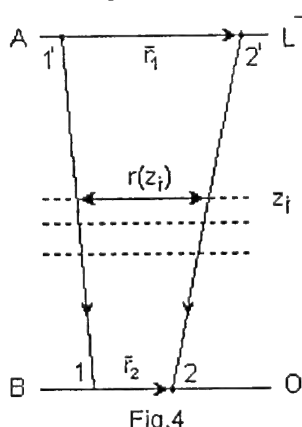


Fig.4

Let us consider a model consisting of  $N$  phase screens placed between planes A and B at arbitrary positions (Fig.4). Each phase screen is described by its structure function  $D_i(r) = A_i r^{5/3}$ . Assuming these phase screens are statistically independent, and  $A_1=A$  one can write for mean square phase difference between beams 1-1' and 2-2':

$$\langle \phi^2 \rangle = \sum \langle \phi_i^2 \rangle = A \cdot \sum |r(z_i)|^{5/3} \quad (6)$$

The formula (6) is a discrete approximation for integral (5), and the problem now is to choose properly the number of the screens and their coordinates to provide sufficient accuracy. In more general case screen weights  $A_i$  may be not equal.

We can consider some physics principles for optimisation of the set of phase screens:

1. The distortions of plane wave should be represented exactly. For this purpose we can use only one phase screen, or a number of arbitrary located screens. The sum of their intensities  $A_i$  should be equal to the total coefficient for the plane wave:

$$\sum A_i = 2.92 \cdot C_n^2 k^2 L = A_0 \quad (7)$$

The relation (7) does not define different values  $A_i$  and coordinates  $z_i$ , but it should be valid for any phase screens representation.

2. The model should represent exactly not only the plane wave distortions, but also distortions in spherical waves emitted both in planes A or B. As the configuration is symmetrical we may try to design a system of two identical phase screens, located at equal distances from planes A and B.

Using (7) we find  $A_1=A_2=A_0/2$ . From (6) we can write

$$\frac{A_0}{2} \left( [h\theta]^{5/3} + [(L-h)\theta]^{5/3} \right) = \frac{3}{8} A_0 (L\theta)^{5/3}$$

The coefficient 3/8 in the right part of the last equation appears from the well known result for phase fluctuations in a spherical wave<sup>6</sup>.

This gives us an equation  $\alpha^{5/3} + (1-\alpha)^{5/3} = 3/4$ ,  $\alpha = h/L$ . (8)

The numerical solution of (8) gives  $\alpha=0.21$ . A regular technique for phase screen model design can be based on the Gaussian quadrature formula<sup>12</sup>, that enables us to calculate best coordinates  $z_i$  and screen weights for a given number of screens. For two screens the result obtained by the last technique does not differ significantly from that obtained above.

### 3. Two phase screen method

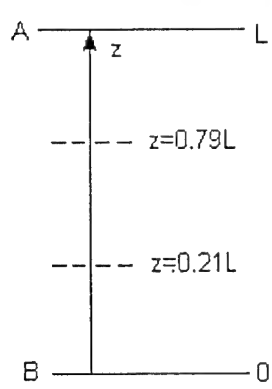


Fig.5

Let us consider a model of turbulent layer consisting of two phase screens placed as shown in fig.5. For mutual structure function one can write

$$D_\phi(\bar{r}_1, \bar{r}_2) = \frac{A_0}{2} \left\{ [(1-\alpha)\bar{r}_1 + \alpha\bar{r}_2]^{5/3} + [\alpha\bar{r}_1 + (1-\alpha)\bar{r}_2]^{5/3} \right\} \quad (9)$$

Applying  $\alpha=0.21$  we obtain an analytical approximation for  $D_\phi$ :

$$D_\phi(\bar{r}_1, \bar{r}_2) = \frac{A_0}{2} \left\{ [0.79\bar{r}_1 + 0.21\bar{r}_2]^{5/3} + [0.21\bar{r}_1 + 0.79\bar{r}_2]^{5/3} \right\} \quad (10)$$

here  $A_0 = 2.92 C_n^2 k^2 L$ , (see the coefficient before  $r^{5/3}$  in the formula (4) for mean square phase fluctuations in a plane wave).

The last formula is useful both for analytical consideration and computer simulation of anisoplanatic effect in statistically homogeneous layer. If  $C_n^2$  dependence on the coordinate  $z$  along the path is significant,

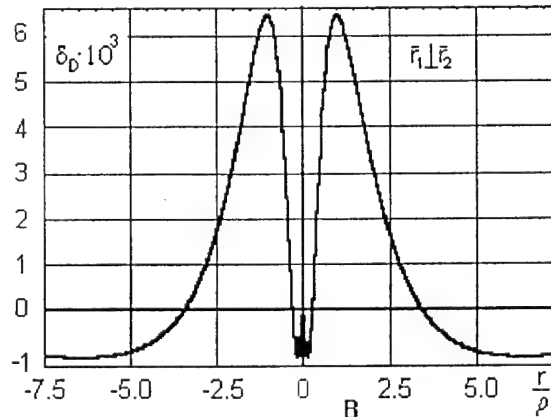
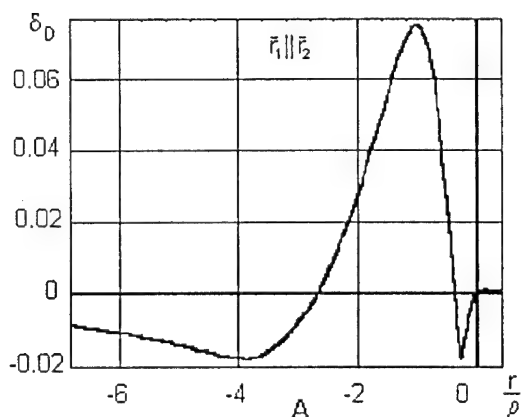


Fig.6

Approximation errors of  $D_\phi(\bar{r}_1, \bar{r}_2)$  calculations: A -  $\bar{r}_1 \parallel \bar{r}_2$ , B -  $\bar{r}_1 \perp \bar{r}_2$ .

- the coordinates of the phase screens should be calculated using Gauss quadrature technique.

We have compared the analytical approximation (10) with result obtained by direct computation of  $D_\phi(\bar{r}_1, \bar{r}_2)$  via integral representation (5). The difference  $\delta_D$  between these two solutions is shown in Fig.6a (for  $\bar{r}_1 \parallel \bar{r}_2$ ) and in Fig.6b (for  $\bar{r}_1 \perp \bar{r}_2$ ). We can see that in the worst case  $\bar{r}_1 = -\bar{r}_2$  approximation error does not exceed 8%. In other cases it is much less. The function  $D_\phi(\bar{r}_1, \bar{r}_2)$  is most frequently used in integral expressions, so the accuracy obtained is sufficient for many applications. Two screen model is useful particularly for optical modelling, because it is very difficult to construct such a model with more than two screens.

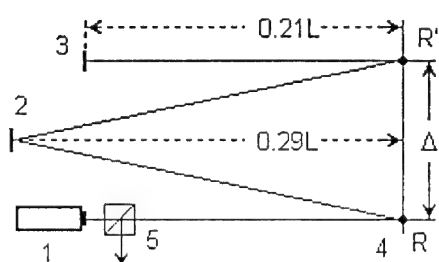


Fig.7

The single screen model with double beam pass and reflecting random phase screen.

For simulation of short scale distortions a single screen model with double beam pass can be used. In Fig.7 a possible optical scheme with reflecting random phase screen is shown.

#### 4. Optical simulation technique for anisoplanatic and double pass effects investigation

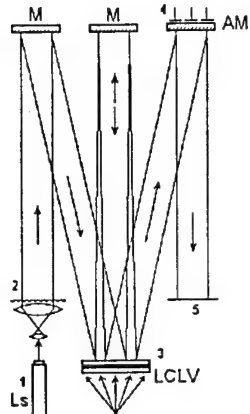


Fig.8  
Schematic of the possible experimental arrangements

A phase screen method can be applied to design an optical setup for turbulence induced phase effects investigation. To simulate "frozen" turbulence computer designed phase screens may be used<sup>11</sup>. For optical "on-the-bench" turbulence simulation light controlled spatial phase modulators, such as liquid crystal light valve (LCLV), are of great interest<sup>2,10</sup>. These devices are especially useful to produce phase screens with relatively short scale small amplitude phase distortions. As we can see from previous consideration this ability is of great importance in anisoplanatic and double pass effects studying. As for large scale distortions, especially low order Zernike modes, they can be successfully simulated by computer controlled flexible mirrors<sup>2,8</sup>.

A schematic of the possible optical arrangements is shown in Fig.8. A main difference between this optical scheme and that proposed before<sup>2</sup> is that the light beam generated by laser source Ls is twice reflected by LCLV surface in accordance with conclusions of the theoretical analysis given above. Another difference is that to produce a random phase modulation a laser induced speckle field is supposed to control LCLV. A flexible mirror 4 can be used, if needed, to induce low order phase distortions. After reflection from this mirror the laser beam reaches the input plane 5 of an imaging system, designed for the performed experiment. An image of a test object 2 or intensity distribution in output laser

beam is registered by a CCD camera and processed by a computer. The key element of our experimental setup is a reflective LCLV 3, that transforms the intensity of the speckle field into random phase modulation of the redout beam.

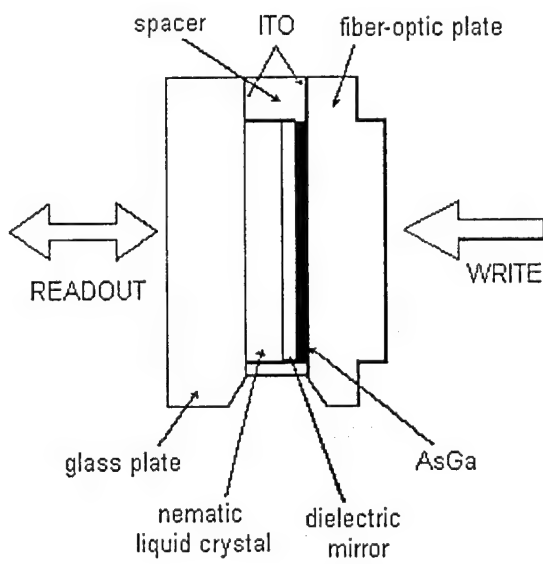


Fig.9  
Liquid crystal spatial phase modulator

The general configuration of the device is shown in Fig.9. The ac light valve consists of a number of thin film layers sandwiched between two glass substrates. A low voltage (5-20 Vrms) audio frequency power supply is connected to the two outer, thin film indium-tin-oxide (ITO) transparent electrodes and thus across the entire thin film sandwich. The 50-micron gallium arsenide (AsGa) semiconductor is used as photosensitive layer. The dielectric mirror and cadmium telluride light blocking layer isolate photoconductor from the readout light beam. The optical isolation between readout light and photoconductor exceeds  $10^4$ . This is one of the major design features of the ac light valve, as it enables simultaneous writing and reading of the device without regard to the spectral composition of the two light beams. Furthermore, the dielectric mirror prevents the flow of the dc current through the liquid crystal and this enhances the lifetime of the device. The chemically inert insulating layers  $\text{SiO}_2$  bounds the liquid crystal layer at both interfaces.

The liquid crystal that is used in this device is a biphenyl nematic material. The thickness of that layer is 10 microns. The optical birefringence effect of nematic liquid crystal<sup>18</sup> is used in this device. The liquid crystal molecules at the electrodes are aligned with their long axes (director) parallel to the electrode surfaces (homogeneous alignment). In addition, they are aligned to lie parallel to each other along the preferred direction that is fabricated into the device. In

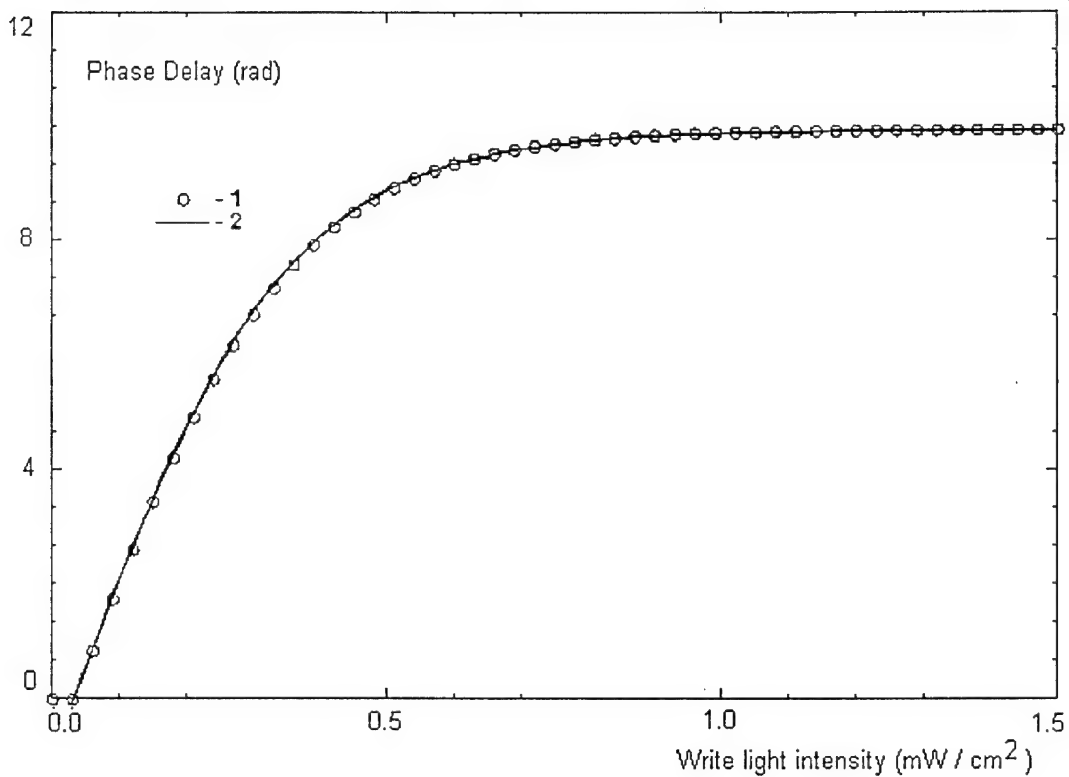


Fig.10  
The sensitivity curve of the LCLV

order to obtain pure phase modulation, the directions of liquid crystal alignment are the same at the both interfaces (instead twisted nematic used in<sup>19</sup>). For the same purposes the director should be oriented parallel with the readout beam polarization.

Without input illumination the dynamical resistance of the photoconductor layer under applied ac voltage is much higher then the resistance of liquid crystal. Consequently, applied voltage almost completely falls on the photoconductor. Let us consider what happens in a illuminated element. In the idealized case, the incident photons introduce a leakage resistance across the photoconductor and a part of applied voltage acts on the liquid crystal layer. This voltage causes the S-type deformation in the liquid crystal layer, and as a result the local refraction index variation.

The response time of the device is 20-25 ms for phase modulation equal  $\pi$ ,  $\lambda=0.63\mu\text{m}$ . The spatial resolution is about 10 line pairs/mm at the 50% MTF. The sensitivity curve for LCLV is presented on the Fig.10. We can see that in the interval  $(0-2\pi)$  phase modulation is almost linear via input intensity.

## 5. Random optical field generation.

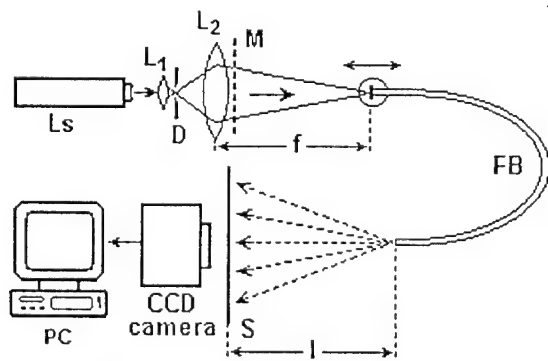


Fig.11. Speckles generation setup.

For generation of time-independant or dynamic random optical field speckle technique may be used, see fig.11. Optical scheme includes lenses L1, L2 and diaphragm D to focus laser beam at the receiving edge of a fiber bundle FB. A mask M can be placed in front of the focusing system in order to control the light intensity distribution at the FB edge. The receiving edge of FB is placed on adjustable translating mount, that allows to change the size of the light spot entering the FB edge. The second edge of the bundle may be considered as a set of elementary coherent light sources. The phases of these sources are randomly distributed in  $(0, 2\pi)$ .

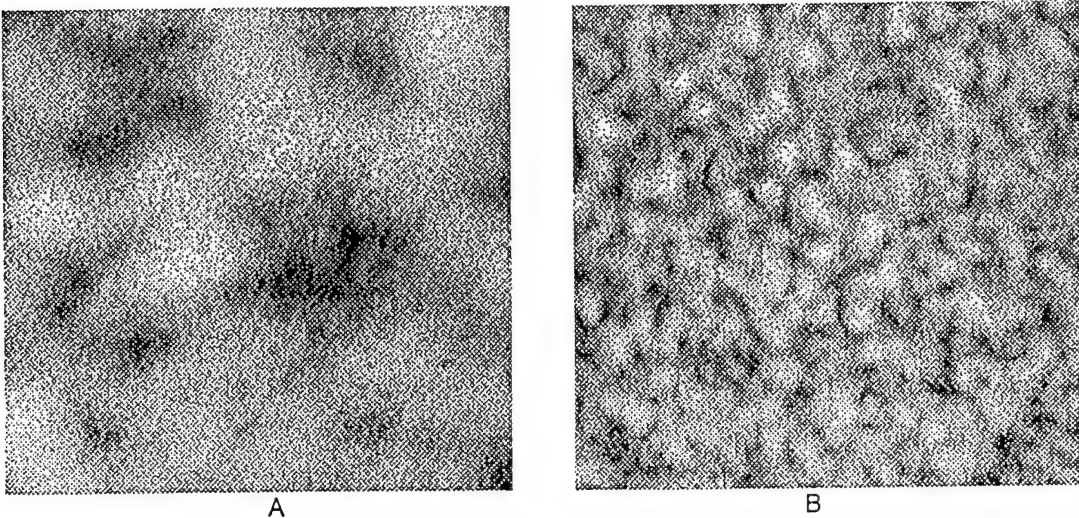


Fig.12  
Optical speckles patterns

interval and their amplitudes corresponds to the intensity distribution at the input edge of FB. The speckle field at the screen S is registered by CCD camera. Patterns of random light intensity distribution for a number of FB input edge positions are shown in fig.12.

The electronics used in experiments allows us to obtain digital intensity distribution images with 512x512 resolution and 256 gray scale coding. The total field of view on pictures shown in fig.12 is about 1.5 cm, so we can easily produce speckle fields with the typical average spot size from less than 1 mm to about than 1 cm.

First step to calculate cross-correlation function of the speckle field produced is smoothing of the intensity array  $I_{ij}$ . In order to suppress high spatial frequency noise of the CCD camera and relay electronics we smooth pictures by a simple mask:

$$\frac{1}{16} \begin{pmatrix} 1 & 2 & 1 \\ 2 & 4 & 2 \\ 1 & 2 & 1 \end{pmatrix}$$

To get the estimate of the speckle field correlation function we select a number of equidistant rows (usually 16) and calculate the "horizontal" correlation functions  $\tilde{K}_{H,i}$  in accordance to the formula:

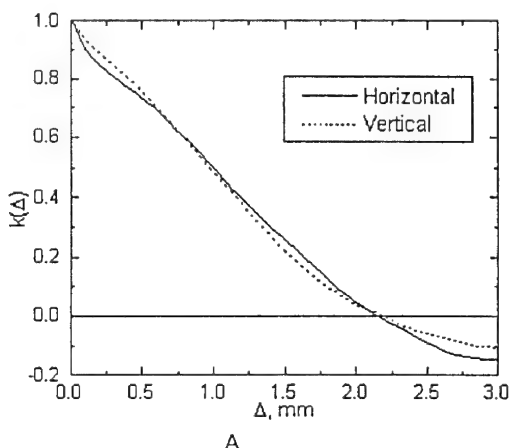
$$\tilde{K}_{H,i}(\Delta) = \frac{1}{512 - \Delta} \sum_{j=1}^{512-\Delta} [I(i, j) - \bar{I}_i][I(i, j + \Delta) - \bar{I}_i]$$

where by  $\bar{I}_i$  we denote the average intensity of the  $i$ -th row. Almost the same formula is used to calculate "vertical" correlation functions  $\tilde{K}_{V,j}$  (averaging along the columns of the picture). The larger the separation  $\Delta$  the fewer number of overlapped points, hence the higher the variance of the estimate. This means that we can only make reasonable estimate of the correlation functions at separation out to about 1/4 of the image size, so in our calculation we use  $[0, 128]$  separation range for  $\Delta$ . As the last step the average correlation functions  $\tilde{K}_H$ ,  $\tilde{K}_V$ ,  $\tilde{K}$  are calculated:

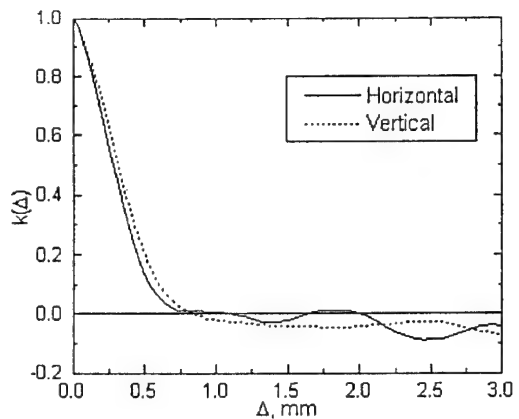
$$\tilde{K}_H = \frac{1}{16} \sum_{i=1}^{16} \tilde{K}_{H,i}, \quad \tilde{K}_V = \frac{1}{16} \sum_{j=1}^{16} \tilde{K}_{V,j}, \quad \tilde{K} = \frac{1}{2} (\tilde{K}_H + \tilde{K}_V)$$

Before calculating 'general' function  $\tilde{K}$ , the "vertical" correlation function  $\tilde{K}_{V,j}$  is rescaled to the same scale as  $\tilde{K}_{H,i}$ . Correlation functions for the images, represented in fig.12, are shown in fig.13. We can see that  $\tilde{K}_H$  and  $\tilde{K}_V$  are very similar, so the speckle field produced is spatially homogeneous and the function  $\tilde{K}$  may be considered as a general characteristics of the field.

It is a well known fact that correlation function of the speckle field intensity may be considered as Fourier transform of intensity distribution in the emitting plane<sup>14,15</sup>. Provided the input plane of FB is the focal plane of the lens system L1,L2, the field distribution in that plane is proportional to Fourier transform of the mask M transmittance profile<sup>16</sup>. When the mask is binary, that is one part of it transmits light completely



A



B

Fig.13  
Normalized correlation functions for the images, represented in fig.12a,b

and the other part doesn't, we can speak just about its shape and size. Making use of Fourier transform properties one can obtain the next formula for output correlation function:

$$K(\bar{\rho}) = c \int M(\bar{r} + \frac{1}{2}m\bar{\rho}) M(\bar{r} - \frac{1}{2}m\bar{\rho}) d^2 r \quad (11)$$

where  $m=l/f$  is the scale factor,  $\bar{\rho}$  is the vector of a point in the output plane, and  $\bar{r}$  is the vector of a point in the mask plane and  $c$  - normalizing constant.

While deriving (11) it was assumed, that the illuminating beam is uniform and the input edge of FB is located exactly in the focal plane of the L1-L2 lens system. A small shift of the input edge of FB completely changes the correlation function, and unfortunately the expression for  $K(\bar{\rho})$  in this case becomes much more complicated.

In practice we can obtain desired shape of the generated speckle field correlation function by changing the mask shape and adjusting the bundle input edge position. Applying this random light field to the photosensitive layer of LCLV we can produce optically controlled phase distortions.

Dynamical phase distortions can be simulated by moving the fiber bundle. Small displacement of emitting end provides a moving speckle pattern, while bending its middle part causes a change of random field realisations, somewhat like optical turbulence.

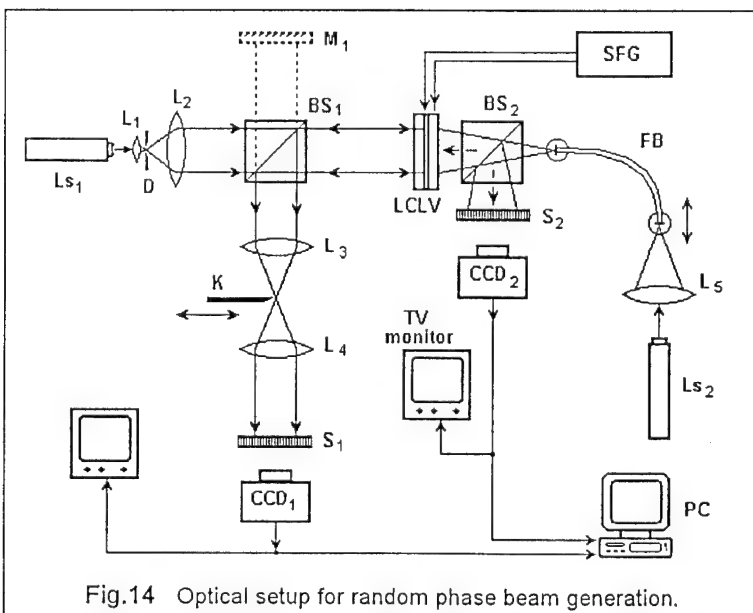


Fig.14 Optical setup for random phase beam generation.

## 6. Experimental results on random phase beam generation

Optical setup made in Adaptive Optics laboratory to introduce the short scale phase distortions in laser beam is shown in fig.14. The light beam of the laser  $L_{s1}$  is expanded by the lenses  $L_1, L_2$ . After reflection from the LCLV readout surface the phase modulated light is diverted by the beam splitter  $BS_1$  into the measuring arm. Sound frequency generator SFG served as ac power supply for LCLV.

Control speckle field is produced by laser  $L_{s2}$ , lens system

$L_5$  and fiber bundle FB. Part of the control speckle beam is diverted by the beam splitter  $BS_2$  to the screen  $S_2$  and video camera  $CCD_2$ .

To make the phase distortions visible we used a Foukot knife technique<sup>17</sup>, implemented by lenses  $L_3, L_4$  and knife edge K. To produce the image of the LCLV surface on the screen  $S_1$  the distances  $L_{CLV} - L_3$ ,  $L_3 - K$ ,  $K - L_4$  and  $L_4 - S_1$  equal to double focal length of lenses  $L_3, L_4$ .

Some examples of control speckle field and produced phase maps, visualized by Foukot knife technique, are shown in Fig.15, corresponding correlation functions for this patterns are shown in fig.16.

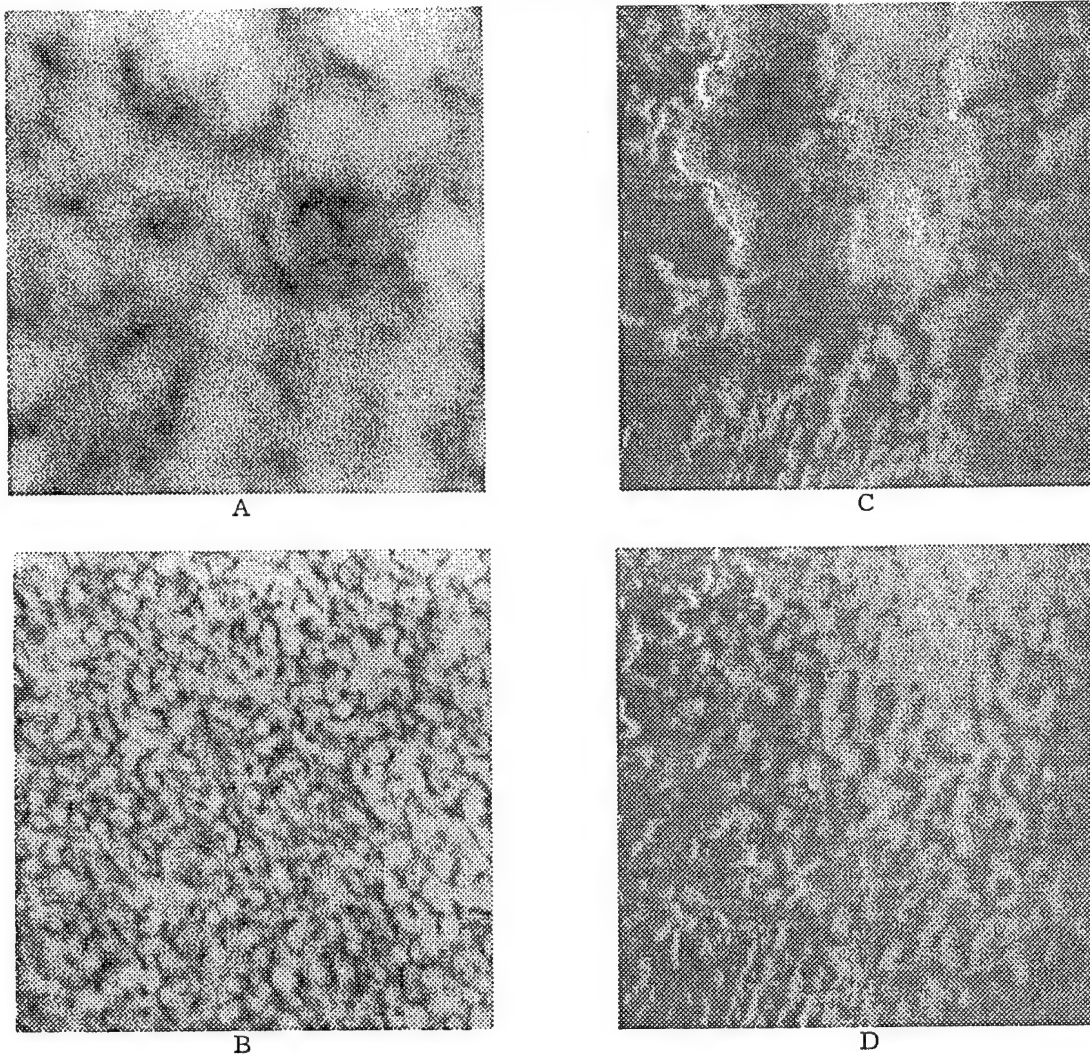
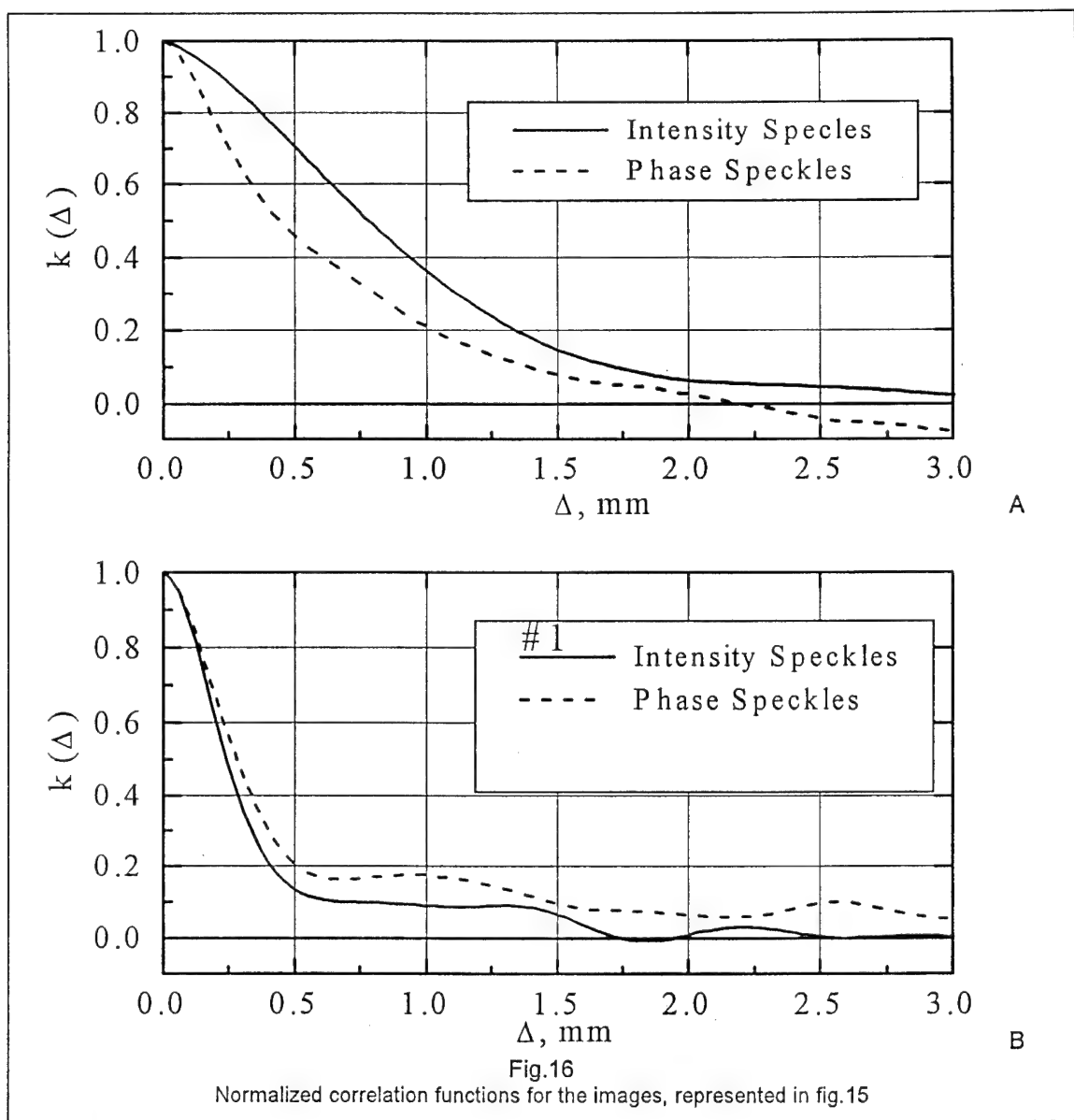


Fig.15  
Control speckle field (A, B) and produced phase patterns (C, D)

We can see, that correlation functions calculated for obtained phase patterns reveals good coincidence with that of the control fields. Some increase of the short scale speckles weight in the phase correlation functions is due to Foukot knife technique influence.

## 7. Conclusions

Possibility of double-pass and anisoplanatic effects simulation by few phase screen model is discussed. A two phase screen model of a turbulent layer is proposed and its accuracy in representation of mutual structure function is examined. An experimental set-up for experimental investigation of anisoplanatic effects with a dynamic phase spatial modulator is designed. A method of generation of random optical field with wide range correlation length is proposed and experimentally tested.



## 8. Literature Cited

1. A.Ishimaru. *Wave propagation and scattering in random media*, Academic Press, New York, 1978.
2. M.A.Vorontsov, J.C.Ricklin, G.W.Carhart. Optical simulation of phase distorted imaging systems: Nonlinear and adaptive optics approach. Optical engineering special issue: *Optical remote sensing and signal processing*.
3. A.V.Polovinkin, A.I.Saichev. Izv. Vuzov, Radiphis., v.24, No 4, p433, 1980.
4. D.L.Fried. Journ. Opt. Soc. Am., v.72, No 1, p.52, 1982.
5. R.E.Lutomirski, H.T.Yura. Journ. Opt. Soc. Am., v.61, No 4, p.482, 1971.
6. S.M.Rytov, Yu.A.Kravtsov, V.I.Tatarskii. *Introduction to statistical radiophysics*, Moscow, Nauka-Press, 1985.
7. P.H.Hu, J.Stone, T.Stanley. Journ. Opt. Soc. Am., A, v.6, No 10, p.1595, 1989.
8. Simulation of Image Distortions in turbulent Atmosphere. Techn. report, Edited ILC MSU.1995
9. M.A.Vorontsov, J.C.Ricklin, W.B.Miller, N.I.Iroshnikov. Proc.SPIE, 2312, p.136, 1994.

10. S.S.Cheznokov, I.V.Davletshina, A.V.Koryabin, V.I.Shmalhausen. Laboratory simulation of large scale wavefront distortions in turbulent atmosphere. 8-th Laser Optics Conference, Technical Digest, v.1, p.22, St.Petersburg, 1995.
11. V.P.Kandidov, S.A.Shlenov. Ultimate possibilities of computer simulation in problems of optical propagation through turbulent atmosphere. 8-th Laser Optics Conference, Technical Digest, v.1, p.22, St.Petersburg, 1995.
12. C.Lanczoc. *Applied Analysis*. Prentice Hall. 1956
13. J.C.Ricklin, M.A.Vorontsov, G.W.Carhart, D.Gose, W.B.Miller. *Journ. of mod. Opt.*, v.42, No 1, p.13, 1995.
14. V.V.Anisimov, S.M.Kozel, G.R.Lokshin. Sov. Radiotekh. and Electron., v.15, No 3, p.539, 1979.
15. *Laser Speckle and Related Phenomena*. Ed. J.C.Dainty. Topics in Applied Physics, v.9.
16. J.W.Goodman. *Introduction to Fourier Optics*.
17. G.B.Parrent and B.J.Tompson, eds., *The New Physical Optics Notebook* (SPIE, Bellingham, 1989)
18. M.F.Shikel and K.Fahrenschon, *Appl.Phys.Lett*, v.19,(1971) p.391
19. W.P.Blecha, L.T.Lipton, E.Wiener-Avner et al, *Optical Engeneering*, v.17, N4, (1978),p.p.371-384.

## Part III

### Photorefractive Crystal (PRC) Based Technology for Distortion Mitigation in Laser Beams

#### 1. Mitigation of phase distortions by means of one-way mitigation system with formation of pumping wave from the distorted signal

##### 1.1. Introduction

During some last years, the problems of formation of high-quality laser beams and compensation or correction of distortions resulting from propagation of such beams through inhomogeneous medium are of great interest. These problems are very significant in such important applications as imaging through turbulent atmosphere, laser location, transmission of laser beam through optical fibers, etc. The main goal of this paper is to present our last results in simulation of so-called one-way compensation system based on four-photon processing of distorted signal in nonlinear medium.

The first systems, used to correct the phase distortions, were based on so-called active techniques. In such a system, wave front of signal is changed by means of flexible adaptive mirrors<sup>1</sup> or holograms<sup>2-4</sup> before its propagation through inhomogeneous medium. A control of the signal is performed in such a manner to obtain required wave front of the signal after its way through the medium. Evidently, for optical signals with rather complicated wave fronts or for inhomogeneities that change in time, practical realization of such kind a system is very difficult or impossible.

Another way to solve the problem lies in application of so-called phase conjugation technique. In such a system, wave front of signal after its propagation through inhomogeneities is directed to special unit - phase-conjugating mirror (PCM) - which performs operation of phase conjugation of wave front of the signal. After that, conjugated signal is transmitted through the same path in the reverse direction and the initial wave front of the signal is reconstructed. In fact, very many nonlinear processes can be used to realize PCMs. However, the most promising units of such kind are usually based on degenerate three- ( $2\omega - \omega = \omega$ ) or four- ( $\omega + \omega - \omega = \omega$ ) photon processes in nonlinear medium<sup>5-9</sup>. Here  $\omega$  is frequency of the signal and some additional waves - pumping beams. These processes are thresholdless and enable one to conjugate ultrashort laser pulses with duration up to  $10^{-11}$ - $10^{-14}$  s<sup>10</sup>. Quantum efficiency of such PCMs depends on value of nonlinear susceptibility, length of nonlinear interaction, intensities of pumping beams and increases with increase of these parameters<sup>5-10, 16</sup>.

The most important characteristic of any mitigation system is quality of distortion compensation. This characteristic can be estimated, for example, through so-called overlapping integral<sup>15</sup>

$$H = \frac{\left| \int_0^{\infty} U_0(\vec{\rho}, z) U_{out}(\vec{\rho}, z) d\vec{\rho} \right|^2}{\int_0^{\infty} |U_0(\vec{\rho}, z)|^2 d\vec{\rho} \int_0^{\infty} |U_{out}(\vec{\rho}, z)|^2 d\vec{\rho}} \quad (1.1)$$

Here  $U_0$  and  $U_{out}$  are the amplitudes of the input (initial) signal and the output (reconstructed) field,  $\rho$  and  $z$  define position of each point in polar system of coordinates. Many investigations of  $H$  dependence on various characteristics of input signal, inhomogeneous medium, and PCM were performed<sup>5-15</sup>. It was shown that the most promising nonlinear materials for the practical realization of PCM are photo-refractive crystals (PRC). Unfortunately, all schemes of such kind are of so-called double-way character. That means that phase distortions resulting from the first propagation of signal through inhomogeneities can be compensated only after one more path of the conjugated signal through the same inhomogeneities. Limitations resulting from this specific feature of such schemes are most evident in the case with rather long path of the signal through inhomogeneities that change in time. In this case, the problem of mitigation of distortions can not be solved by such a manner. That is why so-called one-way compensation systems were proposed<sup>12-14</sup>. Unfortunately, up to now many problems of their practical realization and operation have not been investigated and solved.

One-way compensation system can be realized by different ways. For example, one can pass signal beam  $U_s$  with useful information and pumping beam  $U_{p1}$  with plane wave front through the same inhomogeneities (fig. 1.1). In case when these inhomogeneities are of "pure" phase character, one can subtract them from wave front of output wave  $U_s$  by means of four-beam interaction in PRC

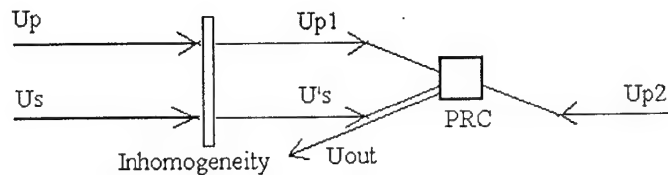


Fig.1.1 One-wave mitigation system with pumping wave  $U_{p1}$  formed by the same inhomogeneities from the special wave  $U_p$ .

$$U_{out} \approx (U_s \exp(i\phi))^* U_{p1} \exp(i\phi) U_{p2} \approx U_s. \quad (1.2)$$

Here  $\exp(i\phi)$  is the transmission function of inhomogeneities. It is easy to see that if the second pumping wave  $U_{p2}$  is plane, four-photon mixing of these beams in nonlinear medium gives rise to output signal without any distortions.

Unfortunately, a scheme of such kind always needs in special pumping wave  $U_{p1}$  transmitted through the same path as the signal. Obviously, it is not so convenient in many applications. However, in case with different spatial scales of useful signal and inhomogeneities, it is possible to use another way. Processing some part of distorted signal<sup>12</sup>, one can form pumping beam with needed shape of wave front. To do this, the signal information must be previously removed from this part of distorted signal by special spatial filter (fig.1.2) while information about all inhomogeneities must be retain. After that, the distorted signal, the pumping wave prepared by this way, and one more pumping wave with plane wave front must be mixed in PRC.

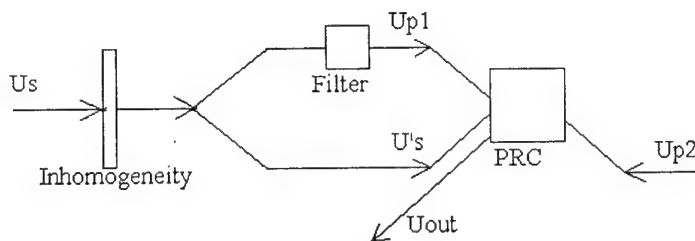


Fig.1.2 One-wave mitigation system with formation of pumping  $U_{p1}$  by spatial filtration of distorted signal  $U_s$ .

Two main factors can influence on quality of compensation of phase distortions. The first factor is connected with accuracy of phase conjugation and is inherent to all versions of such a system. This procedure is not ideal and its accuracy is determined by PCM transfer function. Efficiency of this nonlinear process depends on pumping intensities, the nonlinearity, the length of nonlinear interaction, etc.<sup>10</sup>. At the same time, self-action and stimulated scattering as well as limited angular aperture of PCM will decrease quality of conjugation of input signal. The second factor is inherent to the version of one-way mitigation system with spatial filtration of the distorted signal. Removing of a part of signal information and retaining of a part of information about inhomogeneities result in decrease of quality of distortion compensation. The best quality must correspond to the case when shape of wave front of formed pumping beam coincides with shape of wave front of special plane pumping beam distorted by inhomogeneities. However, because spatial spectra of transmitted information and inhomogeneities overlap, it is not possible to form such ideal pumping.

A possibility of distortion mitigation by such a scheme can be illustrated by a simple example relating to the case with discrete spectra of signal and inhomogeneities. Let us suppose that transmitted informative signal  $U_s$  is given in the form of one-dimensional harmonic phase grating

$$U_s = U_0 \exp(ia \cos(\alpha x)) = U_0 \sum_{-\infty}^{\infty} i^m J_m(a) \exp(im\alpha x). \quad (1.3)$$

Here  $U_0$  is the amplitude of the signal,  $a$  and  $x$  represent the depth and spatial frequency of the useful phase modulation. Let us suppose that phase distortions can be described as similar phase grating with the amplitude  $b$

and spatial frequency  $\beta$ . That means that after propagation through the inhomogeneous medium, the useful signal multiply by factor  $\exp(ib\cos(\beta x))$  and can be represented as

$$U'_s = \sum_{-\infty}^{\infty} i^{m+n} J_m(a) J_n(b) \exp(i(m\alpha + n\beta)x). \quad (1.4)$$

Therefore, its spatial spectrum  $U'_s$  which is shown in fig.1.3 can be written in the form

$$U'_s(\kappa) = \sum_{k,p=-\infty}^{\infty} i^{k+p} J_k(a) J_p(b) \delta(k\alpha + p\beta + \kappa). \quad (1.5)$$

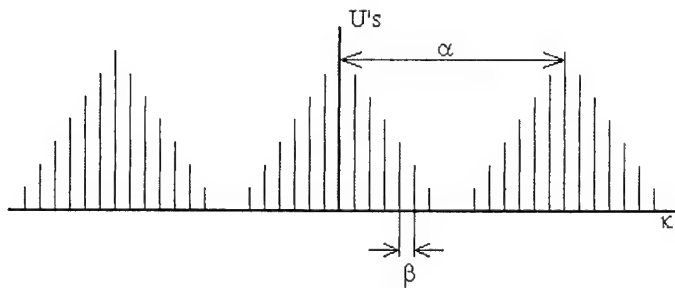


Fig.1.3 Spatial spectrum of the signal  $U'_s$  distorted by harmonic phase grating.

Ideal pumping wave front (see above) must include all spectral components with  $k=k_0$ . Here  $J_{k_0}(a) = \max J_k(a)$ ,  $k = 0, \pm 1, \pm 2, \dots$ . Corresponding spectrum of pumping is shown in fig.1.4. Quality of mitigation will decrease by two different reasons. The first reason results from presence of some pumping spectral components with  $k \neq k_0$  and the second one follows from absence of some components with  $k=k_0$ .

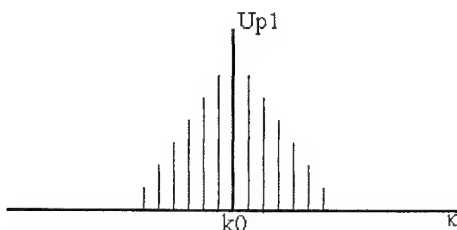


Fig.1.4 Spatial spectrum of the pumping wave  $U_{p1}$  formed by spatial filtration of the distorted signal  $U'_s$ .

This situation is typical for any real conditions and must be simulated in calculations. Another problem results from random behavior of real inhomogeneities which are of interest. That means that stochastic description must be used to optimize one-way mitigation system.

### 1.2. Description of the model

Our theoretical model of proposed one-way mitigation system is based on a step-by-step analytical description of the input image transformation. That means that in our model, we consequently consider the transformation of the input image after all parts of its total way through the homogeneous region of atmosphere, the turbulent region, the filter of spatial frequencies for the channel of the pumping wave formation, the PCM, etc. (fig.1.5). On each such a step we use the paraxial approximation.

For example, after the way through the homogeneous region of atmosphere with the length  $\Delta z$ , spatial spectrum of the signal  $U(\kappa)$  transforms as

$$U(\kappa, z + \Delta z) = U(\kappa, z) \exp\left(-\frac{i\kappa^2}{2k} \Delta z\right). \quad (1.6)$$

Here  $k$  and  $\kappa$  are the magnitude and the transverse projection of the wave vector of the signal. We consider only two-dimensional case, but the model can be easily generalized to three-dimensional case if  $x$  and  $y$  coordinates are independent.

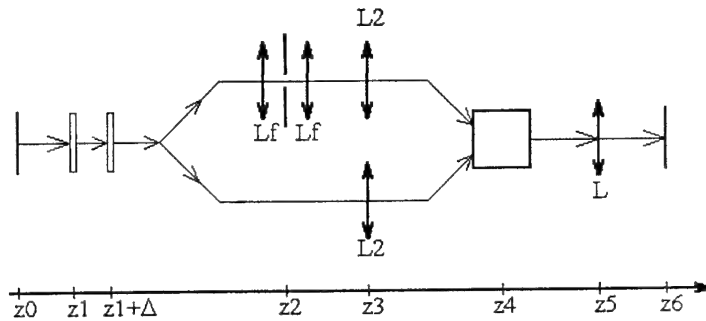


Fig. 1.5. Block-diagram of one-way mitigation system:  $L_f$  - lenses of spatial filter;  $L_{1,2}$  - lenses focusing the signal and pumping into PCM;  $L$  - lens focusing the restored signal on the plane  $z_6$ .

We simulate turbulent region of atmosphere by a set of  $n$  thin random phase screens with transmission functions  $\exp[i\phi_n(r)]$ . Here  $\phi_n$  is the random phase shift of the signal after its path through the  $n$ -th screen. Therefore, we describe the input signal transformation by each the screen as

$$U'(r, z_n) = U(r, z_n) \exp(i\phi_n(r)). \quad (1.7)$$

Here  $z_n$  is the longitudinal coordinate of the  $n$ -th screen. Expression (1.7) is equivalent to transformation of spatial spectrum of the input signal which is given by

$$U'(\kappa, z_n) = \int_{-\infty}^{\infty} U(\kappa', z_n) T_n(\kappa - \kappa') d\kappa' \quad (1.8)$$

Here  $T_n(\kappa - \kappa')$  is the Fourier image of the transmission function  $\exp[i\phi_n(r)]$ . We consider the way of the signal between each pair of phase screens as homogenous region of atmosphere and described the input signal transformation on these parts of the total way by expression which is similar to (1.6). Such the model is reasonable if distance between the screens ( $\Delta$ ) are more than the correlation length in  $z$  direction. This assumption enables us to consider the screens as independent.

We consider the filter of spatial frequencies to be composed of two lenses with the same focal length  $f_f$  and a pin-hole placed in the middle of the distance  $2f_f$  between these lenses. The filter transforms spatial spectrum of the signal from the input focal plane  $z_{-f}$  of the first lens to the output focal plane  $z_{+f}$  of the second lens in accordance with expression

$$U'(\kappa, z_{+f}) = \frac{t_f}{\pi k} U(\kappa, z_{-f}) t_f \left( -\frac{f_f \kappa}{k} \right). \quad (1.9)$$

Here  $t_f$  is transmission function of the pin-hole. Further, the planes  $z_{-n}$  and  $z_{=n}$  are considered as a plane  $z_2$  (fig. 1.5). It means optical ways of the signal and pumping are the same.

The PCM is assumed to be an ideal four-photon converter of the input fields in relation to its spatial resolution and the speed of response. The second pumping wave is assumed to be plane. In this case, the PCM performs the convolution of spatial spectra of the input signal  $U_s$  and formed pumping  $U_p$

$$U'(\kappa, z) = K \int_{-\infty}^{\infty} U_p(\kappa', z) U_s^*(\kappa' - \kappa, z) d\kappa' \quad (1.10)$$

Here  $K$  represents energy efficiency of the PCM.

An additional optical system combined of the lenses  $L_1$  and  $L_2$  with the same focal length  $f$  and the lens  $L$  with the focal length  $f_2$  is used to focus the pumping wave and the distorted image into PCM and to form the output signal. Expression for spatial spectrum of the output (restored) signal can be obtained in the form

$$U_{out}(r, z_6) = C_{int} \int_{-\infty}^{\infty} \int d\kappa_{p1} d\kappa_{p2} d\kappa_{p3} d\kappa_{s1} d\kappa_{s2} d\kappa_{s3} d\kappa_0 d\tilde{\kappa} d\kappa U_0(\kappa_{p1}) U_0^*(\kappa_{s1}) \\ t_f(-\kappa_{p3}) T_1(\kappa_{p2} - \kappa_{p1}) T_2(\kappa_{p3} - \kappa_{p2}) T_1^*(\kappa_{s2} - \kappa_{s1}) T_2^*(\kappa_{s3} - \kappa_{s2}) \exp(i\kappa r) \\ \exp \left\{ \frac{i}{2k} \left[ -\kappa_{p1}^2 z_1 - \kappa_{p2}^2 \Delta - \kappa_{p3}^2 (z_3 - z_1 - \Delta) - \kappa_0^2 (z_4 - z_3) + \right. \right. \\ \left. \left. + (\kappa_0 - \kappa_{p3})^2 f + \kappa_{s1}^2 z_1 + \kappa_{s2}^2 \Delta + \kappa_{s3}^2 (z_3 - z_1 - \Delta) + (\kappa_0 - \tilde{\kappa})^2 (z_4 - z_3) - \right. \right. \\ \left. \left. - (\kappa_0 - \tilde{\kappa} - \kappa_{s3})^2 f - \tilde{\kappa}^2 (z_5 - z_4) - \kappa^2 (z_6 - z_5) + (\kappa - \tilde{\kappa})^2 f_2 \right] \right\} \quad (1.11)$$

Here  $U_0$  represents spatial spectrum of the transmitted image,  $C$  is the constant which depends on  $K$ ,  $k$ ,  $f$ ,  $f_2$ . Expression (1.11) relates to the model which includes only two random phase screens but any number of such phase screens can be included in (1.11) with ease. Furthermore, we suppose that  $\phi_{1,2}(r)$  corresponds to the isotropic random process with Gaussian statistics. We suppose the distance between the screens are more than the correlation length along  $z$  direction (see above). This assumption enables us to simplify expression (1.11) by means of its averaging and usage of relation

$$\langle T_1(\kappa_1) T_2(\kappa_2) T_1^*(\kappa_3) T_2^*(\kappa_4) \rangle = S_1(\kappa_1) S_2(\kappa_2) \delta(\kappa_1 - \kappa_3) \delta(\kappa_2 - \kappa_4). \quad (1.12)$$

Here

$$S_{1,2}(\kappa) = \langle |T_{1,2}(\kappa)|^2 \rangle. \quad (1.13)$$

Finally, we find expression for the mean value of the output signal in the form

$$\langle U \rangle = \langle U_{out}(r, z_6) \rangle = C \int_{-\infty}^{\infty} \int d\tilde{\kappa} d\eta_1 d\eta_2 d\kappa_0 d\kappa \\ S_1(\eta_1) S_2(\eta_2) t_f(-(\kappa_0 + \eta_1 + \eta_2)) \\ U_0(\kappa_0) U_0^*(\kappa_0 - \beta \tilde{\kappa}) \exp(i\kappa r) \\ \exp \left\{ \frac{i}{k} \left[ \frac{A_s \beta \kappa^2}{2} - A_s \tilde{\kappa} \kappa_0 - A_{n1} \tilde{\kappa} \eta_1 - A_{n2} \tilde{\kappa} \eta_2 \right] \right\} \\ \exp \left\{ \frac{i}{2k} \left[ (\kappa - \tilde{\kappa})^2 f_2 - \tilde{\kappa}^2 (z_5 - z_4) - \kappa^2 (z_6 - z_5) \right] \right\} \quad (1.14)$$

Here  $\beta$  is the scale constant of the lens system  $L_{1,2}$ ,

$$A_s = z_4 - z_3 + \left( 1 - \frac{z_4 - z_3}{f} \right) z_3 = z_4 - z_3 + \beta z_3, \quad (1.15)$$

$$A_{n1} = z_4 - z_3 + \beta(z_3 - z_1), \quad (1.16)$$

$$A_{n2} = z_4 - z_3 + \beta(z_3 - z_1 - \Delta). \quad (1.17)$$

To analyze (1.14), we express spectral density  $S(\kappa)$  in the terms of the correlation function  $B_{12}$  of the phase  $\phi$

$$S(\kappa) = \int_{-\infty}^{\infty} \exp(-i\kappa r - \sigma^2 + B_{12}(r)) dr, \quad (1.18)$$

$$\sigma^2 = B_{12}(0). \quad (1.19)$$

To find variance of the output signal we have to average expression

$$\begin{aligned} \langle T_1(\kappa_1) T_1^*(\kappa_2) T_1^*(\kappa_3) T_1(\kappa_4) \rangle = & 2\pi \delta(\kappa_1 - \kappa_2 - \kappa_3 + \kappa_4) \int_{-\infty}^{\infty} dR_2 dR_3 dR_4 \exp(i\kappa_2 R_2 + i\kappa_3 R_3 - i\kappa_4 R_4) \\ & \exp\{B_{12}(R_2) + B_{12}(R_3) - B_{12}(R_4) + B_{12}(R_4 - R_2) + B_{12}(R_4 - R_3) - B_{12}(R_3 - R_2)\} \end{aligned} \quad (1.20)$$

Expressions (1.11) and (1.20) enables us to find variance of the output signal

$$D = \langle U_{out} U_{out}^* \rangle - \langle U_{out} \rangle \langle U_{out}^* \rangle. \quad (1.21)$$

To calculate the output field characteristics in analytical way, we suppose the function  $B_{12}(r)$  to be Gaussian and expand it into a series

$$B_{12}(r_1 - r_2) = \sigma^2 \left( 1 - \frac{(r_1 - r_2)^2}{R_n^2} \right). \quad (1.22)$$

Here  $R$  is the correlation radius. In this approximation, the spectral density  $S$  is a Gaussian, too,

$$S(\eta) = \sqrt{\pi} R_n \exp\left(-\frac{\eta^2 R_n^2}{4}\right). \quad (1.23)$$

According to (1.22) expression (1.20) is equal to

$$\begin{aligned} \langle T_1(\kappa_1) T_1^*(\kappa_2) T_1^*(\kappa_3) T_1(\kappa_4) \rangle = & \\ = S_1(\kappa_1) \delta(\kappa_2 - \kappa_1) \delta(\kappa_3 - \kappa_1) \delta(\kappa_4 - \kappa_1). & \end{aligned} \quad (1.24)$$

Transmission function of the pin-hole is supposed to be a Gaussian, too,

$$t_f(\kappa) = \exp\left(-\frac{\kappa^2}{t_0^2}\right), \quad (1.25)$$

$$t_0 = \frac{kc}{f_f}, \quad (1.26)$$

where  $c$  is the pin-hole radius.

We describe the input signal in the form of two shifted Gaussian spots and suppose the first spot is located in the middle of the field of view and the second spot is shifted in relation to the first one in distance  $r_2$

$$U_0(\kappa) = A_1 \exp\left(-\frac{\kappa^2 R_{01}^2}{4}\right) + A_2 \exp\left(-\frac{\kappa^2 R_{02}^2}{4}\right) \exp(-i\kappa r_2). \quad (1.27)$$

Here  $A_{1,2}$  and  $R_{01,02}$  are their amplitudes and radii. Such shape of a signal enable us to investigate possibility of image reconstruction over the field of view.

Results (1.14), (1.21), (1.22), (1.25) and (1.27) enable us to obtain mean value and variance of the output signal in analytical form. Because final expressions are rather unwieldy to be written here, they will be represented here only in a graphical form (fig.1.6-fig.1.15).

### 1.3. Results of calculations

At the first glance, it seems there are too many free parameters to optimize our system. However, it is not right and we can choose the values of some part of them using a very simple qualitative reasoning. Let us

consider the mitigation system with only one phase screen and plane pumping wave passing through the same inhomogeneities as the informative signal. In this case, spatial spectrum of "ideal" output signal will be defined by

$$\langle U_{out}(\kappa, z_4) \rangle = U_0^*(-\beta k) B(-A_n \kappa / k) \exp(i A_s \beta \kappa^2 / 2k). \quad (1.28)$$

Here  $B$  is the Fourier transform of  $S$  (1.18), that is a correlation function of  $\exp(i\phi_n)$ . It follows from expression (1.28) the case of ideal reconstruction can be realized only if both lenses  $L_{1,2}$  are focused onto the phase screen plane. That means the distortions in the PCM plane are of "pure" phase character. In this case,  $B(0)=1$  and the factor  $\exp(i A_s \beta \kappa^2 / 2k)$  can be corrected by symmetrical adjustment of the system

$$\begin{aligned} z_6 - z_5 &= z_3, \\ z_5 - z_4 &= z_4 - z_3. \end{aligned} \quad (1.29)$$

It is easy to see that there is an similar requirement for the system with two phase screens and the plane of optimal focusing lies between the screens. Its position is determined by relationship between correlation radii of phase distortions<sup>11</sup>. In the case when the radii are the same, the plane of optimal focusing is placed in the middle of interval between the screens. In fact, our model parameters, which should be optimized, are only characteristics of informative signal, inhomogeneities, spatial filter, and position of focal planes of lenses L. Therefore, the system optimization means determination of optimal relationships between them.

To check up the ability of our system to correct phase distortions, we performed numerical calculations of analytical expressions for mean value and variance of output signal. Firstly, it was necessary to find out allowable relationships between spatial scales of informative signal, inhomogeneities, and the width of spatial filter that enables us to reconstruct the image. For these relationships, spatial distribution of mean value of the output signal must coincide with initial distribution of the informative signal. Solving this problem, we considered some different combinations with one ( $A_1$  or  $A_2 = 0$ ) or two input beams and one or two phase screens. The lenses L were focused onto the plane of the phase screen or onto the middle plane between two identical phase screens. The case of one phase screen was simulated by the case of two phase screens by putting the distance between them equal zero. So, in the case of one phase screen, effective correlation radius was equal to  $R_0/\sqrt{2}$ .

To filter the signal spectral components and to retain the spectral components of the inhomogeneities, one needs to satisfy some requirements to their spatial characteristics. Therefore, one can expect the mitigation of distortions in the range

$$\frac{1}{R_n} < t_0 < \frac{1}{R_0}. \quad (1.30)$$

The left part of inequality (1.30) corresponds to passing of components of spatial spectrum of the distortions through the spatial filter. In the case of its violation, distortions of the output field will be exactly of phase character because the formed pumping wave is almost plane. At the same time, the random phase distortions do not almost subtracted and the variance of the output field must be very large. That means that normalized variance of the output field is a good criterion of efficiency of this subtraction. The right part of inequality (1.30) corresponds to filtering of some components of spatial spectrum of the informative signal by the spatial filter. At the same time, random phase distortions are subtracted and the variance of the output signal must be small. In the case of its violation, mean value of the output signal will be distorted because amplitude profile of the formed pumping wave will repeat the amplitude profile of the informative signal and the last will be squared. It is very important that these nonlinear distortions can not be corrected by any routine optical system. For the case with Gaussian beam, such distortions result to change of its radius. Therefore, full width of half maximum (FWHM) of mean value of the output signal is a good criterion to estimate nonlinear distortions. Our calculation enables us to determine an effective operating range of one-way mitigation system that provides the output signal of both minimal nonlinear distortions and minimal variance.

Results of our numerical calculations of the output beam FWHM and its variance  $D$  versus  $R_n$  and the width of the spatial filter  $t_0$  (1.26), are shown in fig.1.6 and fig.1.7. The variance is normalized to the unit magnitude. The calculation results are in full accordance with the above discussion of inequality (1.30). It is easy to see that in the case when the informative components of the input signal spectrum are not filtered ( $R_n t_0 \gg 1$ ), the output signal is really proportional to the squared informative signal and the limit value of its FWHM is equal to  $\sqrt{2} R_0$ . The same value can be obtained in analytical way from (1.14) for another case when  $R_n \ll R_0$ . However, in the case when only the right part of (1.30) is violated i.e.  $t_0 < 1/R_0$  and  $t_0 < 1/R_n$ , the variance  $D$  is small

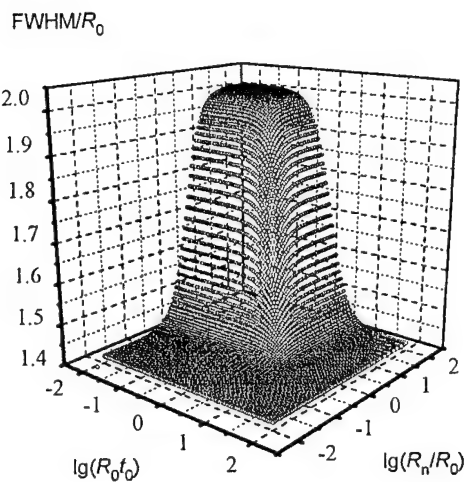


Fig.1.6. FWHM versus  $R_n$  and  $t_0$ ;  $R_0=1$  cm.

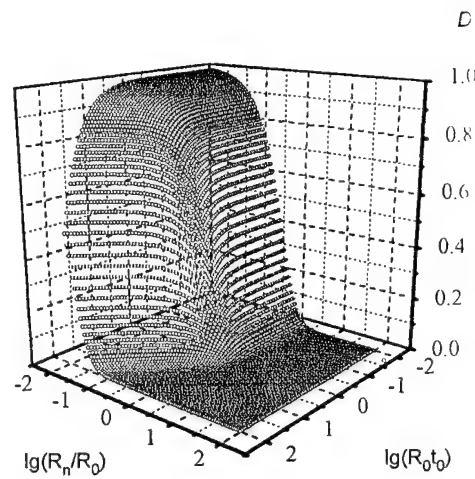


Fig.1.7.  $D$  versus  $R_n$  and  $t_0$ ;  $R_0=1$  cm.

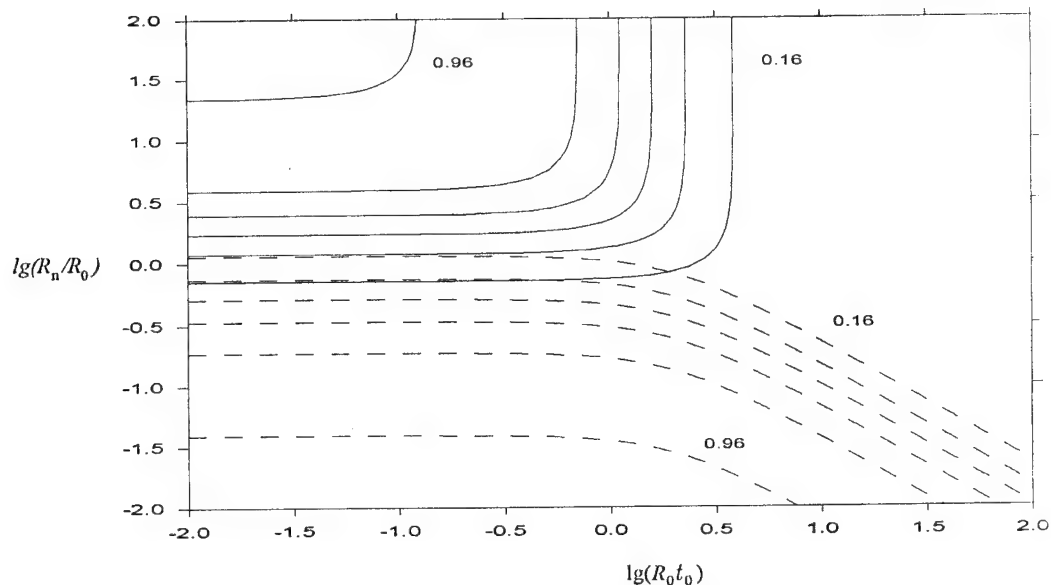


Fig.1.8. Isolines of  $F$  (solid lines) and  $D$  (dashed lines) plotted on  $(R_n/R_0 - R_0 t_0)$  plane through 0.16.

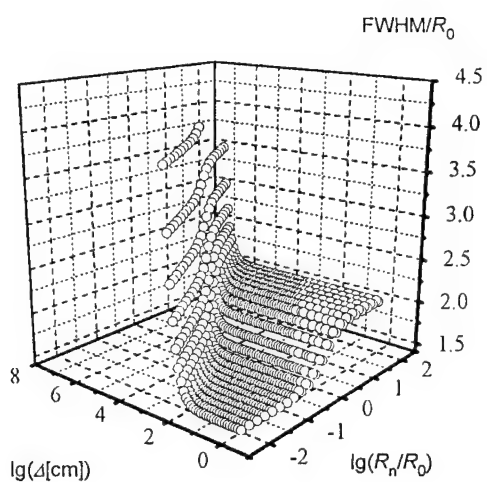


Fig.1.9. FWHM versus  $R_n$  and  $\Delta$ :  $R_0=1$  cm,  $R_0 t_0=0.01$ .

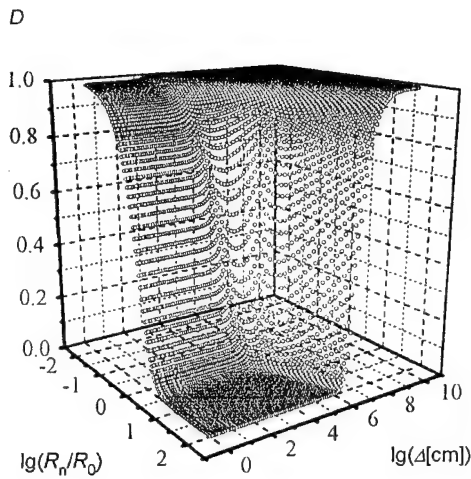


Fig.1.10.  $D$  versus  $R_n$  and  $\Delta$ :  $R_0=1$  cm,  $R_0 t_0=0.01$ .

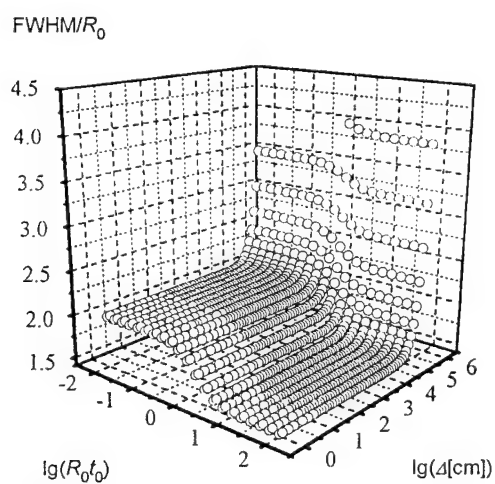


Fig.1.11. FWHM versus  $t_0$  and  $\Delta$ :  $R_0=1$  cm,  $R_n/R_0=10$ .

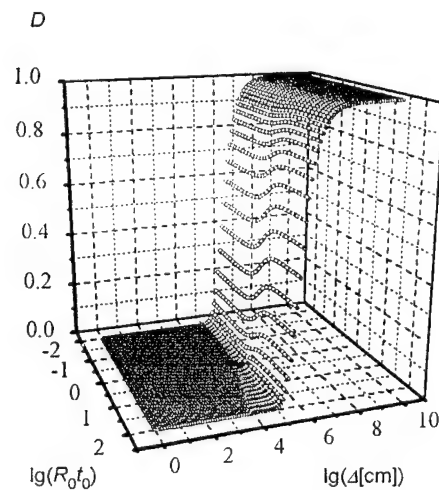


Fig.1.12.  $D$  versus  $t_0$  and  $\Delta$ :  $R_0=1$  cm,  $R_n/R_0=10$ .

$\text{FWHM}/R_0$

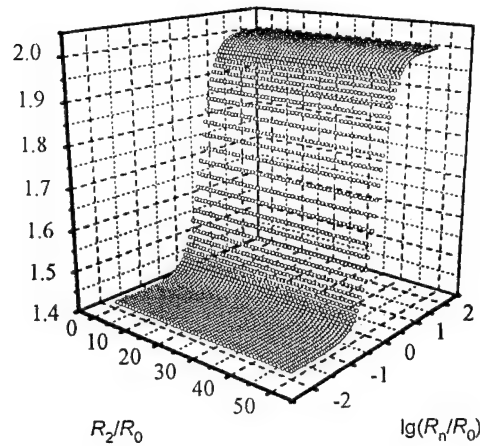


Fig.1.13. FWHM versus  $R_n$  and  $R_2$ ;  $R_0=1$  cm,  $R_0 t_0=0.01$ .

$D$

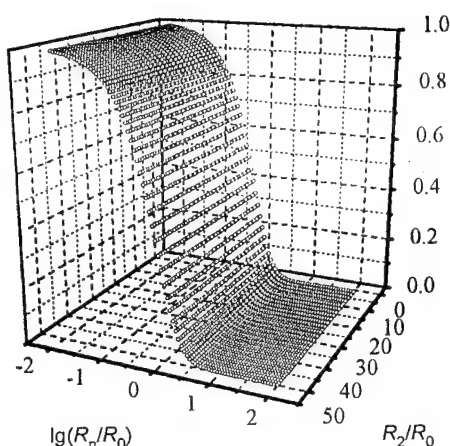


Fig.1.14.  $D$  versus  $R_n$  and  $R_2$ ;  $R_0=1$  cm,  $R_0 t_0=0.01$ .

$\langle U_{\text{out}} \rangle$  [a.e.]

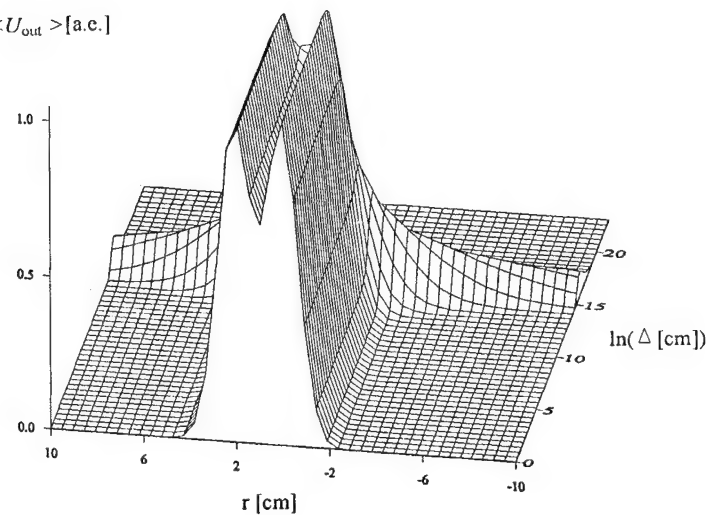


Fig.1.15. Distribution of  $\langle U_{\text{out}} \rangle$  versus  $r$  and  $\Delta$  for the case with two input Gaussian beams.

(see fig. 1.7), too, due to rather large spatial scale of inhomogeneities. To determine the effective operating range of the mitigation system, we calculated the isolines (fig. 1.8) of  $F = [(FWHM - \sqrt{2}R_0) / (2R_0 - \sqrt{2}R_0)]$  (solid lines) and normalized  $D$  (dashed lines) which are plotted on the  $\lg(R_n/R_0) - \lg(t_0 R_0)$  plane. The step between consecutive two isolines is equal to 0.16. One can see that in the case of  $F > 0.32$ , the variance  $D < 0.16$ . Therefore, the major limitation on effective operating range of our system is determined by distortions of the mean value of the output signal.

Fig. 1.6-1.8 refer to the case of distortions of pure phase character, that is, to the case of precise focusing of the lens system onto the plane of two coincident phase screens. For extended atmospheric path, such a case can not be realized. That is why we calculated FWHM and D for the case with two identical phase screens separated by distance  $\Delta$  simulating the length of atmospheric path. Under conditions of optimal focusing of the lens system onto the middle plane (see above) and transmitted beam radius 1 cm, results of our calculations are shown in fig. 1.9-1.12. Allowable value of  $\Delta$  has been found to be about  $10^5-10^6$  cm that is long enough for the most part of practical important applications. The major limitation on effective operating range of mitigation system is determined as before by distortions of the mean value of the output signal.

Formation of spatial spectrum of the pumping wave is necessary attended with its angular divergence. This specific feature of the mitigation system can result in dependence of the PCM characteristics on transverse coordinates<sup>11</sup>. That is why we calculated FWHM and D of the output field in the case of the one input Gaussian beam ( $A_1 = 0$ ) shifted by  $R_2$  in transverse direction. Calculation results are shown in fig. 1.13 and fig. 1.14. It is easy to see that quality of mitigation does not practically depend on initial position  $R_2$  of the input beam.

Calculating the case of two input Gaussian beams ( $A_1 = A_2$ ), we checked a possibility to mitigate distortions of more complicated transmitted image. The input beams were supposed to be originally resolved by the Rayleigh criterion. Averaged distribution of the output field is shown in fig. 1.15. In this case, criterion of small D is good to the same region and the output beams can be resolved even better than the input ones due to some nonlinear distortions (see above). The Rayleigh criterion can be violated only for very large  $\Delta \sim 10^5-10^6$  cm, that is, for very long atmospheric way.

In a real PCM with the PRC length l, nonlinear interaction should be considered taking into account phase mismatch  $\delta$  of wave-vectors of interaction waves along z-axis. The spatial spectra of the output field is determined by the expression

$$U'(\kappa, z) = K \int_{-l/2}^{l/2} \int_{-\infty}^{\infty} U_p(\kappa', z') U_s^*(\kappa' - \kappa, z') \exp(i\delta z') dz' d\kappa', \quad (1.31)$$

where in paraxial approximation  $\delta = (2\kappa^2 - \kappa\kappa')/k$ . One should integrate expression for the output field  $U_{out}$  obtained for the ideal case ( $l = 0$ ) over the PRC length because parameters  $A_{n,s}$  and  $\beta$  should be replaced by the following way

$$A_n \Rightarrow A_n + z', \quad \beta \Rightarrow \beta - z'/f, \quad A_s \Rightarrow A_s + z'(1 + 1/\beta).$$

This is an exact way to take into account the real PCM length. However, much more simple way of estimation of such kind lies in calculation of an equivalent problem. One can calculate FWHM and D for the case when the focusing lens system is mismatched for a distance about l. A typical value of l is about only 1 cm. It is much less than diffraction length of the input signal beam with  $R_0 = 1$  cm and can not considerably influence on the obtained results.

#### 1.4. Conclusions

1. The model of one-way mitigation system, based on nonlinear interaction of distorted informative optical signal and pumping wave formed from a part of the distorted signal has been developed.
2. A criterion of successful mitigation of phase distortions have been formulated.
3. Full width of half maximum of mean value of the output field and its variance have been calculated.
4. An effective operating range of the mitigation system has been determined and optimized.
5. It has been shown the optimized mitigation system is good for many practical important cases.

#### 1.5. Literature Cited

1. Adaptive Optics, JOSA **67**, N3 (1977).
2. Jack D. Gaskill. J. Opt. Soc. Am. **58**, 600 (1968).
3. J.W. Goodman et al. Appl. Phys. Lett. **8**, 311 (1966).
4. C.O. Reynolds, T.J. Skinner. J. Opt. Soc. Am. **54**, 1302 (1964).
5. B.I. Stepanov, E.V. Ivakin, A.S. Rubanov. DAN USSR **196**, 567 (1971) (in Russian).
6. D.M. Bloom, G.C. Bjorkland. Appl. Phys. Lett. **31**, 592 (1977).

7. E.S. Voronin et al. ICONO'78 Proceedings, 243 (1978) (in Russian).
8. E.S. Voronin et al. Kvantovaya Elektronika **6**, 2009 (1979) (in Russian).
9. S.M. Jensen, R.W. Hellwarth. Appl. Phys. Lett. **32**, 166 (1978).
10. V.V. Ivakhnik et al. Kvantovaya Elektronika **7**, 898 (1981) (in Russian).
11. E.S. Voronin, V.M. Petnikova, V.V. Shuvalov. Kvantovaya Elektronika **8**, 917 (1981) (in Russian).
12. J.An. Jeung et al. Opt. Lett. **4**, 42 (1979).
13. E.V. Ivakin, I.N. Petrovichev, A.S. Rubanov. In "Optical methods of information processing", Minsk, Nauka i Tekhnika, 1978, 124 (in Russian).
14. V.V. Ivakhnik et al. Kvantovaya Elektronika **7**, 653 (1980) (in Russian).
15. B.Y. Zel'dovich, V.V. Shkunov. Kvantovaya Elektronika **4**, 2353 (1977) (in Russian).
16. S.G. Odulov et al. UFN **23**, 562 (1978) (in Russian).
17. V.V. Ivakhnik et al. Proceedings of the conference "Optical image formation and methods of its correction", Mogilev, 1979, 125 (in Russian).
18. E.S. Voronin et al. Kvantovaya Elektronika **7**, 543 (1980) (in Russian).
19. R.K. Jain, M.B. Klein, R.C. Zind. Opt. Lett. **4**, 341 (1979).
20. D. Fekete, J.An. Jeung, A. Jariv. Opt. Lett. **5**, 51 (1980).
21. S.M. Jensen, R.W. Hellwarth. Appl. Phys. Lett. **33**, 404 (1978).
22. R.W. Hellwarth. IEEE QE-15, 101 (1979).
23. V.V. Ivakhnik, V.M. Petnikova, V.V. Shuvalov. ICONO'80 Proceedings, 137 (in Russian).
24. K.S. Bjorkholm, M.S. Danielmeyer. Appl. Phys. Lett. **15**, 171 (1969).
25. I.S. Itskhoki, K.S. Seregin. Kvantovaya Elektronika **7**, 900 (1980) (in Russian).
26. S.A. Akhmanov, V.G. Dmitriev. Optika i Spektroskopiya **33**, 156 (1972) (in Russian).
27. S.A. Akhmanov, A.S. Chirkin. Introduction in Statistical Optics, M., 1985 (in Russian).
28. D. Goodman. Introduction in Fourier Optics, 1970 (in Russian).

## 2. Dynamic distortion suppression by phase-conjugation systems based on inertial photorefractive nonlinearity

### 2.1. Introduction

During some last years, the problem of phase distortion mitigation by means of systems based on photorefractive crystals (PRC) is of great interest<sup>1</sup>. The main reason of such interest is a possibility to realize high-efficient nonlinear interaction using very low intensity of pumping beams<sup>2</sup>. On the other hand, the PRC nonlinear response is inertial and nonlocal<sup>3</sup>. These specific features enable one to develop some new and very promising techniques to suppress the dynamic distortions. In conventional version of mitigation system<sup>4</sup>, nonlinear medium is used only as a phase-conjugating (PC) mirror. Therefore, to compensate the phase distortions, one needs to use the second pass of conjugated signal through the same inhomogeneities. This pass greatly narrows down the field of possible applications of such a system. So called "one-way" mitigation systems<sup>5</sup> allow one to except the second pass of restored beam through the inhomogeneities. In systems of such kind, wave front of the first beam - the signal - is modulated by both the useful information and phase distortions. The second one - the pumping - is phase modulated too, but the shape of its wave-front results only from the phase distortions. To restore the initial information, one must simply subtract the wave front of pumping from the signal one by means of nonlinear interaction in PRC. To form the needed shape of wave front of pumping, one can use an additional plane wave transmitted through the same path<sup>6</sup>. Another possible way to solve this problem lies in spatial filtration of the distorted signal<sup>7</sup>. Implementation of inertial PRC gives us the new possibility to realize a crucially new type of one-way system. Such a system is based on averaging of dynamic distortions, that is, the nonlinear medium is used as a time averaging filter. Authors of reference<sup>8</sup> were the first who suggested and realized such technique and published some preliminary experimental results. The most promising field of applications of such system relates to problems connected with transmission of optical information through turbulent atmosphere.

The main goal of our paper is to present our last results in computer simulation of dynamic distortion suppression by the one-way system based on nonlinear interaction in photorefractive crystals.

### 2.2. The model

We took the conventional set of material equations<sup>3</sup> as a basis of our model. Using this set of equations, we obtained all analytical steady-state solutions. To compute dynamics of all the processes, we used the simplified<sup>9</sup> version of the set

$$\begin{cases} \frac{\partial E_x}{\partial x} = 4\pi\rho/\epsilon, \\ \frac{\partial j}{\partial x} = -\frac{\partial \rho}{\partial x}, \\ j = e\mu(n_d + n_e)(E_0 + E_{xc}) + \mu k_B T \frac{\partial n_e}{\partial x}, \\ \frac{\partial n_e}{\partial x} = \alpha I - \alpha_r n_e + \frac{1}{e} \frac{\partial j}{\partial x}. \end{cases} \quad (2.1)$$

Here  $\epsilon$  and  $T$  are the static dielectric constant and the temperature of PRC,  $e$  and  $\mu$  are the charge and the mobility of free carriers,  $k_B$  is the Boltzmann constant. Solution of (2.1) remains all specific features of dynamics of spatial distributions of the electric field  $E_{xc}$  and of the charge  $\rho$  and the current  $j$  densities. We supposed that the parameters  $\alpha$  and  $\alpha_r$  representing photogeneration and recombination of free carriers are the constants, that is, they do not depend on the dark  $n_d$  and photoinduced  $n_e$  densities of free carriers. We described the external static electric field applied to PRC by  $E_0$ . So, we took into account both drift and diffusion components of  $j$ .

The set (2.1) and the conventional wave equation for the amplitude  $A$  of light field with wave vector  $k$

$$2ik \frac{\partial A}{\partial z} = \Delta_\perp A + 2k^2 \frac{\delta n}{n} A \quad (2.2)$$

gave us the complete self-consistent problem. Here,  $n$  and  $\delta n$  are the linear and nonlinear parts of the refractive index. We calculated the last term by means of well-known electrooptic equations<sup>3</sup> and solution of (2.1). To simulate the problem numerically, we represented PRC as a set of thin nonlinear layers placed consequently along  $z$ -axis. We supposed that inside each layer, all functions, including the beam intensity  $I$ , depend only on the transverse coordinate  $x$ . We took into account all changes along  $z$ -axis by means of computing (2.2). We assumed that both boundary and initial conditions correspond to the system "switching on" at the moment  $t=0$  and that both the interacting beams are symmetrically directed onto the first layer. For each moment  $t$ , we computed (2.2) using the fast Fourier transformation. Then, we made the step in time and calculated  $\delta n$  as a result of each layer evolution to the new steady-state distribution of all the parameters listed above. In this procedure, we used all initial conditions from the previous time moment. So, we solved this self-consistent problem by step-by-step technique.

To simulate four-beam interaction, we modified our numerical scheme. We took into account only transmitting gratings, that is, we simulated the case with non-coherent or orthogonal polarized pumping beams. This assumption enabled us to speed up the calculation thanks to decrease of the number of required nonlinear layers. The main specific feature of our numerical scheme for this geometry was the following. For the stage of propagation, using inertia of PRC, we consequently simulated the pass of all the beams along  $z$ -axis in direct and reverse directions. Then we computed the nonlinear part  $\delta n$ . We thoroughly checked accuracy of our numerical scheme by changing the value of steps of the grids in time and space.

We described the phase distortions arising from the atmospheric turbulence as some additional phase modulation of wave front of the signal on PRC's input plane (subscript "in") according to

$$\delta\varphi^{in} = A_s \sin(k_s x) + A_n \sin(k_n x - \Omega t). \quad (2.3)$$

Here, the first item with the amplitude  $A_s$  at the spatial frequency  $k_s$  represents the useful information, and the second one with  $A_n$  and  $k_n$  describes the dynamic phase distortions at the atmospheric turbulence frequency  $\Omega$ . We estimated the mitigation quality as the root-mean-square deviation of the restored beam's phase wave front (subscript "out") from the initial information

$$\beta^{out} = \left\langle \left( \delta\varphi^{out} - A_s \sin(k_s x) \right)^2 \right\rangle^{1/2}. \quad (2.4)$$

The amplitude distortions were simulated as an additional amplitude noise, that is, for the optical field in PRC's input plane, we used the expression

$$E^{in} = E^{signal} + E_n \sin(k_n x). \quad (2.5)$$

Here, the first item represents the useful signal and the second one with the spatial  $k_n$  and temporal  $\Omega$  frequencies describes the amplitude dynamic distortions. In the four-beam geometry, the input and output planes of the mitigation system always coincide whereas in the two-beam geometry, they are separated by PRC length. This length can be greater than the diffraction length. That is why we recalculated the output field to the input plane. In a real experiment, it is equivalent to addition of a lens to form the input image.

In parallel with (4), in four-beam geometry, we characterized the quality of noise mitigation by the more convenient value - the overlapping integral  $H^{10}$ .

$$H = \frac{\left| \sum E_{in} E_{out} \right|^2}{\sum |E_{in}|^2 \sum |E_{out}|^2} \quad (2.6)$$

### 2.3. Theory

To illustrate a possibility of dynamic noise filtration in such a scheme, we can use the simplest case without amplitude distortions. Let as signal beam with the amplitude  $E_1$  and the phase distortions (2.3) as plane pumping wave with the amplitude  $E_2$  are directed onto PRC's input plane

$$E = E_1 e^{ik_x} + E_2 e^{ik_x + i\delta\phi}. \quad (2.7)$$

Here  $E$  is the resulting field in the input plane,  $k_x$  is the transverse projection of the wave vector. Under assumption of fixed intensity of the beams and with ignoring of the diffraction, the distribution of intensity in PRC can be found as

$$\begin{aligned} I = EE^* = E_1^2 + E_2^2 + 2E_1 E_2 J_0(A_n) \sum_{m=-\infty}^{+\infty} J_m(A_s) \exp[i(2k_x + mk_s)x] + \\ + 2E_1 E_2 \sum_{m=-\infty}^{+\infty} \sum_{l \neq 0} J_m(A_s) J_l(A_s) \exp\{i[(2k_x + mk_s + lk_n)x - n\Omega t]\}. \end{aligned} \quad (2.8)$$

Here  $J_m(x)$  is the  $m$ -order Bessel function. If PRC does not respond to the high-frequency components of the fringe pattern (2.8) due to its inertia, the gratings at the spatial frequencies  $(2k_x + mk_s)$  corresponding to the useful information will be only written. Thus, in the case of so-called diffusion transportation of charge ("nonlocal response",  $E_0=0$ ),

$$\delta n \propto E_1 E_2 J_0(A_n) \sum_{m=-\infty}^{+\infty} i(2k_x + mk_s) J_m(A_s) \exp[i(2k_x + mk_s)x] \quad (2.9)$$

It means that only spectral components at the useful spatial frequencies can be amplified. When  $\Omega \gg 1/\tau$  ( $\tau$  is the PRC characteristic response time) and spatial frequencies of the noise and the useful signal are not multiple, one can obtain steady-state solution as

$$\beta^{out} = \frac{\beta^{in}}{\gamma}. \quad (2.10)$$

It is easy to see that  $\beta^{out}$  depends only on the gain constant  $\gamma$ . It means that the larger will be the difference in  $\gamma$  for the useful and noise parts of  $E$ , the better will be the quality of filtration of dynamic distortions. So, in two-beam geometry, the maximal magnitude of  $\beta^{out}$  is always limited by the maximal value of  $\gamma$  and initial noise level.

The estimation (2.10) is not valid for the four-beam geometry. Under the same assumptions and for the case with nonlocal character of PRC response,

$$E^{out} \propto (2k_x - iA_s k_s \cos(k_s x)) \exp\{-i(k_s x - A_s \sin(k_s x))\}. \quad (2.11)$$

Thus, under  $2k_s \gg A_s k_s$ , that is typical for a real experiment, the output beam contains only the useful information. In the case with local character of PRC response, the useful signal can be completely filtered as well. However, even in these simplest examples, the solutions change radically under violation of conditions mentioned above. The problem becomes much more complicated if we try to take into account diffraction, self-action,

frequency detuning, real PRC thickness, etc. In this case, it is impossible to find both steady-state and transient solutions of the problem in analytical form. So, computer simulation is the only way to solve this problem.

#### 2.4. Numerical results

All parameters of our simulation corresponded to well-known PRC InP:Fe<sup>1,2</sup>. Its electrooptical constant is 1.45 pm/V,  $n=3.3$ , and the free path length of carriers is determined by  $\mu/\alpha_r=1.5 \cdot 10^{-4} \text{ cm}^2/\text{V}$ . We represented 1 mm length PRC as 20-80 phase screens and described the spatial distributions of  $n$  and  $I$  by arrays of 8192 points in the aperture of 3 mm. We assumed that the signal beam with 1 mm diameter formed the transmission gratings with 5  $\mu\text{m}$  period.

##### 2.4.1. Two-beam interaction

For this geometry, our computer simulation confirmed the possibility of efficient mitigation of phase dynamic distortions. Under conditions listed in section 1, after switching the mitigation system on,  $\beta^{out}$  decreases from the value  $\beta^n$  up to the steady-state level (2.9) with the characteristic time  $\tau$  (Fig.2.1b). However, with violation of any conditions listed above, the dependence  $\beta^{out}(t/\tau)$  changes drastically. Fig.2.1a illustrates characteristic oscillations in  $\beta^{out}(t/\tau)$  for the case when  $k_s=k_n$  and  $\Omega\tau \gg 1$ . These oscillations can be interpreted with ease by simple qualitative reasoning. In this case, effective energy exchange between all spectral components of the signal takes place because the refractive index gratings contain both useful and noise information. That is why the effective filtration of dynamic noise does not occur. The range of  $k_n$ , where we can observe this regime, is determined by the spectral selectivity of written 3D grating, that is, by the aperture of interacting beams.

Nonlinear response of PRC is usually not of "pure" nonlocal character. For example, such a character results from the use of the static electric field  $E_0$  to increase the gain constant<sup>11</sup>. Our simulation has shown that  $\beta^{out}(t/\tau)$  strongly depends on the frequency detuning  $\Delta\omega$  between the interacting beams. Fig.2.2 represents the steady-state dependencies  $\beta_{st}^{out}(\Omega\tau)$  for different relationships between the local and nonlocal parts in PRC nonlinear response. This figure illustrates effects arising under violation of the  $\Omega\tau \ll 1$  condition. Because our system is a time averaging filter, only the distortions with characteristic times that are less than  $\tau$  can be mitigated. In opposite case, the gratings at frequency  $\Omega$  will be efficiently written in PRC that leads to efficient amplification of the noise components and decreases the mitigation quality. Typical dependencies  $\beta^{out}(t/\tau)$  for some values of the parameter  $\Delta\omega\tau$  are shown in fig.2.3. Fig.2.3a corresponds to the case with domination of nonlocal response. Fig.2.3b relates to the opposite case when the quality of noise mitigation is optimal when  $\Delta\omega=0$ . The reason of this result is following. When  $\Delta\omega=0$ , the optimal phase shift between the interference fringe pattern and the refractive index grating ( $\pi/2$ ) is achieved for some shifted spectral components of the noise. Therefore, the gain constant for these components is larger than the gain constant for the useful signal. Obviously this fact will decrease the mitigation quality. However, one can optimize the phase shift by means of some well-known ways. It is possible to optimize the frequency shift of pumping<sup>12</sup> in relation of the useful signal (see fig.2.3b) or the frequency of external alternate electric field<sup>13</sup>. The last technique enables one to realize the highest value of the gain constant.

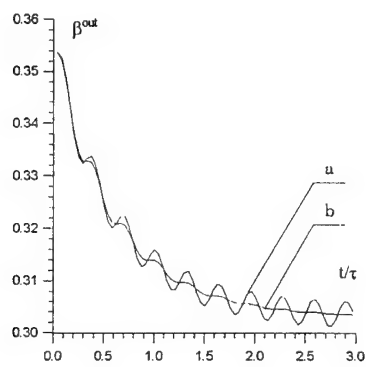


Fig.2.1.  $\beta^{out}$  versus  $t/\tau$  in two-beam geometry:  $k_s = 130 \text{ cm}^{-1}$ ,  $k_n = 130 \text{ cm}^{-1}$  (a) and  $100 \text{ cm}^{-1}$  (b);  $A_s=0.2$ ;  $A_n=0.5$ ;  $E_0=0$ ;  $\Omega\tau \gg 1$ .

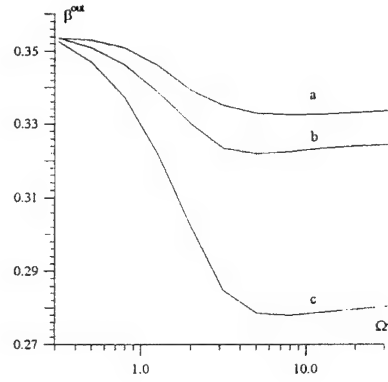


Fig.2.2.  $\beta_{st}^{out}$  versus  $\Omega\tau$  in two-beam geometry:  $k_s = 100 \text{ cm}^{-1}$ ,  $k_n = 130 \text{ cm}^{-1}$ ;  $A_s=0.2$ ;  $A_n=0.5$ ;  $E_0 = 5.5$  (a,b) and 15 (c) kV/cm;  $\Delta\omega\tau=0$  (a) and 1 (b,c).

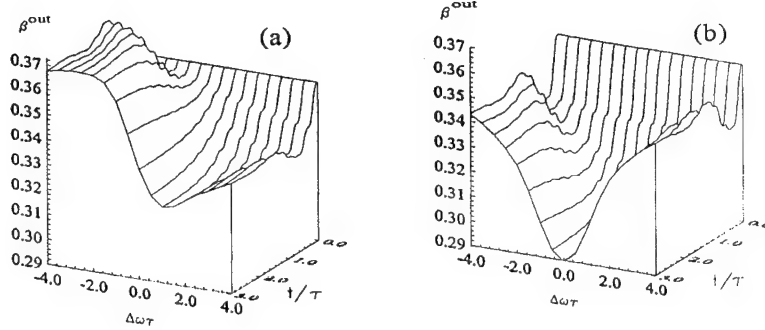


Fig.2.3.  $\beta_{\text{out}}^{\text{out}}$  versus  $t/\tau$  and  $\Delta\omega\tau$  in two-beam geometry:  $k_s=100 \text{ cm}^{-1}$ ,  $k_n=130 \text{ cm}^{-1}$ ;  $A_s=0.2$ ;  $A_n=0.5$ ;  $E_0=0$  (b) and  $5.5 \text{ kV/cm}$  (a);  $\Omega\tau \gg 1$ .

#### 2.4.2. Four-beam interaction

For this geometry we have considered the problem of mitigation of both phase and amplitude dynamic distortions and studied the possibility of reconstruction of amplitude image.

According to our computer simulation of four-beam geometry, after switching the system on,  $\beta_{\text{out}}^{\text{out}}$  begins to decrease from its initial value  $\beta_{\text{out}}^{\text{out}}$  to the steady-state level  $\beta_{\text{ss}}^{\text{out}}$  at  $t > \tau$  (fig.2.4a). The overlapping integral dependence  $H(t/\tau)$  exhibits improvement of the output beam quality, too (fig.2.4b). However, in contrast to the two-beam geometry (see fig.2.1, curve b), the characteristic time of this transient process is determined by the new time constant  $1/\Omega$  that is much smaller than  $\tau$ . The reason of such a difference is very simple. The dynamic noise penetrates to the output of four-beam mitigation system only if this noise has been written in the refractive index grating. Therefore, the grating amplitude  $\delta n$  determines only the energy efficiency of the system, whereas the accuracy of this grating determines the mitigation quality. In our case, the correct grating forms during the time interval  $1/\Omega$  and after that the output signal power  $I_{\text{out}}^{\text{out}}$  continue to grow with the characteristic time  $\tau$  (fig.2.4c). We have found that the  $\beta_{\text{ss}}^{\text{out}}$  value is rather sensitive to spatial frequency of the input signal (fig.2.5). It means that the limiting level of distortion mitigation is determined by the small-scale self-focusing process. The case  $k_s=k_n$  is followed by characteristic oscillations in  $\beta_{\text{out}}^{\text{out}}(t)$  (fig.2.6). However,  $\beta_{\text{out}}^{\text{out}}(t)$  does not depend on the phase shift of grating and frequency detuning between the interacting beams (fig.2.7).

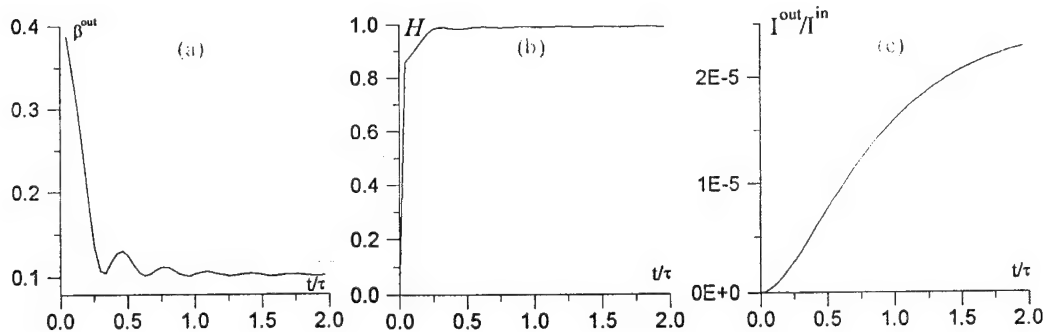


Fig.2.4.  $\beta_{\text{out}}^{\text{out}}$  (a),  $H$  (b), and  $I_{\text{out}}^{\text{out}}/I_{\text{in}}$  (c) versus  $t/\tau$  for the case with mitigation of phase distortions in four-beam geometry:  $k_s=100 \text{ cm}^{-1}$ ,  $k_n=130 \text{ cm}^{-1}$ ;  $A_s=0.2$ ,  $A_n=0.5$ ;  $E_0=0$ ;  $\Omega\tau \gg 1$ .

Our simulation has confirmed the possibility of effective mitigation of amplitude dynamic distortions in four-beam geometry as well (fig.2.8 and fig.2.9). In these cases, we simulated the total input signal as sum of the amplitude dynamic noise and the phase

$$E^{\text{in}} = E_s \exp\left(-\left(\frac{x}{a}\right)^2\right) \left(1 + \sin(k_s x)\right) + E_n \sin(k_n x - \Omega t) \quad (2.12)$$

or amplitude

$$E^{\text{in}} = e^{-\left(\frac{x}{a}\right)^2} \left(1 + 0.5 \sin(k_s x)\right) + 5 \sin(k_n x - \Omega t) \quad (2.13)$$

image, respectively. Here,  $a$  is the beam radius,  $E_n$  represents the dynamic noise amplitude. It is very important that for the realizations shown in figures 8 and 9,  $E_n$  is five times larger than the amplitude of the useful signal.

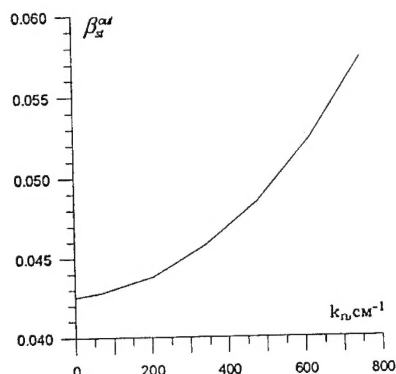


Fig. 2.5.  $\beta_s^{out}$  versus  $k_n$  for the case of mitigation of phase distortions in four-beam geometry:  $k_s = 130 \text{ cm}^{-1}$ ;  $A_s = 0.2$ ;  $A_n = 0.5$ ;  $E_0 = 15 \text{ kV/cm}$ ;  $\Omega\tau \gg 1$ .

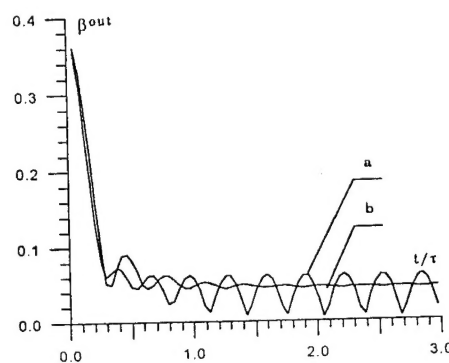


Fig. 2.6.  $\beta_s^{out}$  versus  $t/\tau$  for the case of mitigation of phase distortions in four-beam geometry:  $k_s = 130 \text{ cm}^{-1}$ ;  $k_n = 130$  (a) and  $150$  (b)  $\text{cm}^{-1}$ ;  $A_s = 0.2$ ,  $A_n = 0.5$ ;  $E_0 = 0$ ;  $\Omega\tau \gg 1$ .

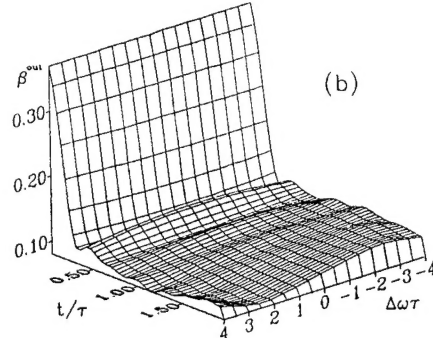
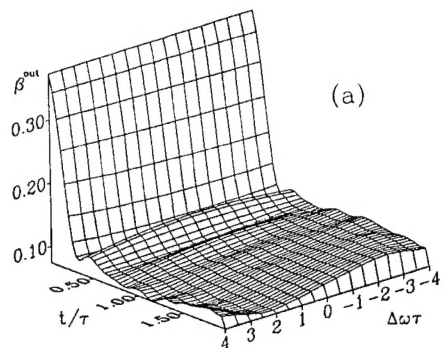


Fig. 2.7.  $\beta_s^{out}$  versus  $t/\tau$  and  $\Delta\omega\tau$  for the case of mitigation of phase distortions in four-beam geometry:  $k_s = 100 \text{ cm}^{-1}$ ,  $k_n = 130 \text{ cm}^{-1}$ ;  $A_s = 0.2$ ;  $A_n = 0.5$ ;  $E_0 = 0$  (b) and  $5.5$  (a)  $\text{kV/cm}$ ;  $\Omega\tau \gg 1$ .

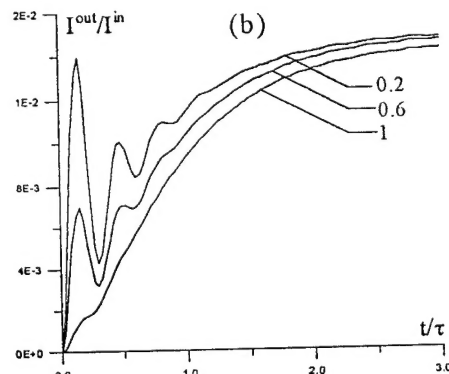
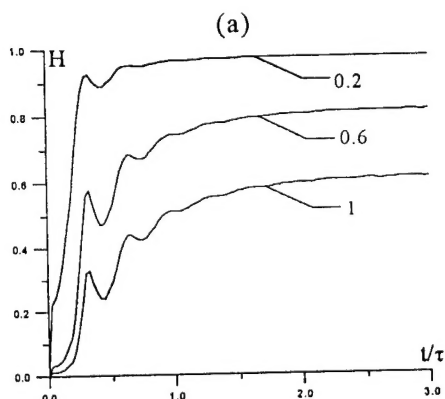


Fig. 2.9.  $H$  (a) and  $I_s^{out}/I_s^{in}$  (b) versus  $t/\tau$  for the case with mitigation of amplitude distortions in four-beam geometry:  $t/\tau = 0$  corresponds to the "switching on" moment;  $k_s = 110 \text{ cm}^{-1}$ ,  $k_n = 140 \text{ cm}^{-1}$ ;  $E_s = 0.1$ ;  $E_n = 0.2, 0.6$ , and  $1$ ;  $E_0 = 0$ ;  $\Omega\tau \gg 1$ .

So, our simulation has proved that under the same conditions, in comparison with the systems based on the two-beam geometry, the mitigation systems based on the four-beam geometry are much more effective.

### 2.5. Conclusions

1. A new promising numerical scheme for simulation of self-consistent problems, arising from the problem of nonlinear interaction of spatial-modulated beams in PRC, was proposed.
2. The scheme was tested and it was shown that two- and four-beam geometry of nonlinear interaction in PRC can be used to mitigate phase and amplitude dynamic distortions.
3. The scheme enables one to simulate various problems of dynamics of two- and four-beam interaction in PRC with taking into account diffraction, self-action, exhaustion of pumping, etc.
4. The same approach can be extended to much more complicated problems of nonlinear interaction such as dynamics of self-pumping PC-systems<sup>14</sup>.

### 2.6. Publications

Following papers with our acknowledgments to the US Army Research Laboratory contract No 68171-

94-C-9147 issued through US Army European Research Office, London, UK have been prepared and published:

1. V.N.Kutuzov, V.V.Shuvalov, V.A.Vysloukh. *Dynamic phase distortion suppression by phase-conjugation systems with inertial photorefractive nonlinearity*, ICONO'95 Proceedings **1**, 437 (1995).
2. V.N.Kutuzov, V.V.Shuvalov, V.A.Vysloukh. *Dynamic distortion filtration using systems based on inertial photorefractive nonlinearity*, Kvantovaya Elektronika **18**, #1 (1996, to be published) (in Russian).
3. V.N.Kutuzov, V.V.Shuvalov, V.A.Vysloukh. *Dynamic phase distortion suppression by phase-conjugation systems with inertial photorefractive nonlinearity*, SPIE Proceedings (1996, to be published).

### 2.7. Literature Cited

1. "Photorefractive materials and their applications", *Topics in applied physics*, **62**, Springer, 1989.
2. "Photorefractive materials and their applications", *Topics in applied physics*, **61**, Springer, 1988.
3. N.V. Kukhtarev et al. *Ferroelectrics* **22**, 949 (1979).
4. R.W. Hellwarth. *J. Opt. Soc. Am.* **67**, 1 (1977).
5. V.V. Ivakhnik et al. Kvantovaya Elektronika **7**, 989 (1980) (in Russian).
6. A. Yariv, T.L. Koch. *Opt. Lett.* **7**, 113 (1982).
7. M.S. Barashkov et al. Kvantovaya Elektronika **10**, 1502 (1983) (in Russian).
8. E. Oldekop, A. Siahmakoun. *Proc. SPIE* **1396**, 174 (1991).
9. M.P. Petrov, S.I. Stepanov, A.V. Khomenko, "Photorefractive crystals in coherent optics", Nauka, St.-Petersburg, 1992 (in Russian).
10. B.Ya. Zel'dovich, V.V. Shkunov. *JETP (Moscow)* **2**, 428 (1978) (in Russian).
11. B. Mainguet. *Opt. Lett.* **13**, p.657 (1988).
12. K.R. McDonald, J. Feinberg. *Phys. Rev. Lett.* **55**, 821 (1985).
13. D.T. Liu et al. *Opt. Commun.* **72**, 384 (1989).
14. M. Cronin-Colomb et al. *IEEE J. Quant. Electr.* **QE-20**, 12 (1984).

## List of publications

1. V. P. Kandidov, "Monte Carlo method in statistical nonlinear optics", *Uspekhi Fizicheskikh Nauk* (in Russian), (to be published 1996).
2. S. S. Chesnokov, I. V. Davletshina, "Dynamical structure of light beam phase distortions in nonlinear turbulent media", Proc. SPIE (to be published 1996).
3. V. I. Shmalhausen, A. V. Koryabin, "Influence of phase distortion on imaging of extended objects", Proc. SPIE (to be published 1995).
4. V. N. Kutuzov, V. V. Shuvalov, V. A. Vysloukh, "Dynamic phase distortion suppression by phase-conjugation systems with inertial photorefractive nonlinearity", Technical Digest of 15th International Conference on Coherent and Nonlinear Optics, St. Petersburg Russia, Vol. 1, 437 (1995).
5. V. N. Kutuzov, V. V. Shuvalov, V. A. Vysloukh, "Dynamic distortion filtration using systems based on inertial photorefractive nonlinearity", *Kvantovaya Elektronika* (in Russian), Vol. 18, N1, 1996 (to be published).
6. V. N. Kutuzov, V. V. Shuvalov, V. A. Vysloukh, "Dynamic phase distortion suppression by phase-conjugation systems with inertial photorefractive nonlinearity", Proc. SPIE (to be published 1996).

## **List of participating scientific personnel**

Principal Investigator, Associate Professor S.S.Chesnokov

Technical Manager, Associate Professor B.V. Zhdanov

Technical Secretary N.G. Podkopaeva

### **Part I. Numerical simulation of laser beam propagation through atmospheric turbulence**

Professor V.P. Kandidov

Associate Professor S.S.Chesnokov

Associate Professor S.A. Shlyonov

Assistant Researcher N.G. Iroshnikov

Assistant Researcher T.A. Matveeva

Assistant Researcher I.V. Davletshina

Assistant Researcher O.G. Kosareva

PhD Student I.V. Krupina

Student M. Tamarov

Student A. Skulacheva

Student S. Skipetrov

### **Part II. Optical modelling of laser beam propagation through the turbulent atmosphere**

Professor V.I. Shmalhausen

Senior Researcher A.V. Koriabin

Assistant Researcher A.V. Larichev

PhD Student X.V. Prokofieva

PhD Student A.N. Simonov

Student D. Mamontov

Student N. Yaitskova

### **Part III. Photorefractive crystal (PRC) based technology for distortion mitigation in laser beams**

Senior Researcher V.V. Shuvalov

Associate Professor V.A. Vysloukh

Senior Researcher V.M. Petnikova

Student V. Kutuzov

Student D. Mazurin